REPORT DOCUMENTATION PAGE

Form Approved
OMB No. 0704-0188

The public reporting burden for this collection of information is estimated to average 1 hour per response, including the time for reviewing instructions, searching existing data sources, gathering and maintaining the data needed, and completing and reviewing the collection of information. Send comments regarding this burden estimate or any other aspect of this collection of information, including suggestions for reducing the burden, to the Department of Defense, Executive Service Directorate (0704-0188). Respondents should be aware that notwithstanding any other provision of law, no person shall be subject to any penalty for failing to comply with a collection of information if it does not display a currently valid OMB control number.
PLEASE DO NOT RETURN YOUR FORM TO THE ABOVE ORGANIZATION.

1. REPORT DATE (DD-MM-YYYY)	2. REPORT TYPE		3. DATES COVERED (From - To)
01-03-2009	Final		22-10-2005 to 30-09-2008

4. TITLE AND SUBTITLE	5a. CONTRACT NUMBER
Engineered Bio-Molecular Nano-Devices/Systems	FA9550-06-C-0006
	5b. GRANT NUMBER N/A
	5c. PROGRAM ELEMENT NUMBER N/A

6. AUTHOR(S)	5d. PROJECT NUMBER
Hibbs, Andrew, D., and Barrall, Geoffrey, A.	N/A
	5e. TASK NUMBER N/A
	5f. WORK UNIT NUMBER N/A

7. PERFORMING ORGANIZATION NAME(S) AND ADDRESS(ES)	8. PERFORMING ORGANIZATION REPORT NUMBER
Electronic Bio Sciences, LLC 5754 Pacific Center Blvd. Suite 204 San Diego, CA 92121	N/A

9. SPONSORING/MONITORING AGENCY NAME(S) AND ADDRESS(ES)	10. SPONSOR/MONITOR'S ACRONYM(S)
USAF, AFRL AF Office of Scientific Research 875 N. Randolph Street, Rm. 3112 Arlington, VA 22203	AFOSR
	11. SPONSOR/MONITOR'S REPORT NUMBER(S) N/A

12. DISTRIBUTION/AVAILABILITY STATEMENT
Distribution Statement A. Approved for public release, distribution unlimited.

13. SUPPLEMENTARY NOTES
N/A

14. ABSTRACT
The goal of the MOLDICE program was to exploit ion channels for practical ion channel based sensing. Stochastic sensing provides a detection method that can deliver extremely low false alarm rates while still maintaining a high probability of detection. In order to develop a practical system that could be deployed in the field, the EBS led team addressed several key system parameters. First, to eliminate the previous need for vibration isolation for ion channel measurements, a stable bilayer platform was implemented. This platform uses a glass nanopore membrane device which contains a nanometer scale orifice that provides a solid support for a suspended lipid bilayer and subsequent protein insertion. To provide highly specific analyte detection, the alpha hemolysin protein pore sensor was genetically engineered. The (M113K)7 pore was incorporated into the final system and is able to detect ppb concentrations of DTPMPA in the presence of ppm concentrations of a TDP interferent. The EBS led team developed a prototype system that was portable for offsite demonstration of an ion channel based detection system. The program resulted in the successful demonstration of this prototype system at an offsite location in Arlington, VA on May 2, 2008.

15. SUBJECT TERMS
Glass nanopore membrane, Ion channel sensing, Modified protein pores

16. SECURITY CLASSIFICATION OF:			17. LIMITATION OF ABSTRACT	18. NUMBER OF PAGES	19a. NAME OF RESPONSIBLE PERSON
a. REPORT	b. ABSTRACT	c. THIS PAGE			Tracey Wrightson
U	U	U	UU	100	**19b. TELEPHONE NUMBER (Include area code)** 858-412-1800

Standard Form 298 (Rev. 8/98)
Prescribed by ANSI Std. Z39.18
Adobe Professional 7.0

MOLDICE Final Report

Electronic Bio Sciences, LLC

Principal Investigator:
Dr. Andrew D. Hibbs, CEO
Electronic Bio Sciences
5754 Pacific Center Blvd., Suite 204
San Diego, CA 92121
Tel: (858) 373-0232
Fax: (858) 412-1728
ahibbs@electronicbio.com

Administrative Point of Contact:
Tracey Wrightson, Director of Operations
Electronic Bio Sciences
5754 Pacific Center Blvd., Suite 204
San Diego, CA 92121
Tel: (858) 412-1800
Fax: (858) 412-1728
twrightson@electronicbio.com

20090518119

Table of Contents

1. Executive Summary

The goal of the MOLDICE program was to exploit ion channels for practical ion channel based sensing. Stochastic sensing provides a detection method that can deliver extremely low false alarm rates while still maintaining a high probability of detection.

In order to develop a practical system that could be deployed in the field, several key system parameters needed to be addressed. Previous ion channel experiments have all been completed in laboratory settings requiring a vibration isolation table due to the fragility of the bilayer. Thus, a stable bilayer platform needed to be developed. The EBS led team has examined several platforms including tethered lipid bilayers on gold surfaces as well as suspended bilayers over silicon or glass nanoscale orifices. Ultimately, the system development focused on the glass nanopore membrane device consisting of a glass capillary with a nanometer scale orifice at one end to provide a solid support for a suspended lipid bilayer and subsequent protein insertion. This device has provided channel recordings of over 16 days without vibration isolation. In addition, with bilayer formation methods developed under this program, bilayers and protein insertions can be readily repeated if the bilayer does fail.

To provide highly specific analyte detection, the alpha hemolysin protein pore sensor must be genetically engineered. Groups at the University of Oxford and University of Texas Arlington developed pores that are able to specifically bind mustard agents and the organophosphate DTPMPA respectively. Ultimately the $(M113K)_7$ pore was chosen to be incorporated into the final system to show detection of ppb concentrations of DTPMPA in the presence of ppm concentrations of a TDP interferent. Once the protein was developed, methods for incorporation into the glass nanopore membrane were developed to allow the channels to insert into the greatly reduced membrane size compared to usual ion channel experiments. The protein was also produced in large quantities by an outside laboratory.

The EBS led team went through multiple system revisions to develop a prototype system that was portable for offsite demonstration of an ion channel based detection system. This system used a glass nanopore platform, automated fluid flow and pressure control with a $(M113K)_7$ pore incorporated in the bilayer to demonstrate the detection of 100 nM DTPMPA in the presence of 250 µM TDP. The successful demonstration was performed at an offsite location in Arlington, VA on May 2, 2008.

2. Stochastic Sensing

The stochastic sensor works by measuring the current through one or more ion channels (e.g. the protein channel α-hemolysin (αHL) embedded in a lipid bilayer as shown in Figure 1. The ion channel pictured is the αHL channel produced by the bacterium *staphylococcus aureus*. Electrodes located on opposite sides of the lipid bilayer apply a voltage bias producing current flow through the ion channel. Electrolytes in aqueous reservoirs act as the charge carriers. The applied voltage bias is generally on the order of 10's of millivolts and the current through the ion channel is measured in the pico-Ampere regime. The measured signal, right side of Figure 1, is a simple current as a function of time trace that shows discrete changes in current when a single molecule binds to the interior of the ion channel. This type of measurement is commonly referred to as a single channel measurement [1]. When the ion channel is open the current is at a maximum. When an analyte reversibly binds to the interior of the ion channel, the channel is blocked and the current is temporarily decreased. The average duration and amplitude of the current block are dependent upon the binding affinity between the ion channel and the bound molecule. Naturally occurring and genetically engineered ion channel proteins have been used

to sense metal cations [2, 3], anions [4], organic molecules [5, 6], linear polymers [7], proteins [8, 9] and DNA [10-13].
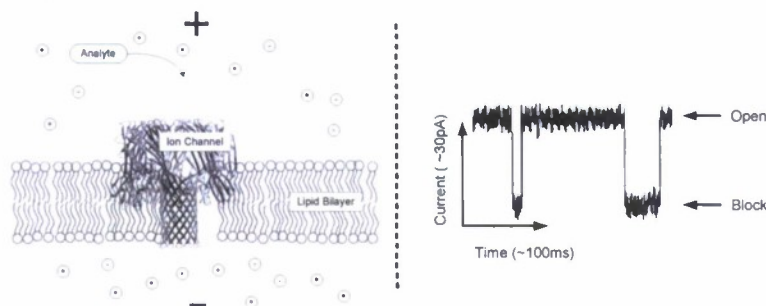

Figure 1. (Left) The interaction between an ion channel in a lipid bilayer with a target analyte molecule. (Right) An example of current blocking caused by the reversible binding of an analyte molecule to the interior of the ion channel. Such current measurements are commonly referred to as single channel measurements.

Discrimination between analytes is based upon three separate factors: affinity to functional groups in the ion channel, amount of current blocked during the single molecule binding event, and the duration of the blocking event. Determination of the analyte concentration is determined by the frequency of analyte binding events. Each of these aspects are described in detail below.

A depiction of the αHL protein, the current workhorse ion channel for stochastic sensing, as assembled in a lipid bilayer is shown in Figure 2. By modifying the amino acids in the 1.5 nm constriction region, it is possible to confer a high level of selectivity analyte binding in the interior of the channel. For example, the 111th and 113th residues (glutamate and methionine for wild type αHL) are amenable to substitution with other amino acids that display very different chemical properties.
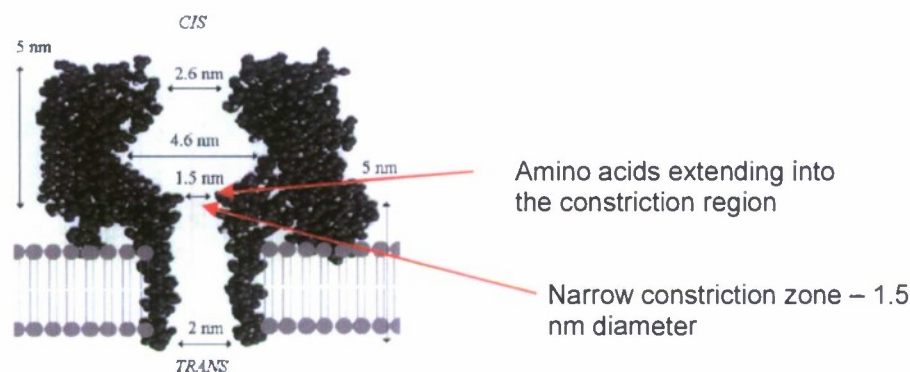
Figure 2. View of the interior of the αHL heptamer inserted into a lipid bilayer. The narrow 1.5 nm constriction occurs at the 111th and 113th residues (glutamate and methionine for wild type αHL) in each monomer.

The amplitude of the current block is characteristic of the analyte present in the channel. Many analytes that are too large to enter the ion channel or have little to no affinity with functional groups introduced in the interior of the channel will not cause a measurable current block. Only analyte molecules that are able to enter the channel, block a significant fraction of the internal cross section of the channel and stay in that position for 100's of microseconds to milliseconds will be detected. Analytes that do cause a measurable change in current will cause different reductions in current depending upon the nature of the analyte (e.g. size, chemistry, charge).

An example of a single channel recording for such a system is shown on the left of Figure 3. The distribution of blocking amplitudes (right side of Figure 3) shows a clear separation between two organophosphates, TDP (Thymidine 5'-diphosphate sodium salt) and DTPMPA (Diethylene Triamine Penta (methylene phosphoric acid)). In this case the methionine residue at position 113 was replaced with lysine to promote binding of DTPMPA.
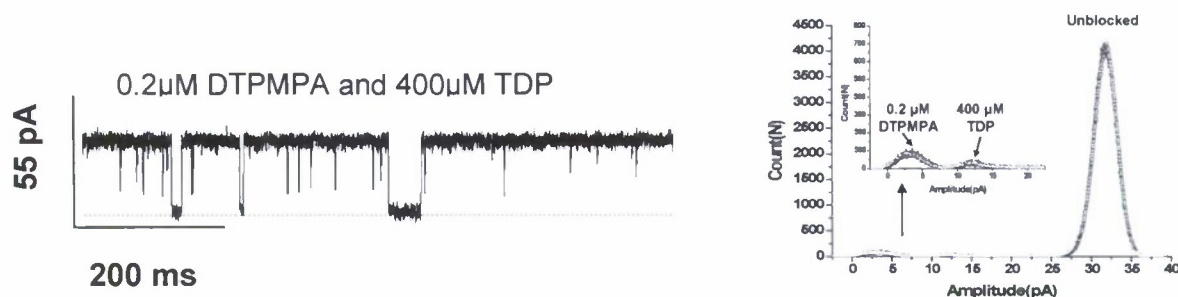
Figure 3.   (Left) Portion of a single channel recording for a mixture of the organophosphates DTPMPA and TDP. The αHL channel has been modified to have affinity to organic phosphate anions by replacing methionine in the 113th residue with lysine. (Right) The distribution of current levels can be used to discriminate between analytes. In this case the large peak to the right is the open channel current (~32 pico Amperes) and the two smaller peaks arise from two analytes in the test volume.

The duration of the binding times can also be used to discriminate between analytes. The binding is generally characterized by a first order rate constant, so the distribution of blocking times takes the form of an exponential as shown in Figure 4. Signals can also be separated simultaneously based on amplitude and duration to create a two-dimensional decision space. If multiple analytes have similar current blocking levels, the distribution of blocking event durations can be deconvoluted to reveal the separate contributions. An example is shown on the right of Figure 4. DNA segments of increasing length (e.g. 3 base pairs (bp) versus 4 bp) show a trend of increasing current block and increasing block duration. The large spread in the % unblocked current (I/I_0) for 3 bp is an artifact due to the low bandwidth of the measurement device.
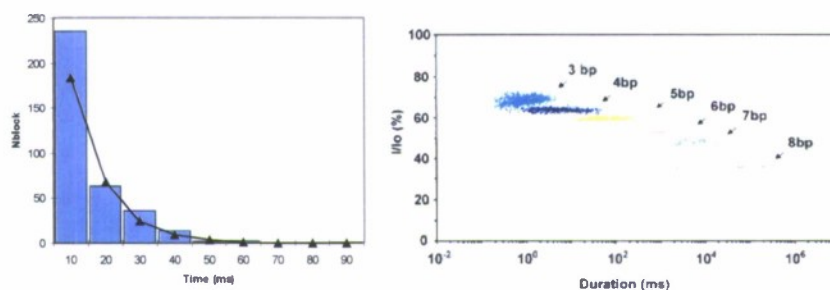
Figure 4. (Left) The duration of the blocking events depends upon the binding affinity of the analyte to the interior of the ion channel. The distribution of blocking event durations is generally an exponential. (Right) A plot of % unblocked current vs blocking duration shows a clear separation between signals for similar molecules (DNA segments differing by a single base pair [11]).

Stochastic sensing has a very powerful, and in fact unique, combination of properties for detection of small molecules in a wide background of interferent molecules and in an aqueous environment:

1. Two independent measurement outputs (blocking amplitude and duration) provide a high level of target discrimination from background clutter

2. The ion channel can be modified to optimize detection of a desired class of molecules
3. Single molecule operation offers the ultimate sensitivity
4. Individual molecular interactions provide a direct measure of concentration
    100 mV voltage bias and 100 pA currents give sub nanowatt power consumption
5. Reversible binding means that the detection system is not used up
6. Aqueous samples may be used directly without having to force the analyte into the gas phase
7. The nanoscale ion channel offers a very compact final system size and array possibilities

3. Stochastic Sensing Platforms

While stochastic sensing has great potential, a limiting factor has been the availability of a robust platform for the sensing of ion channel conductance (i.e. stochastic sensing). Under the MOLDICE program we have investigated three separate platforms. These are described in detail below.

3.1. The Supported Bilayer on Gold

3.1.1. Summary

Tethered bilayer membranes (tBLMs) on gold electrodes have the potential to be extremely robust platforms for the measurement of ion channel conductance. tBLMs provide excellent stability by covalently linking the bilayer membrane to a solid support. The inner leaflet of the membrane is bound to the solid support via a short spacer group. Thiol anchors are used to graft the membrane onto the gold electrode, which allows for the measurement of the ion channel conductance.

A schematic of the tBLM on a gold electrode is shown in Figure 5A. Lipid constructs are connected to the gold electrode via a spacer group that allows for a reservoir of electrolyte solutions. The tBLM is completed by fusing phospholipids to the upper surface of the tBLM. Ion channels are incorporated by standard methods. The conductance of the ion channel and the tBLM is measured using an AC bias. The resulting record, Figure 5B, is the ratio of the voltage and current from the counter electrode in solution to the working gold electrode relative to a reference electrode. Typically in electrical impedance spectroscopy, the signal is recorded over a range of frequencies to separate the frequency independent (resistance, R) and frequency dependent (capacitance, C) components of the impedance, Z. This is described in more detail below. A circuit model, Figure 5C, is then used to analyze the record and determine the capacitance and resistance of the tBLM and associated ion channels.
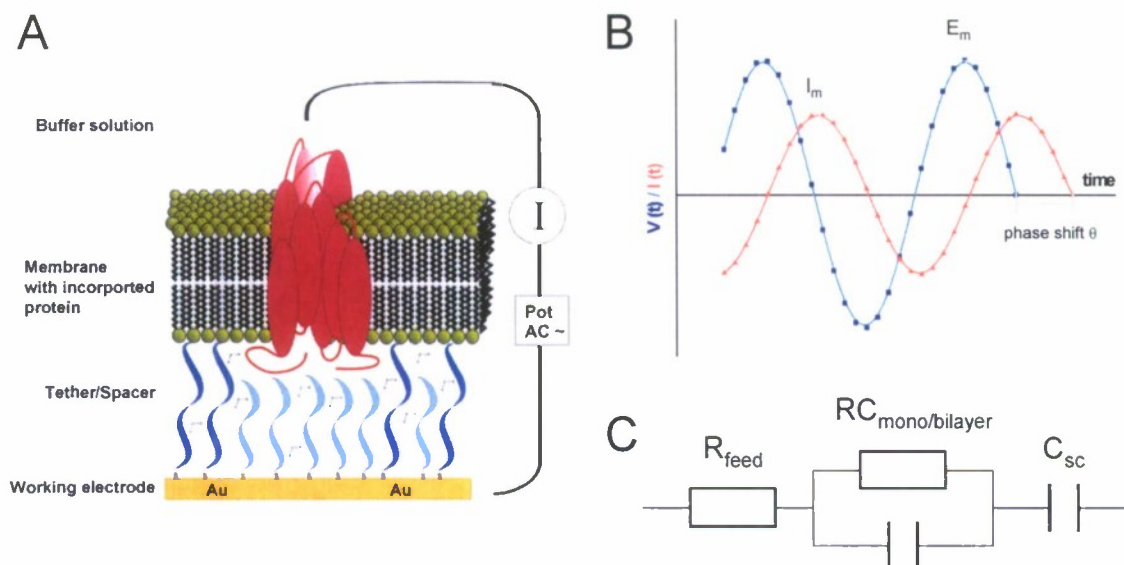
Figure 5.   (A) The tBLM architecture and associated measurement apparatus.   (B) Electrorecording of the (amplitude and phase of the) current response upon the application of a small-amplitude ac voltage. (C) Typical circuit model used to fit to the

By measuring the conductance across the tBLM and gold electrode over a range of frequencies it is possible to quickly separate the capacitance and resistance of the tBLM. This is particularly important since the activity of the ion channels will be measured by changes in the resistance of the system. If the resistance of the bilayer is too low or the capacitance is too high, it will not be possible to measure the changes in the resistance due to the ion channel. A representative Bode plot for the conductance across a large area tBLM is shown in Figure 6. The change in resistance terms are measured proportional to the plateaus in the impedance, Z. The capacitance is measured by shifts in the impedance curve. In this case, the resistance of the tBLM is ~5 MΩ and the capacitance across the tBLM is ~0.2 µF.

R_1 /Ω	$R_2 /M\Omega$	$C_1 /\mu F$	$C_2 /\mu F$
100	5	0.2	2
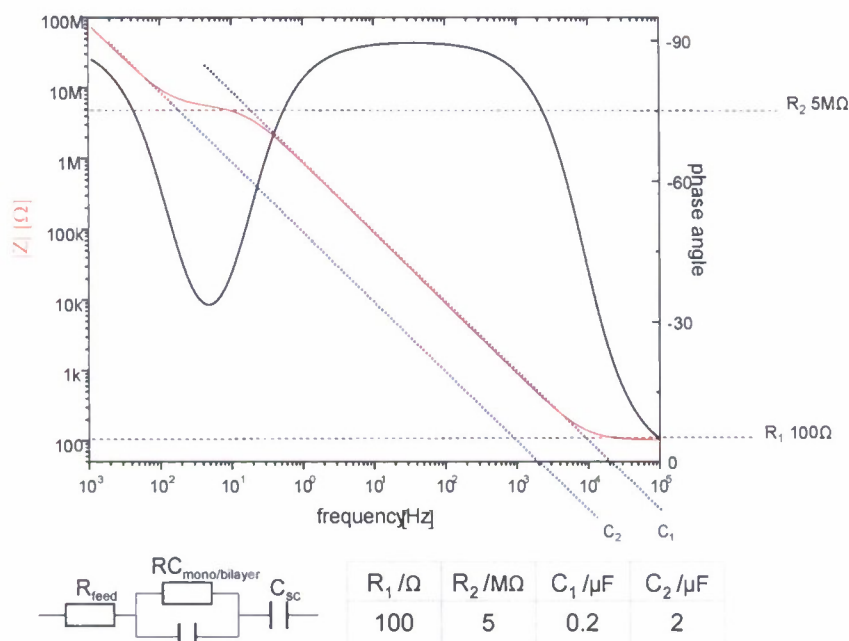
Figure 6.   Bode plot derived from the conductance measurements across a gold electrode.

Under the current program, the Max Planck Institute (MPI) has developed improved tether molecules for the formation of tBLMs and has demonstrated the ability to maintain active sensor elements for up to 7 months.   The Electronic Bio Sciences (EBS) and University of Texas at Austin (UTAustin) groups developed microelectrode versions of the devices with integrated electronics that significantly improve the fabrication and have the potential to make single ion channel conductance measurements.   Defects in the bilayers at the edge of the tBLM have hindered our ability to make stochastic sensing measurements with this platform, but a new gold electrode fabrication process recently developed by MPI may solve this remaining problem.

3.1.2. Formation of Electrode by the Template Stripped Gold Method

In order to produce a high resistance tBLM it is necessary to have a very smooth gold surface. tBLMs on Polycrystalline gold surfaces produced by traditional vapor deposition techniques yield resistances < 0.05 $M\Omega \cdot cm^2$ [14].   In order to measure the changes in conductance of a single ion channel, it is necessary to have significantly greater resistance in the tBLM.

MPI has developed a method to produce gold electrode surfaces with an rms roughness of ~0.25 nm.   The template stripped gold (TSG) electrode [15] relies upon the inherent smoothness of mica sheets to produce atomically smooth gold surfaces. As shown in Figure 7, gold films (50 nm thick) are deposited by electro-thermal evaporation (rate 0.01-0.05 nm/s, 2 x 10^{-6} mbar) onto a freshly cleaved mica sheet. The gold surface is then annealed by heating the mica sheet at 650 °C for 45 s to form Au(111). The gold surface is then glued with EPO 377 to a glass slice and cured for 60 min at 150 °C. After cooling, the slide is detached from the mica sheet to expose the TSG film.
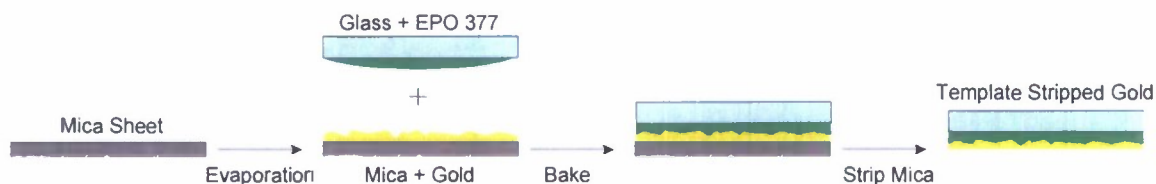
Figure 7. The preparation of template stripped gold (TSG) electrodes.

To produce the tBLM, Figure 8, TSG slides are placed for 24 h in an ethanolic solution of ~0.02 mg/ml of the tethered lipid, rinsed in pure ethanol, and dried in a stream of nitrogen. Afterward, liposomes, prepared from DPhPC (1,2-Diphytanoyl-sn-Glycero-3-Phosphocholine) by extrusion through 50 nm polycarbonate filters, were added to the solution. Fusion of vesicles was carried out at 30 °C at a final concentration of 0.02 mg/mL. EIS spectra were recorded also in a solution of NaCl 0.1 mol/L.
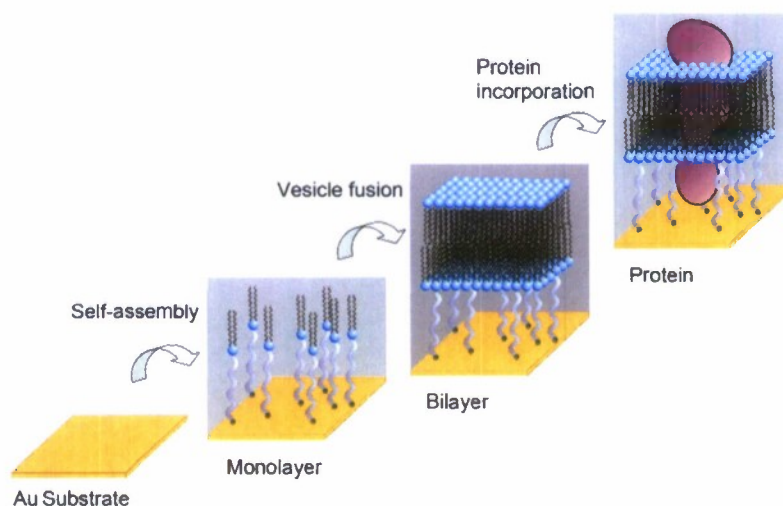
Figure 8. Formation of the tBLM on the TSG surface.

The tBLM on TSG, Figure 9, is incorporated into an apparatus that allows for simultaneous surface Plasmon resonance (SPR) and electrical impedance measurements. SPR is used to monitor the growth of the tBLM. The primary measurement we will be concerned with is the measurement of the electrical impedance of the tBLM on the TSG. The device provides a tight seal at the edge of the tBLM by the simple use of an o-ring between the Teflon cuvette and the glass slide. The relative large size of the TSG electrode (over 0.5 cm in diameter) allows for the use of relatively simple methods to seal the edge of the tBLM.
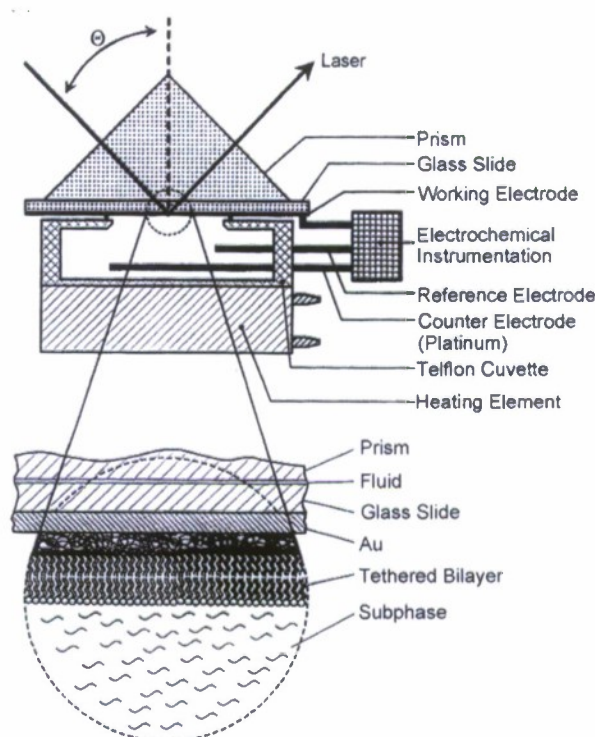
Figure 9. Experimental set-up based on a surface plasmon spectrometer combined with an electrochemical/impedance spectroscopic module for the simultaneous characterization of structural and functional features of tethered bimolecular lipid membranes. The enlargement shows the solid/solution interface with the thin Au layer used for surface plasmon excitation, the tethering layer and the lipid bilayer in contact to the aqueous buffer phase

The resulting tBLMs have very high intrinsic resistance. As we see in Table 1, the resistance of the tBLM on TSG is ~1000X greater than the resistance of the tBLM on polycrystalline gold. This large increase in resistance significantly improves the ability to measure ion channel conductance.

	$C_m(exp)/\mu F \cdot cm^{-2}$	$R_m(exp)/M\Omega \cdot cm^2$
DPTL, monolayer on TSG before vesicle spreading	0.71−0.80	3.1−4.9
lipid bilayer on TSG after vesicle spreading	0.64−0.72	18−71
lipid bilayer on TSG after vesicle spreading, + valinomycin and 6.89 mM KCl	0.84−1.1	0.0023−0.0026
DPTL, monolayer on polycrystalline gold before vesicle spreading	0.9	0.029
lipid bilayer on polycrystalline gold after vesicle spreading	0.9	0.043

Table 1. Comparison of the capacitance and resistance of tBLMs on TSG and polycrystalline gold [15].

3.1.3. Development of Tethered Lipids

Under the MOLDICE program, MPI has developed two new tethered lipids. Each of these has a hydrophobic diphytanoyl tail to match up with the phospholipid, DPhPC. A general purpose method for the synthesis of these tethers was developed by MPI under the current program and is described in detail by Atanasov et al [16].
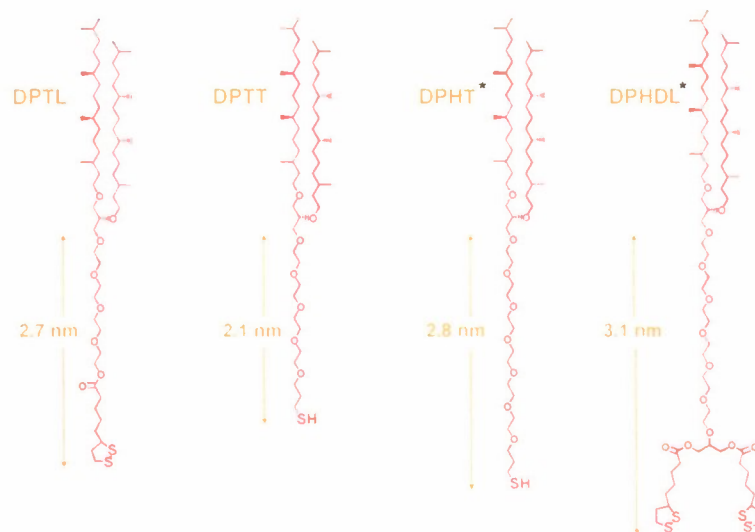
Figure 10. Phospholipid tethers developed by MPI. Tethers denoted by a (*) were developed on the current program.

3.1.4. Incorporation of αHL in tBLMs

In order to use the tBLM on gold for stochastic sensing, it will be necessary to incorporate recombinant protein pores to act as the sensing element. To this end, MPI evaluated the ability of αHL to incorporate into the tBLM on TSG platform. The EIS results are shown in the Bode plot of Figure 11. The step in the impedance occurs at ~8 MΩ for the bilayer. With the addition of 64 nM αHL, the resistance decreases by ~400X. Increasing the concentration further reduces the resistance of the tBLM. It is clear that the αHL is incorporating into the tBLM and providing a low resistance path across the tBLM. The very low resistance of the tBLM in this case, however, does not allow for the measurement of single ion channel.
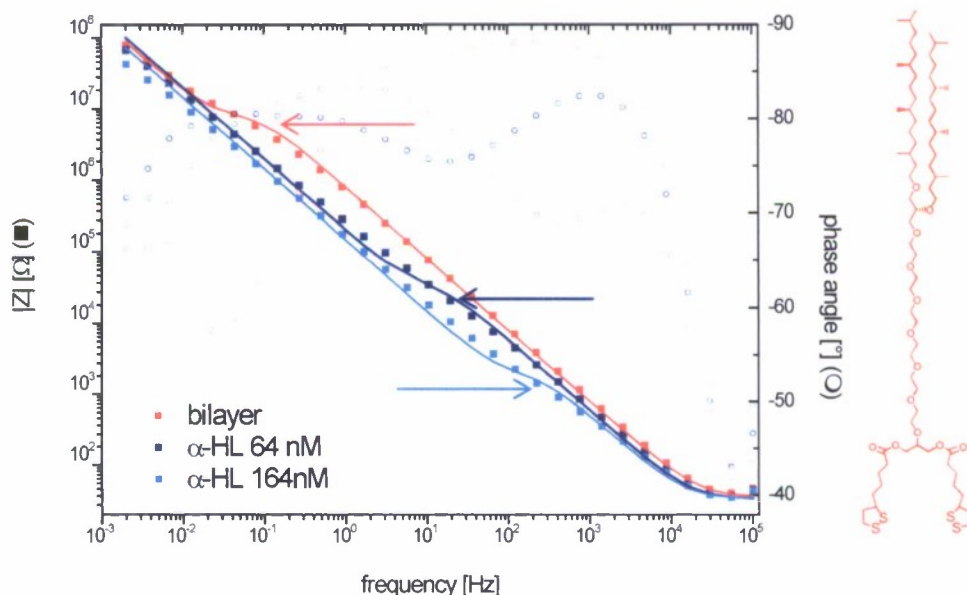
Figure 11. Incorporation of αHL into tBLMs on TSG electrodes.

3.1.5. Long term stability of tBLMs on TSG electrodes

To investigate the electrical stability of a tBLM, five membranes were prepared in identical Teflon cells. The measurement cell provides an aqueous reservoir above the membranes. The electrical properties were measured using EIS, Figure 12. In between the measurements, the cells were closed and stored at room temperature.
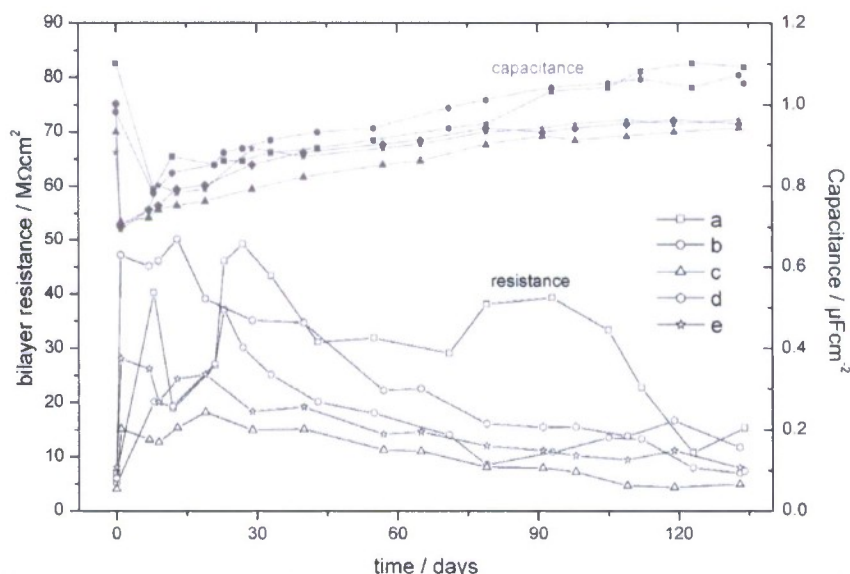
Figure 12. Long term monitoring of tBLM resistance and capacitance for 5 separate devices.

The resistance values for the different monolayers showed some variability, but they were all in the range of 3–10 MΩ cm^2 and increased to 10–50 MΩ cm^2 during vesicle fusion. Bilayer formation was also associated with a large drop in capacitance for all samples. Throughout the measurements, the bilayer resistance remained fairly stable for two of the samples (c and e). Two fluctuated but remained at a high level above 5 MΩ cm^2 (a and b), while one showed a decrease in resistance (d). In all cases, the resistance after 4 months is still higher than the initial monolayer resistance. Over the same time course, the bilayer capacitances increased steadily with time, but even after about 60 days the values remained so low (below the starting value of the monolayer), to be consistent with a tightly sealing membrane. From 60 days onward, two of the electrodes (b and e) showed a capacitance higher than the value of the monolayer, indicating a slow decay of the membrane sealing properties. Nevertheless, three of the samples were below 1 μF cm^{-2}, and all samples remained below 1.1 μF cm^{-2}.

The reason for the fluctuations is unclear, however, even after 3 months all membranes showed resistances above 10 MΩ cm^2, whereas the membrane capacitance showed a slight and continuous increase over the whole time. This might be due to several processes. The electrolyte solutions were neither sterilized nor were any chemicals added to prevent biodegradation. There might have been slight biocontamination, e.g., with enzymes that slowly digest the membrane. At the same time, a small amount of lipids might have been dissolved in the electrolyte. The critical micelle concentration is small, but not negligible. Nevertheless, after 3 months all four membranes are still tightly sealing with capacitances around 1 μF cm^{-2}.

One of the membranes was stored at room temperature for a total duration of 228 days. After that period, the membrane resistance was still about 3 MΩ cm^2, Figure 13. In order to test

whether the membrane was still functional, its response to incubation with valinomycin was investigated. Valinomycin is a small peptide that selectively transports potassium ions across membranes. The addition of the peptide to the membrane led to a drastic decrease in the membrane resistance to 50 MΩ cm^2.
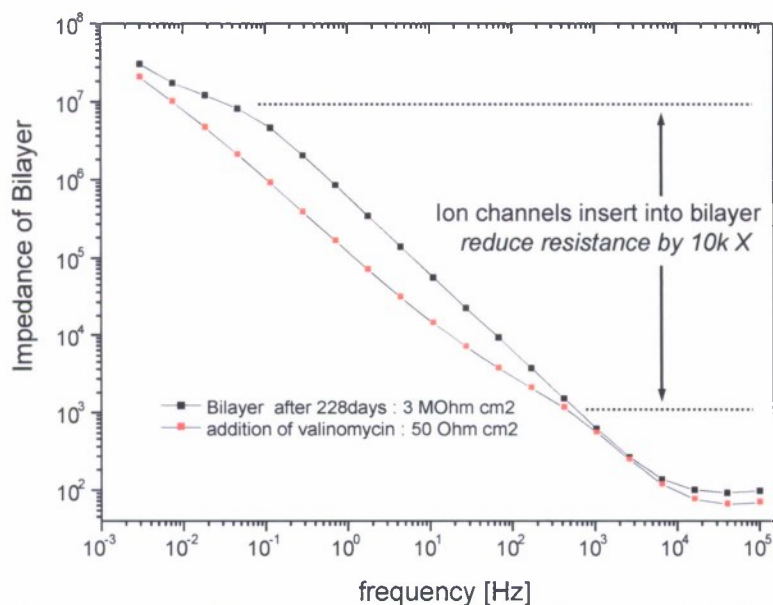
Figure 13. Demonstration of functionality of a tBLM on TSG stored for 7 ½ months in ambient conditions.

In all of the previous lifetime tests, the tBLM has been kept submerged in an electrolyte solution. Ideally, we would like to be able to store the devices in a relatively dry state and rehydrate when needed. This is complicated by the fact that lipid membranes are typically destroyed when exposed to air. To stabilize the tBLM, MPI investigated the benefit of coating a tBLM with a poly(NIPAAM) hydrogel. A 2–3 mm thick layer was polymerized in situ on the membrane. Initially, the electrical properties of the membrane are perturbed. However, they recovered to values of about 1.5 MΩ cm^2, which is slightly lower than for membranes without hydrogel coating (typically >10 MΩ cm^2). However, the experimental data cannot be well described in an equivalent circuit model consisting of ideal capacitive and resistive elements. This might be due, for example, to a distribution of capacitive elements. Nevertheless, in order to perform a consistent comparison, we used the same equivalent circuit throughout. When an unprotected membrane is left to dry and is rehydrated after 24 h, the membrane is modified such that the electrical sealing properties are no longer present. In contrast, the hydrogel covered membrane could be dried for 24 h and regained its electrical properties after rehydration, Figure 14. Apparently, the hydrogel keeps a sufficient amount of water in its network structure to keep the underlying membrane hydrated, and therefore functionally intact. The results are promising and indicate that it may be possible to store tBLMs on gold electrodes for extended periods prior to use.
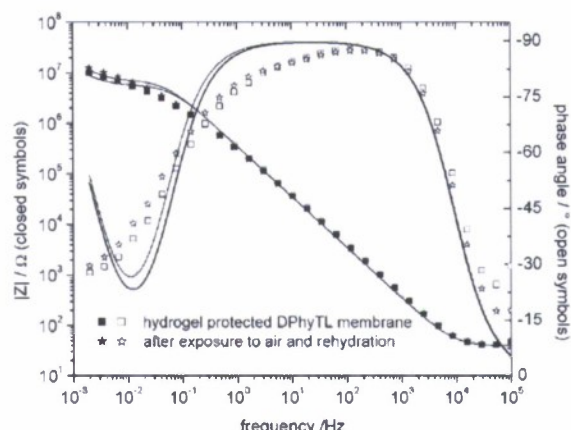
Figure 14. Rehydration of hydrogel protected membrane.

3.1.6. Limitations of the tBLM on TSG Platform

The TSG electrodes as developed by MPI are inherently quite large (~0.5 cm in diameter). This is a beneficial feature when characterizing the resistance and capacitance per unit area of the tBLMs. In particular, the large area tBLMs formed on TSG are relatively easy to seal at the edge. An example of the apparatus used by MPI to study tBLMs on TSG is shown in Figure 9. The sealing at the edge of the tBLM is achieved by a small o-ring placed between the Teflon cuvette and the glass slide.

Unfortunately, such large area tBLMs will not allow for the measurement of a single channel current necessary for stochastic sensing. A realistic readout system will have a noise voltage of 10 nV/rtHz. This noise voltage is transformed into a noise current via the capacitance of the electrode. At 1uF/cm2, the capacitance of a 0.5 cm diameter electrode is 5 µF. This translates into a noise current of > 10 nA/rtHz at 10 kHz. For a 1GΩ ion channel (e.g. αHL in 1M KCl) the total current at a 100 mV bias is only 100 pA; bias levels ~2X greater than 100 mV are possible with αHL, but the protein will frequently gate at high bias [17]. In order to have a current noise at least 10X less than the expected current through the 1 GΩ ion channel (i.e. less than ~10 pArms), the diameter of the electrode must be reduced by ~100X to 50 µm. It is not possible to create such a small electrode using the TSG method described above, so we have worked on developing alternative methods to produce ultraflat gold electrodes that can have very small dimensions.

3.1.7. tBLMs on a Chip

EBS performed a careful analysis of the overall circuit associated with the tBLM on a microelectrode. Physical and electronic schematics are shown in Figure 15.
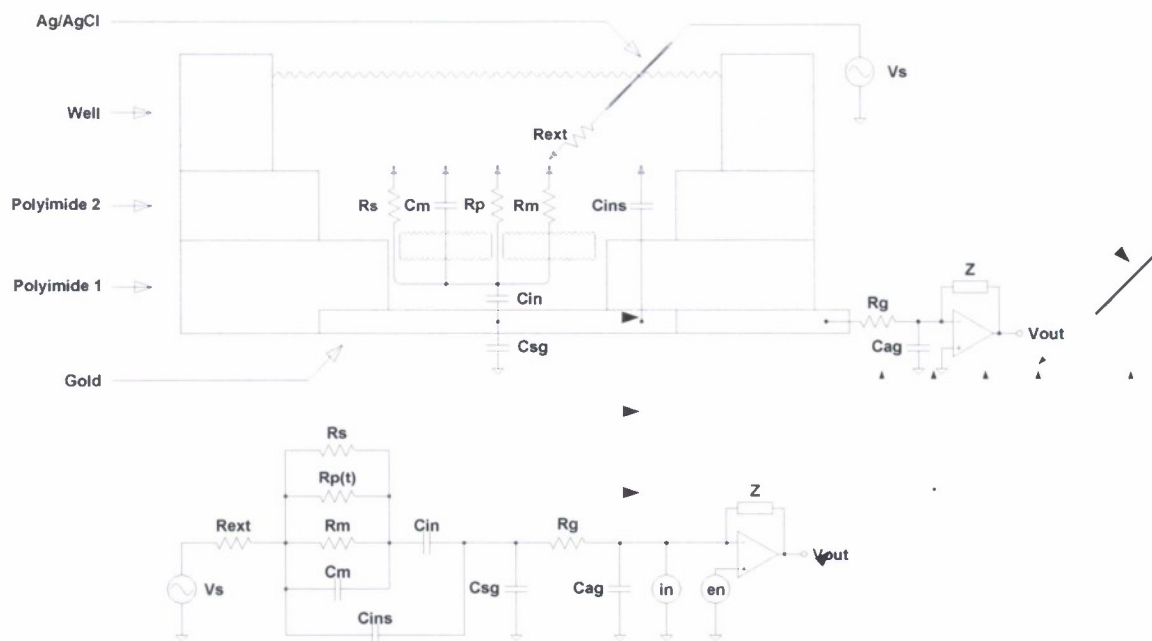
Figure 15. (Top) Physical schematic of the circuit elements associated with a tBLM on a micro gold electrode. Polyimide is used to seal the edges of the electrode. (Bottom) Electronic circuit schematic with all parasitic element and noise sources.

The electronic system shown in Figure 15 has been modeled by EBS to determine the sensitivity to current flow through the ion channel. For a 25 µm diameter electrode the SNR for the full current through the pore is ~120 at a seal resistance of 1 GΩ. Above a few GΩ the SNR flattens out due to the limiting effect of the electrode capacitance.
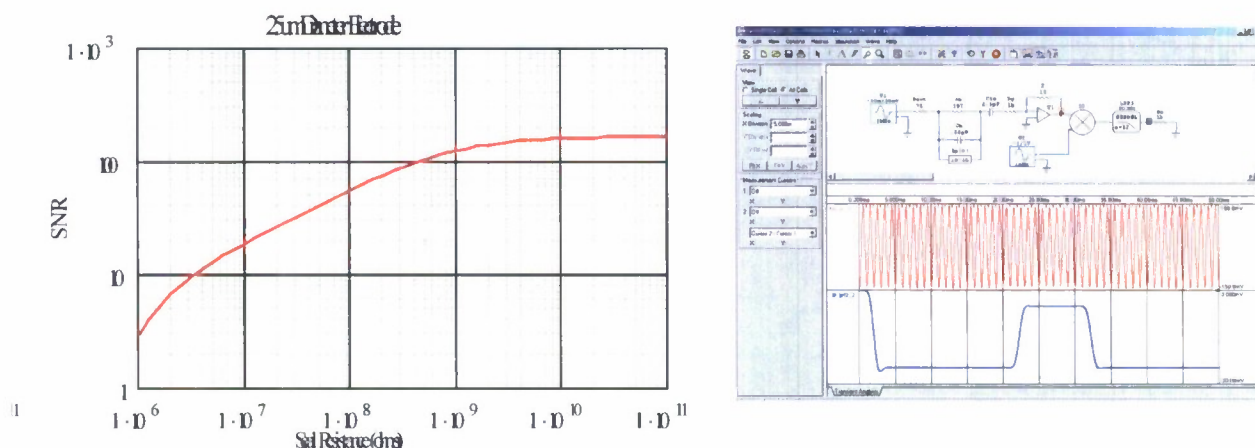
Figure 16. (Left) SNR for the measurement of current through αHL in 1M KCl on a tBLM attached to a 25 µm diameter electrode. (Right) Circuit model and results used to estimate SNR.

In order to produce gold electrodes with diameters below 50 µm EBS and the UT Austin developed a design for an electrode produced by semiconductor manufacturing methods integrated with the readout electronics. By incorporating the readout electronics on the same substrate as the gold electrode, it is possible to minimize stray capacitance that will limit the

performance of the system. The basic design for the electrode and circuit layout is shown in Figure 17.
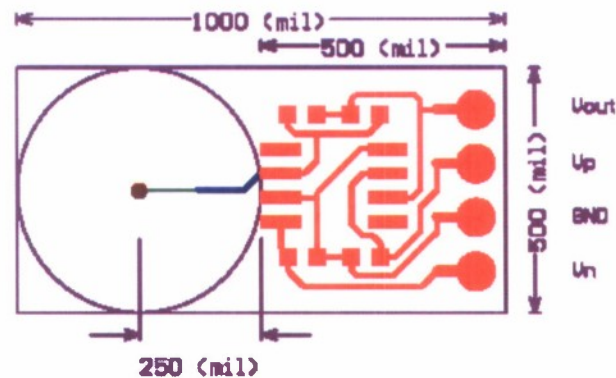
Figure 17. Printed circuit layout for gold electrode integrated with readout electronics. Reference electrodes not shown.

In the first approach attempted, UT Austin produced a circuit and electrode layout with no protective seal around the edge of the gold electrode (as shown by Polyimide 1 in Figure 15). Simple evaporation of gold on a silicon or silca surface has been shown to produce relatively low resistance bilayers[15]. In order to produce gold electrode with a surface roughness less than ~ 1 nm rms, UT Austin developed a multi-layer process. Microelectrodes were produced by evaporation of 3 nm of Ti followed by 50 nm of a 60% Au/40% Pd alloy on a silicon/silicon dioxide substrate (cleaned in piranha prior to evaporation) pre-patterned to the desired structures with photoresist. A 20 nm layer of pure gold was deposited on top of the alloy to form the surface of the pad. The pre-patterning process is described graphically in Figure 18. The completed electrode and circuit is shown in Figure 19.
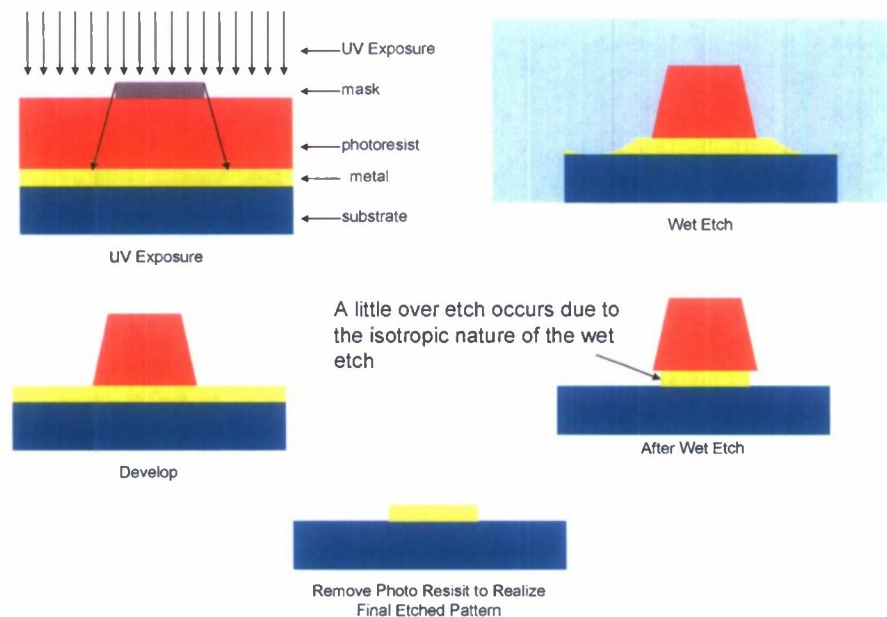
Figure 18. Patterning of electrode and circuit elements.
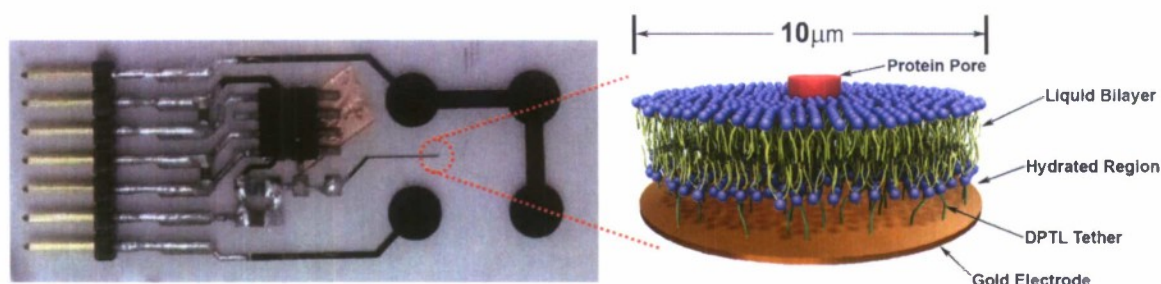
Figure 19. Completed gold electrode and measurement circuit on a quartz substrate. The electrode itself is 10 μm and circled.

The leads connecting the electronics to the electrode was masked using a polyimide tape and a test well was formed using a Teflon cell. Monolayers of DPhyTL (2,3-di-O-phytanyl-glycerol-1-tetraethylene glycol-D,L-lipoic acid ester lipid) were prepared on the gold electrodes via self-assembly from an ethanolic solution of the thiolipid. DPhyTL consists of two phytanyl lipids connected via a tetraethylene oxide chain to a lipoic acid anchor group. Monolayers were measured by impedance spectroscopy to determine their electrochemical properties. (All measurements were performed in 0.1 M KCl solution.) After addition of small unilamellar vesicles (1,2-di-O-phytanoyl-sn-glycero-3-phosphocholine, DPhyPC, Avanti Polar Lipids, 50 nm by extrusion), a series of scans were taken.

The results for the unprotected electrode are shown in Figure 20. No distinct plateaus are evident in either the monolayer impedance or the bilayer impedance. This indicates that there are significant defects in the monolayer and bilayer. It is likely that the unprotected edge of the electrode is the cause of the poor monolayer and bilayer formation. The next step is to use a polyimide coating to cover the edges of the electrode.
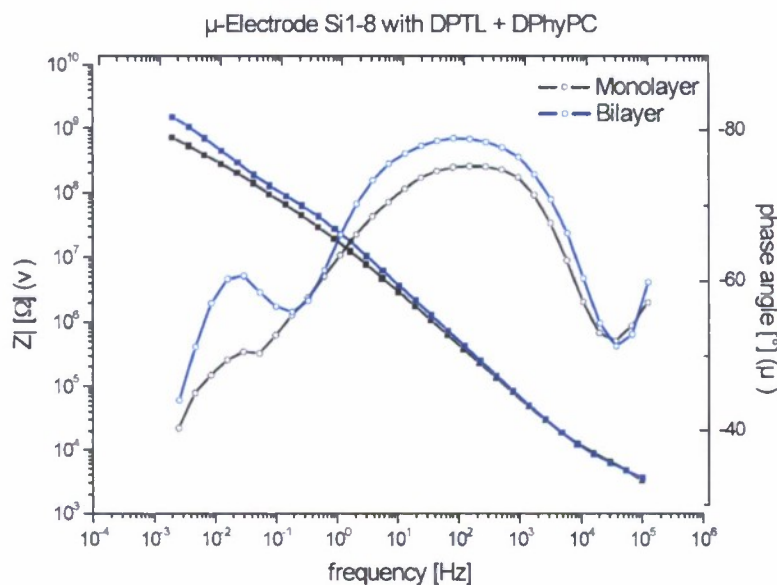
Figure 20. Electrical impedance results for an unprotected micro electrode.

A polyimide resist (PI-5878G, HD Microsystems) was photolithographically applied in order to define the pad size and to prevent back-coupling to the underlying substrate via the exposed edges of the sensing pad. Electrodes with window openings from 4000 μm to 8 μm were produced. The process used to apply the polyimide coating to protect the edges of the electrode is shown in Figure 21.
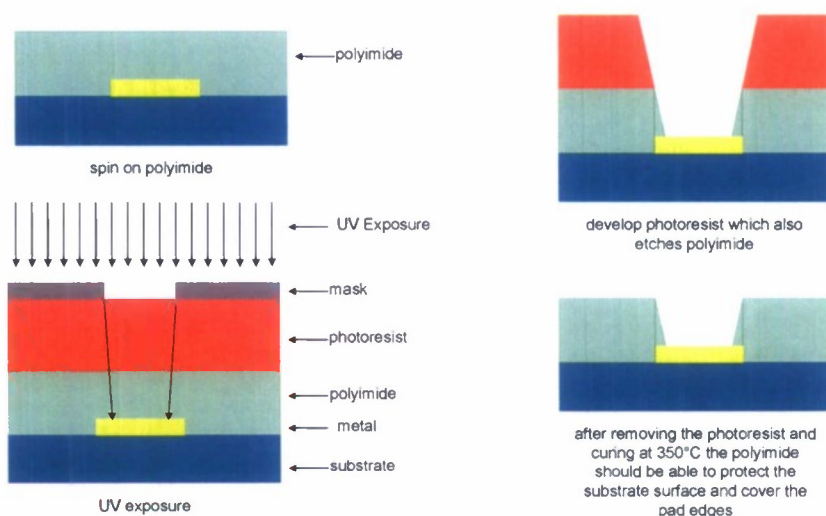
Figure 21. Application of polyimide coating around the gold electrode.

The topology of the electrodes was investigated using AFM techniques. Both topography and phase image show the well-like structure of the electrode window in the polymer coating Figure 22A. The thickness of the polyimide film around the electrode pad was about 3 µm Figure 22B. The roughness of the active electrode area was determined by a scan with higher resolution on a smaller area inside the well Figure 22C. The roughness was 1.08 nm over an area of 5 µm^2, which is by a factor of 2 larger than the gold surfaces used in former studies [15] and might cause non-ideally sealing membranes.
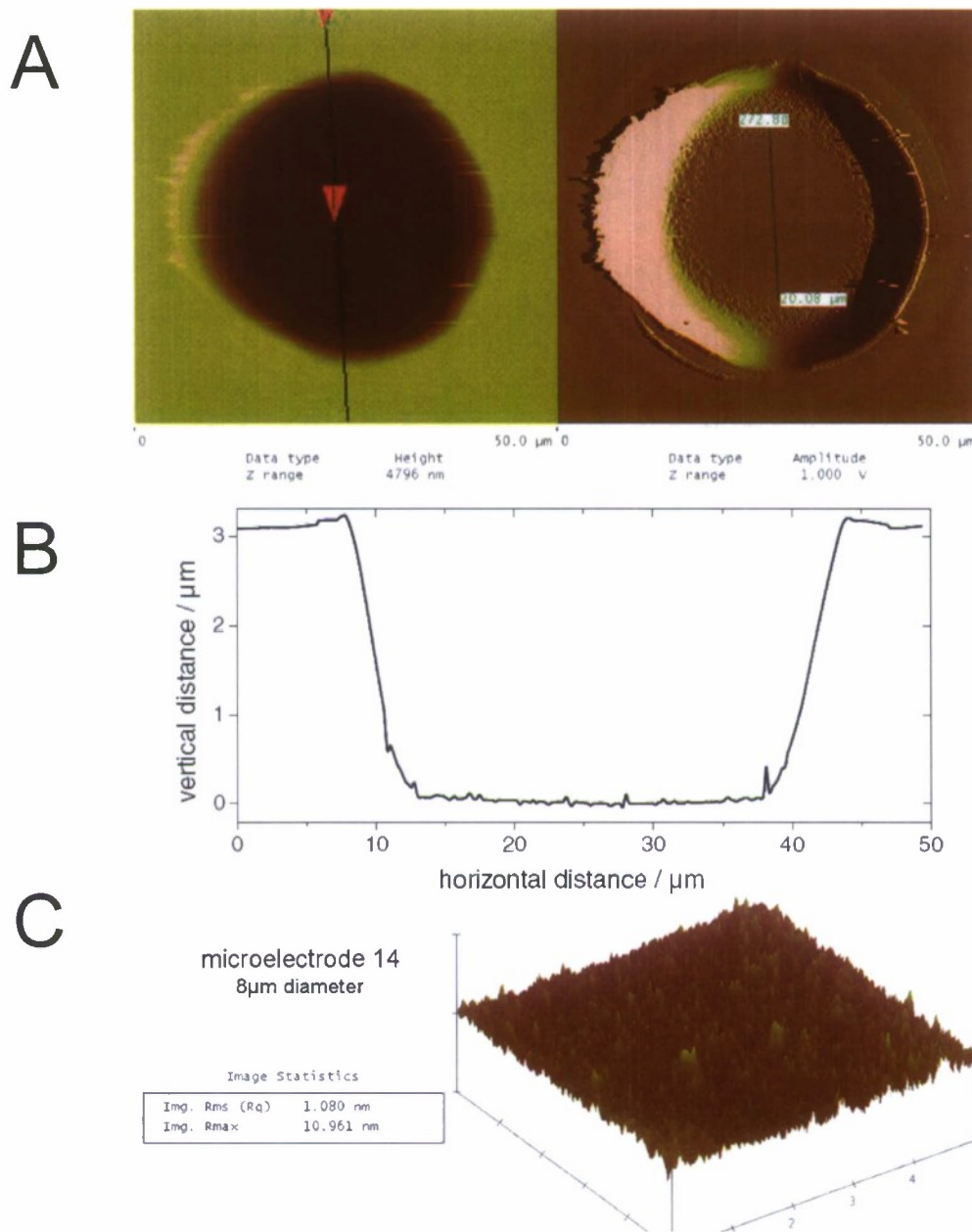
Figure 22. (A) AFM topography and phase image of an electrode with 20 mm diameter. The polyimide coating forms a well-like architecture around the open electrode window. (B) Linescan across electrode showing 3 μm depth of polyimide coating. (C) High resolution surface scan showing 1.08 nm surface roughness of the gold electrode.

Electrodes were functionalized with a tBLM and the electrical properties of both mono- and bilayer were analyzed as shown in Figure 23. As mentioned above, if the capacitance is too high or dominated by the underlying support, no high SNR measurements of transmembrane currents are possible.

The capacitance of a DPTL monolayer was measured for 2–7 samples per electrode size (Figure 23 left). For a 4000 μm diameter electrode, the absolute capacitance is around 1 μF. It decreases constantly to a value of 0.47 nF for the smallest electrodes (8 μm). For large

electrode sizes, the capacitance values scale quadratic with the electrode diameter, while a linear trend can be seen for the small electrodes. By extrapolation, a lower limit of about 0.46 nF for the investigated electrodes can be found. This value is probably determined by the stray capacitance of the underlying support. The different dependence of the capacitance on the electrode size (quadratic and linear) indicates that at large areas the capacitance is dominated by the electrode area, while at smaller electrode sizes, the circumference seems to have the dominant effect.
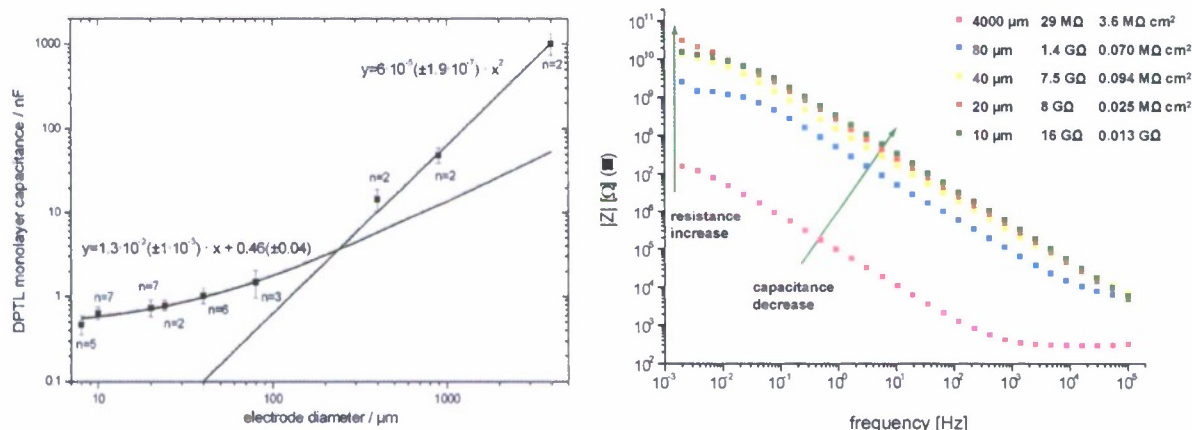
Figure 23. (Left) Capacitance of DPTL monolayers and (Right) resistance of tBLMs on gold electrodes ranging from 4000 to ~10 µm in diameter.

A similar trend can be seen for the lipid bilayers. On the right of Figure 23, the impedance spectra of bilayers on electrodes with diameters ranging from 4000 µm to ~10 µm are plotted. The membrane on the largest electrode (4000 µm) has the lowest resistance (29 MΩ) and highest capacitance (1.1 µF) and also shows an electrolyte resistance in the high frequency range. With decreasing electrode size, the spectra shift upwards towards smaller capacitances and larger resistances. The membrane on the 80 µm electrode has already an absolute resistance in the giga-ohm range. For the even smaller electrodes the resistance increases further until a resistance of 16 GΩ for an electrode with a diameter of 10 µm.

Similar to the monolayer capacitances, the bilayer resistance scales, at least for the small electrodes, linearly with the electrode diameter. This implies that changes in the circumference to area relation dominate the sealing properties of the bilayer. At large electrode sizes, the edge of the bilayer does not play a major role, while for small sizes already a slight disordering of the mono-/bilayer structure at the edges of the electrode can have a major influence on the electrical properties of the membrane. To conclude, even though the bilayer resistances on the small electrodes are in the giga-ohm range, as commonly reported in BLM experiments, they are no longer in the $M\Omega \cdot cm^2$ range, used before to characterize supported bilayer membranes on macroscopic electrodes.

Into the same tBLMs, αHL was incorporated by addition of a small aliquot to a preformed bilayer of a resistance of 5.5 GΩ. As shown in Figure 24, the membrane resistance decreased by over three orders of magnitude to a value of 1.5 MΩ. This is even lower than the initial monolayer resistance showing the ability of the protein to penetrate through the whole bilayer. While the electrical parameter of mono- and bilayer could be analyzed using a single RC-element, a second RC-element had to be introduced to describe the protein-doped membrane.
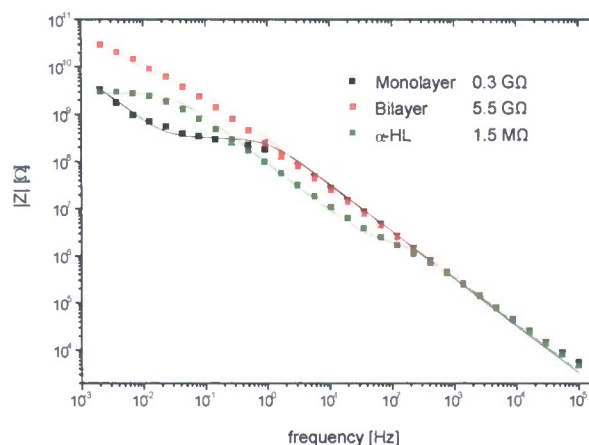
Figure 24. Electrical impedance of monolayer, and tBLM on a 20 μm diameter electrode before and after incorporation of αHL. Electrolyte: 0.1M KCl.

Although we were successful in incorporating αHL into tBLMS on micro electrodes, the quality of the bilayers appears to be poor resulting in larger than acceptable capacitance values (>600 pF) and lower than acceptable resistance values (< 16 GΩ) for the smallest 10 μm diameter electrodes. The quality of the gold surface appears to be good in light of the high seal resistance for the 4000 μm electrode, 3.6 MΩ·cm^2. Some problem with either the edges of the gold electrode or the polyimide coating compromises the seal resistance around the circumference of the electrode and makes the small electrodes unsuitable for single channel measurements.

3.2. The Suspended Bilayer

Although the supported bilayer platform is quite attractive in light of the bilayer robustness, single channel measurements have not been demonstrated in a reproducible manner. Traditionally, single channel measurements are made using a bilayer that is suspended across an aperture with electrolyte baths on both sides [18, 19]. An example is shown in Figure 25.
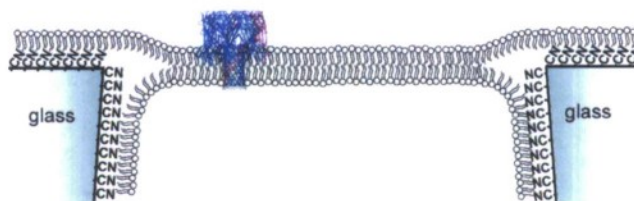
Figure 25. Suspended lipid bilayer with inserted ion channel.

The primary difficulties with traditional suspended planar lipid bilayers derive from the typical diameter of the lipid bilayer membrane, ~150 μm diameter. The large area leads to fragile bilayers, noise interference from vibration and large thermal noise due to the large capacitance of such bilayers. The solution is to produce small diameter (< 2 μm diameter) bilayers on a solid support.

At the onset of the program we investigated the use of Kapton films that have been track etched to produce sub-micron apertures. Due to the inability to obtain the necessary films, we quickly abandoned this approach and began to pursue the development of suspended bilayer platforms in silicon and glass (as well as quartz). The two substrates require radically different approaches and ultimately the glass platform was chosen for further testing.

3.2.1. Silicon Nanopores

Arizona State University (ASU) led the silicon nanopore development effort. The goal was to produce nanopores in silicone, demonstrate lipid bilayer formation and channel insertion (with the assistance of other groups on the MOLDICE team), develop a device to isolate individual elements of the array and construct a prototype microfluidics system for stochastic sensing of a model analyte. The ASU team succeeded in developing the silicon nanopore fabrication method, but issues with surface roughness and then spontaneous blocking of the silicon nanopores prevented the ultimate demonstration of stochastic sensing with these devices.

3.2.1.1.   Fabrication of the Silicon Nanopores

The fabrication process of the cylindrical nanopore is based on a silicon-on-insulator (SOI) substrate using two mask steps and was carried out at the ASU Center for Solid State Electronics Research Facility [20, 21]. The first step in the process is to define and etch the nanopore in the device layer of the SOI wafer, followed by the alignment and etching of a larger opening from the backside of the handle wafer to reach the buried oxide layer.

Samples were prepared with double-sided-polished 100 mm diameter SOI wafers with a 340 nm device layer, a 1 µm thick buried SiO_2 layer and a 450 lm thick p-type handle wafer (Figure 26a). A 60 nm layer of silicon dioxide (SiO_2) was thermally grown in a dry oxygen atmosphere at 1000 °C for 60 min to function as a hard mask for etching the device layer (Figure 26b). This oxidation consumes about 30 nm of the device layer resulting in a top silicon thickness of approximately 310 nm which was verified via ellipsometry using a Woollam WVASE32 variable angle spectroscopic ellipsometer.
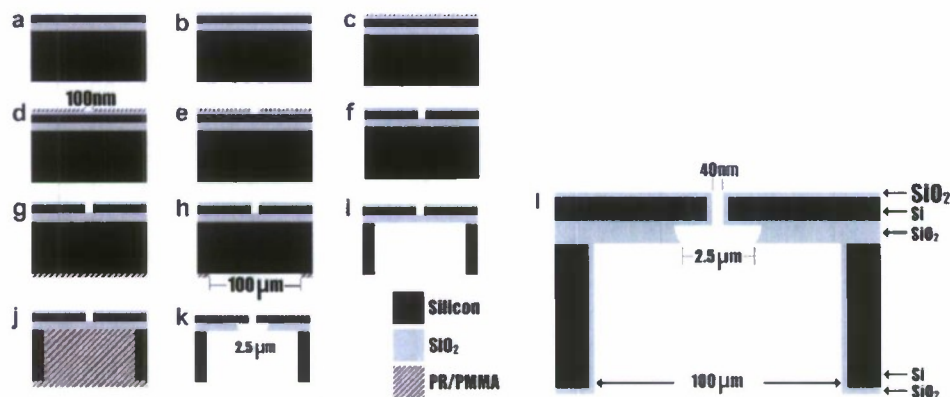
Figure 26. Silicon nanopore fabrication process.

The device layer was spin coated with 3% polymethyl methacrylate (PMMA) in methoxybenzene at 5000 rpm to obtain a film thickness of 100 nm. The PMMA was soft baked at 175 °C for 15 min on a hot plate (Figure 26c). Electron beam lithography (EBL) was used to pattern either single circles or arrays of circles in a JEOL JBX-6000FS/E EBL system with a typical area dose of 460 µC cm^{-2}. The patterns were developed in 11:10:1 MIBK:CS:MEK diluted in IPA, ethanol and methanol solvent for 20 s at 23 °C, rinsed in isopropyl alcohol and blown dry with nitrogen gas (Figure 26d). The openings in the PMMA are transferred to the SiO2 hard mask by reactive ion etching (RIE) using an Oxford Instruments Plasmalab 80 + RIE tool (Figure 26e). The etch used a 1:1 CHF_3:Ar chemistry for 20 min at a power of 25 W. These etch conditions were chosen because they resulted in better than 1:1 selectivity between the PMMA and SiO_2. The etch rate was relatively slow (60 Å/min) to provide accurate control of the etch depth. The top silicon device layer was then etched utilizing the SiO_2 hard mask in an inductively coupled

plasma (ICP) RIE at 500 W coil power, 50 W platen power with 10 sccm of Cl_2 for 2 min using an advanced general etch tool from Surface Technology Systems (Figure 26f). Chlorine chemistry was chosen because it resulted in the most cylindrical pores that in turn led to higher packing density. Fluorine chemistries, CF_4 and SF_6, were also explored, but resulted in gross enlargement of the patterned hole. For example, an EBL patterned 100 nm diameter pore was enlarged to 300 nm and 600 nm for CF_4 and SF_6, respectively.

After etching the nanopore in the front side of the SOI layer a 100 μm opening in the back side was etched though to the buried oxide layer. AZ4620 positive photoresist was spin coated at 2500 rpm on the front side of the wafer and baked in an oven at 120 °C for 5 min. The backside of the wafer was then cleaned in diluted hydrofluoric acid, 1:4 HF 49% to water, to remove any SiO2 on the backside. The wafer was then immersed in heated AZ 400T photoresist stripper at 100 °C for 5 min to remove the AZ4620 from the front side of the wafer. The device layer was recoated with a new layer of AZ4620, at 2500 rpm and baked at 120 °C for 5 min in an oven, to protect the surface while processing the backside. The backside of the wafer was spin coated with AZ4620 at 2500 rpm and soft baked at 90 °C for 90 s on a hot plate (Figure 26g). Backside photolithography was then completed, utilizing features patterned via EBL on the front side as reference alignment markers, to pattern 100 μm circles vertically opposite the 100 nm circles on the device side using an EV Group 620 Mask Aligner (Figure 26h).

After patterning, the backside opening was etched in a deep reactive ion etcher (Surface Technology Systems, Advanced Silicon Etcher) using the Bosch process with 600 W coil power, 12 W platen power, 136 sccm of SF_6 for 14.8 s for the etch phase, and 600 W coil power, 2 W platen power, 90 sccm of C_4F_8 for 7.0 s for the passivation phase, for a total of 435 cycles to contact the buried SiO_2 layer (Figure 26i). Once the etch was completed, the wafer was cleaned in heated AZ400T for 5 min followed by piranha solution, H_2SO_4 and H_2O_2 at 1:1 ratio, for 5 min.

At this stage in the processing the nanopore on the front side of the wafer is separated from the larger opening in the backside by the buried oxide (BOX) layer. To connect the two sides of the wafer, the BOX layer needs to be removed in the vicinity of the nanopore. It was desired to keep the size of the opening small because the thick BOX layer improved the robustness of the silicon membrane and reduced the overall capacitance. The wafer was immersed in a buffered oxide etchant (BOE 20:1) for 60 min with the backside opening sealed, which resulted in the etching of the BOX layer only through the top side nanopore (Figure 26j and k). Upon completion of the etch, the wafer was cleaned in heated AZ400T for 5 min followed by piranha solution, H_2SO_4 and H_2O_2 at 1:1 ratio, for 5 min.

The wafer was then placed into a thermal-oxidation furnace to grow a layer of SiO_2. Typically a 60 nm thick layer of thermal SiO_2 was grown at 1000 °C for 60 min in a dry oxygen atmosphere. Thermal oxidation processes are conformal; therefore the film grows on the sidewalls of the pore, and in turn controllably reduces its diameter (Figure 26l). The amount of SiO_2 grown in the final oxidation step can be adjusted to achieve the desired final pore diameter.

Upon completion of the final thermal oxidation step, the wafer was spin coated on both sides with AZ4620 and baked in an oven at 120 °C for 5 min. The wafer was then scribed into 1 cm-by-1 cm square devices, that were later mounted for conductance measurements and imaging. The individual die were immersed in heated AZ400T for 5 min followed by piranha solution, H_2SO_4 and H_2O_2 at 1:1 ratio, for 5 min. Devices were either stored in 1:1 IPA:water solution or dried in a super critical CO_2 drier (Tousimis 815B). The super critical CO_2 drier was used because it was found that drying under nitrogen resulted in surface contamination in the area

around the front side of the nanopore, which is believed to be a result of evaporation of fluid collected in the buried SiO_2 cavity.

A FESEM cross section of a completed nanopore is shown in Figure 27. This particular image is from a pore that is a member of a large array on a 4 μm pitch to allow scribing for imaging and to retain robustness; the back side of the handle wafer was not etched underneath this array of pores to allow manual scribing. The silicon handle wafer can be seen below the cavity in the buried SiO_2 layer. This pore was patterned using EBL with a 100 nm initial diameter and thermally oxidized to grow 60 nm of SiO_2, resulting in a final pore diameter of 40 nm.
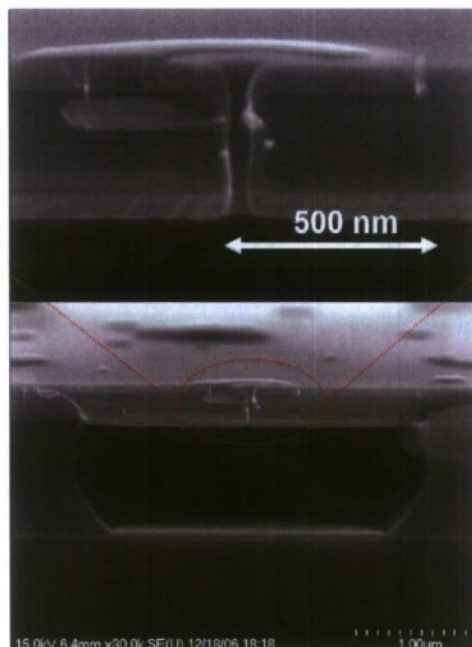
Figure 27. (Below) Cross-sectional scanning electron micrograph of a single nanopore after the completion of the fabrication sequence. The patterned diameter of the nanopore was 100 nm with a final dry oxidation of 60 nm. The handle wafer was not etched to provide structural support for scribing. (Above) a higher magnification image of the pore region.

The preliminary conductivity measurements of numerous single nanopores in the solution have been completed for characterization purposes. To prepare a device for measurements, the 1-cm^2 die is mounted between two polytetrafluoroethylene wells using polydimethylsiloxane (PDMS) gaskets to provide a fluid tight seal. Prior to making measurements, a dry nanopore device must be filled, which was a nontrivial issue. To fill a nanopore with water, it is boiled for 1 h in deionized water and then degassed for up to 8 h in a desiccator. The initial condition of a device that is freshly filled with deionized water is its minimum conduction state, as compared with the electrolyte solution; therefore, KCl sweeps were always completed from the lowest concentration to the highest. Figure 28a shows the I–V traces of a 100-nm-diameter nanopore acquired via cyclic voltammetry using an Autolab PGSTAT302 for various unbuffered KCl concentrations ranging from 31.6 mM to 1M in half-log increments. The slope of the lines in the plot correspond inversely to the resistance of the pore. The larger the slope, the smaller the resistance. It is apparent in the graph that, as the concentration of the KCl solution is reduced, the resistance increases, as expected. Figure 28b shows a plot of the resistance of the single nanopores of different diameters measured with various higher concentration KCl buffer

solutions. The solutions (0.25, 0.50, 0.75, and 1.0 M KCl) were buffered with 20 mM N-(2-Hydroxyethyl) piperazine-N'- (2-ethanesulfonic acid) (HEPES) at pH 7.4. The points in Figure 28b represent measured data, while the solid lines represent the theoretical values of resistance calculated using the DeBlois approximation for a cylindrical resistance with an end-effect correction. It can be seen that the measured resistance very closely follows the calculated value of resistance, taking into account the end-effect approximation.
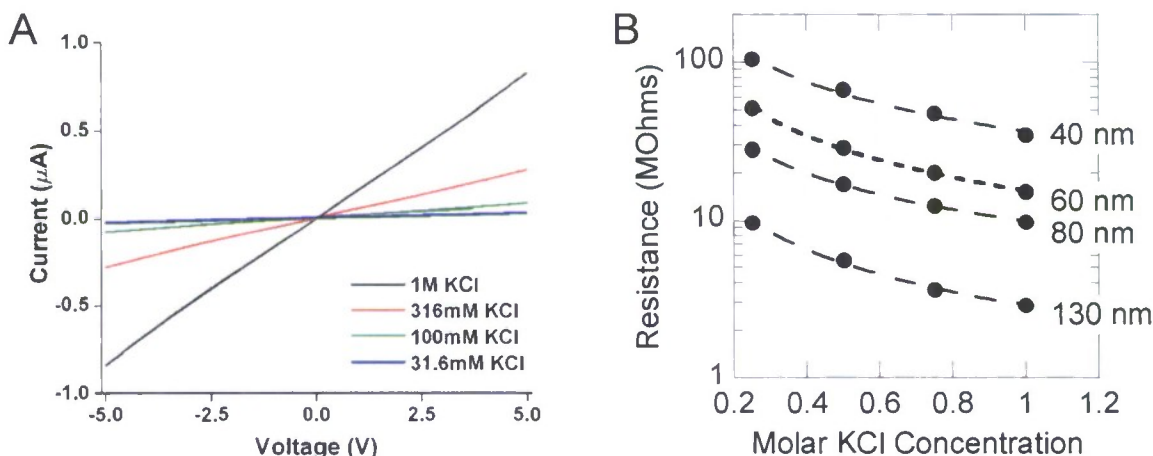
Figure 28. (A) Cyclic voltammograms for a single 100-nm-diameter pore at KCl concentrations of 1 M, 316 mM, 100 mM, and 31.6 mM. (B) Comparison of the resistances of nanopores with various diameters filled with 0.25, 0.5, 0.75, and 1 M KCl 20-mM-HEPES-buffered solution. The curves represent calculated values of resistance for a cylindrical nanopore with a length of 360 nm and the given diameter, taking into account end-effect corrections.

3.2.1.2.   Ion channel measurements

As described in the previous section, opening the silicon pores is a non trivial operation. For much of the project, we were unable to open the pores in order to make conductance measurements in preparation for making measurements of ion channel conductance. In addition, surface roughness of the silicon devices prevented bilayer formation in early runs. By the end of the program we continued to have difficulty forming the necessary bilayer/ion channel structure on the silicon nanopores in order to demonstrate the ability to make stochastic sensing measurements.

3.2.2. The Glass Nanopore Membrane (GNM)

In light of the difficulties encountered early on with the silicon nanopores, the MOLDICE team concentrated significant effort on the development of an alternative platform. The University of Utah group (Utah) had previously developed a glass nanopore electrode which consists of a 10-1000nm radius Pt disk electrode set into or just back from the face of a polished glass capillary [22]. This device was adapted to produce the glass nanopore membrane [23], ultimately shown to be a robust and reliable platform for stochastic sensing.

3.2.2.1.   Fabrication of the GNM

Fabrication of a disk electrode involves sealing an electrochemically sharpened Pt microwire into a glass capillary, followed by polishing the glass until a nanometer-sized metal disk is exposed. Complete removal of the wire yields a GNM, in which a conical-shaped pore is embedded in a thin (~50 μm) glass membrane.

A 2 cm length of Pt wire (99.95% pure, 25 μm diameter) was connected to a W rod using Ag conductive epoxy (DuPont). The Pt/W ensemble was heated in an oven at 120 °C for ~15 min to dry the Ag epoxy. The end of the Pt wire was electrochemically etched to a sharp point in 6 M NaCN/0.1 M NaOH solution following standard methods reported elsewhere [24, 25]. Briefly, a 100-300 Hz ac voltage (~4 V amplitude) was applied between the Pt wire and a large-area Pt electrode using an Agilent 33220A function/arbitrary generator. Bubbles formed at the metal/solution interface during electrochemical etching; the applied voltage was removed immediately upon cessation of bubbling and the sharpened wire was washed with H_2O.

The sharpened end of the Pt wire was inserted into a glass capillary (Dagan Corp. SB16, 1.65-mm o.d., 0.75-mm i.d., softening point 700 °C, manufacturer provided composition 67.7% SiO_2, 2.8% BaO, 15.6% Na_2O, 5.6% CaO, 4% MgO, 1.5% B, and 0.6% K_2O%), leaving ~3 mm between the tip and the end of the glass tube. The wire was then sealed into the glass tube by slowly softening the capillary in a H_2-O_2 flame (a simple H_2 and air flame is also satisfactory).

The glass nanopore membrane requires that the length of the Pt wire sealed in the glass capillary does not exceed ~100 μm. Sealing very short lengths (25-50 μm) of the sharpened end of a Pt wire is accomplished using a specialized procedure. First, the tip is positioned at the middle of the glass capillary to avoid touching of the glass walls while the glass is being heated in the H_2-O_2 torch. Initially, the Pt is positioned >0.5 cm from the end of the glass capillary while the end of the capillary is heated. As the capillary softens and collapses, the interior surface becomes very flat. At this point, the glass capillary is removed from the flame and the Pt tip is positioned as close as possible toward the sealed end of the capillary, taking care to avoid physical touching of the glass surface by monitoring progress with an optical microscope. The capillary is then placed back into the lower, cooler part of the flame to continue softening the glass with constant visual inspection of the interior flat surface. As the glass continues to soften in the flame, it eventually retracts and contacts the sharp Pt tip. This contact is observed by eye (with considerable practice) in real time by the sudden appearance of a spot at the point of contact. The capillary, with Pt tip sealed at the end, is immediately removed from the flame and allowed to cool. The sealed end of the capillary is inspected by optical microscopy (40X magnification) to ensure that the end of the tip is embedded in glass.

After obtaining an acceptable seal, the top of the W rod is secured to the glass capillary with epoxy (Dexter). Rough polishing to remove a large portion of the glass (i.e., leaving ~100 μm between the metal tip and the outside edge of the capillary) is accomplished using fine sand paper. Final polishing to expose the Pt or Au disk is performed using a Buehler Microcloth polishing pad mounted on a green glass plate with the aid of an electrical circuit as described below. The polishing cloth was wetted with a slurry of 50-nm Al_2O_3 particles and 0.02 M KCl.
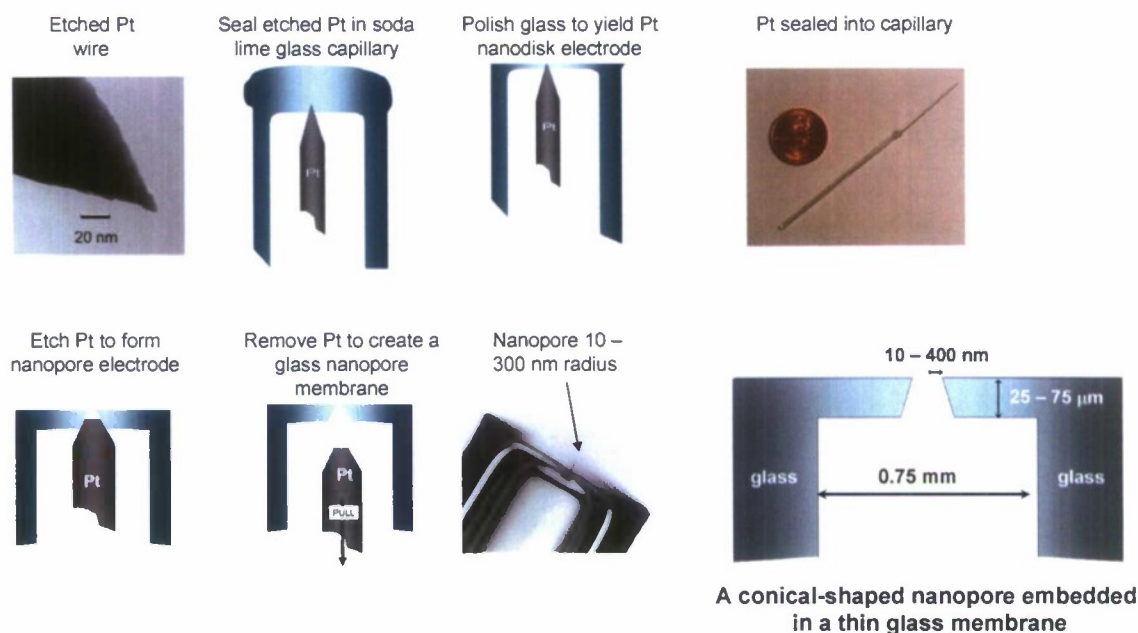
Figure 29. Fabrication steps for a glass nanopore membrane (GNM).

To aid hand polishing, a high-input impedance (MOSFET)-based electrical continuity circuit is used to signal the exposure of a metal disk of preselected size during polishing. Experimentally, the electrical resistance between the Pt wire sealed in glass and the felt polishing cloth (wetted with a KCl solution containing 50 nm Al_2O_3 particles and connected to the external circuit with a metal clip) is measured. The successful implementation of this strategy hinges on designing the circuit such that the user is alerted at precisely the moment a Pt or Au disk of desired radius is obtained during polishing. We performed a finite element analysis of the resistance between the Pt tip and the electrolyte solution [23]. The results of the analysis are shown in Figure 30a. The resistance decreases from an immeasurable 10^{18} Ω with 20 nm of glass between the tip and the bath. Upon breakthrough the resistance drops to the measurable $G\Omega$ regime. Details of the test circuit are described by White et al [23].
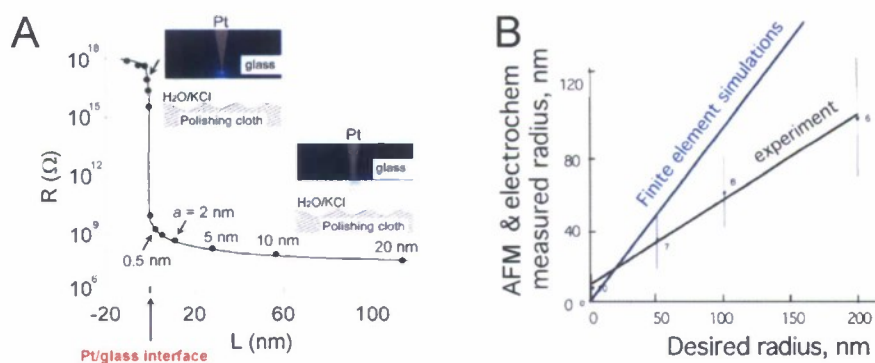
Figure 30. (A) Estimated resistance between Pt tip and polishing cloth electrolyte solution. The predicted nanopore radius is indicated at 0.5, 2, 5, 10 and 20 nm. (B) Comparison of predicted and actual nanopore radius.

The capillary is polished using the MOSFET circuit to create a Pt nanodisk electrode. The Pt is then electrochemically etched in $CaCl_2$ to remove as much of the Pt wire as possible from the glass. The remaining Pt can readily be removed from the glass at this point by gently twisting

the W wire attached to the Pt inside the capillary. Figure 31 shows cross-sectional optical images of the following: (A) Pt tip sealed in glass; (B) the polished Pt nanodisks electrode; (C) the glass nanopore membrane after the tip is removed; and (D) a schematic drawing of the glass nanopore membrane showing the dimensions.
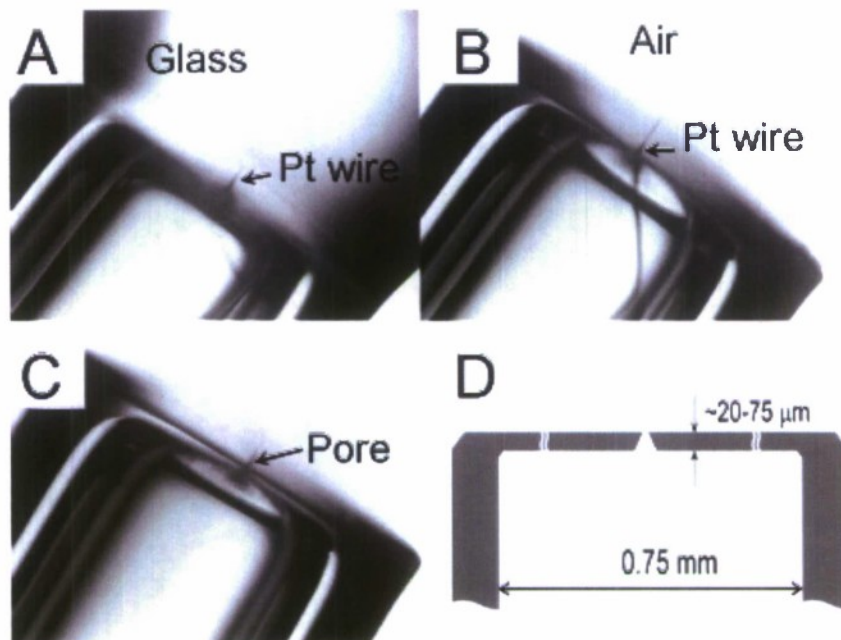
Figure 31. Optical images during the preparation of a glass nanopore membrane. (A) Pt sealed in bulk glass; (B) Pt sealed in glass membrane after polishing glass; (C) glass nanopore membrane after removal of Pt; (D) schematic of glass nanopore membrane showing nominal membrane dimensions. The small opening of the pore is not drawn to scale.

The radius of the small orifice of a glass nanopore membrane can be determined from the ionic resistance of the pore measured in a solution of known ionic conductivity. The pore resistance is obtained from the slope of i-V curves recorded by varying the potential between two Ag/AgCl electrodes positioned on opposite sides of the membrane. The relationship between the membrane resistance, R_p, and the small orifice radius, a_p, is given by

$$R_p = \frac{1}{\kappa a_p} \left(\frac{1}{\pi \tan \theta} + \frac{1}{4} \right)$$

where R_p is the resistance, κ is the conductivity of the solution, and θ is the half-cone angle of the sharpened Pt wire (~10°).

3.2.2.2.   Bilayers on the GNM

Because of favorable interactions of the polar head groups of the lipid molecules and the hydrophilic glass surface, a lipid bilayer can be readily deposited at the outer surface of the unmodified GNM membrane to yield a supported bilayer across the pore orifice [26]. See Figure 32a. The supported bilayer configuration, however, is not ideally suited for ion channel recordings because of the leakage of current through the thin water layer (~1 nm thick) that exists between the polar head groups of the lipids and the glass surface [26]. An additional

problem with the "supported" bilayer across a GNM is the inability to localize or corral ion channel to the region directly over the aperture.
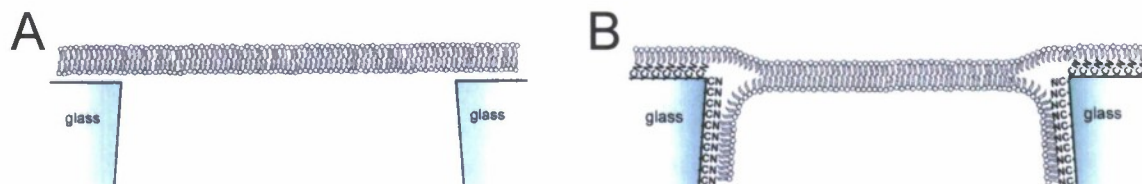
Figure 32. (A) "Supported" bilayer formed across hydrophilic glass surface and nanopore. (B) "Suspended" bilayer formed across modified hydrophobic glass surface and nanopore.

The solution is to make the surface of the GNM hydrophobic. We have discovered that deposition of 3-cyanopropyldimethylchlorosilane on the GNM surface, which creates a silane monolayer with a terminal -CN functionality, allows for both the formation of the suspended bilayer structure shown in Figure 32B and the wetting of the nanopore by aqueous solutions. In addition, the -CN functionality prevents protein adsorption on glass, as initially reported by Wayment and Harris. The GNM bilayer structure shown in Figure 32B exhibits typical seal resistances of >70 GΩ and can be formed over pore orifices ranging from tens of nanometers to several micrometers on glass and quartz.

The GNM is pretreated before silanization by soaking the entire glass capillary (inside and outside) in a 0.1 M HNO3 solution for 10 min. The glass capillary is rinsed with copious amounts of ultrapure H2O followed by CH3CN. The GNM is then filled and fully immersed in a 2% v/v solution of 3-cyanopropyldimethlychlorosilane in CH3CN for 12 h to ensure surface modification of both the internal and external surfaces. The capillary is rinsed sequentially with CH3CN, EtOH, and H2O followed by air drying.

The Texas A&M group (TAMU) verified the nature of the self assembled lipid bilayers and monolayers on untreated and treated glass respectively. To demonstrate this, we first compared the fluorescence level of a POPC (1-palmitoyl-2-oleoyl-sn-glycero-3-phosphocholine) film fused to a hydrophilic bare glass substrate and a cyano-terminated substrate. Each bilayer was doped with 0.1 mol % Texas Red DHPE for visualization purposes. Glass substrates were cleaned following standard procedures, yielding uniformly hydrophilic surfaces. Several clean glass substrates were then functionalized with 3-cyanopropyldimethylchlorosilane following the same procedures used to functionalized GNMs. Lipids were introduced to the substrates via the vesicle fusion method.

A POPC vesicle solution was incubated above a glass surface for 20 min, and then excess solution was rinsed away and replaced by 1.0 M KCl, 10 mM PBS buffer solution (pH 7.4). Following the rinsing step, the surface was gently scratched with a pair of metal tweezers. Following the scratching step, the sample was rinsed again to remove any lipid material that separated from the surface during scratching. The fluorescence images on the left side in Figure 33 are micrographs of lipid layers on the bare glass (upper image) and on the cyanoterminated glass (lower image). Line scans of fluorescence intensity that correspond to the red lines drawn on the images are presented to the right of the corresponding fluorescence images. Both line scans have similar background levels (corresponding to the dark regions in the scratched area), yet the hydrophilic bare glass substrate displays precisely twice the specific fluorescence as the silanized glass sample. The 50% decrease in fluorescence obtained from

the cyano-terminated glass substrate, relative to the lipid bilayer on bare glass, is consistent with the formation of a lipid monolayer.
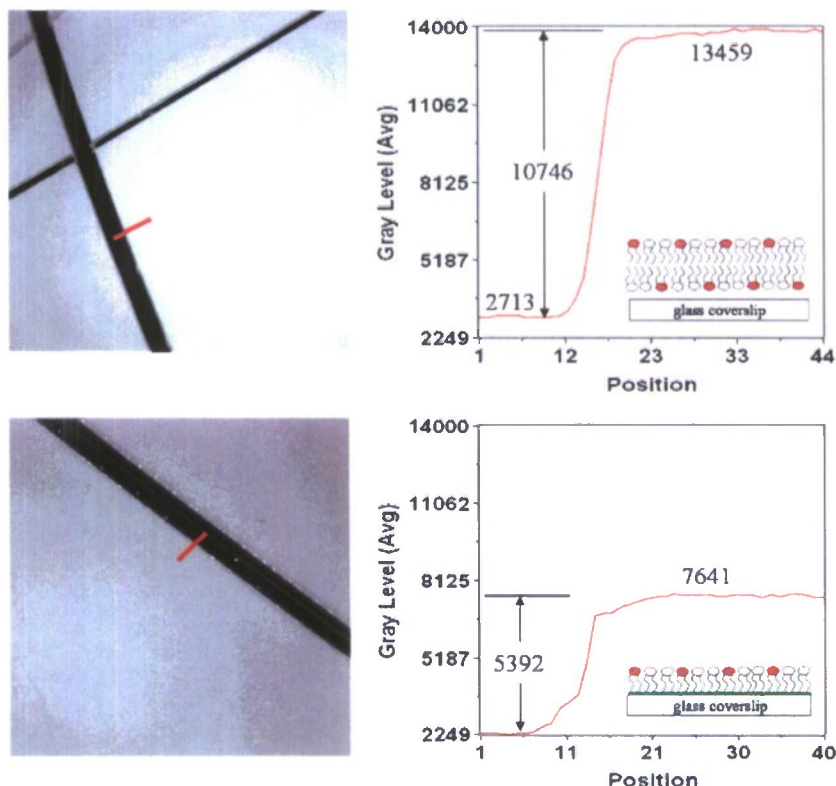
Figure 33. Fluorescence micrographs of a POPC lipid bilayer on bare (unmodified) glass (upper panel) and a lipid monolayer on silanized glass (lower panel). The linescan to the right of each image corresponds to the red lines in each image and shows the relative fluorescence levels of bilayer and monolayer with respect to the background. The scratch marks (black) were intentionally made with a tweezers to determine the background level.

3.2.2.3.   Ion channel measurements with the GNM

In the next step of the process, Utah developed methods to reliably incorporate αHL into the bilayer suspended across the GNM aperture. Consider the graphical representations shown in Figure 34. With a very small GNM aperture (50 nm in radius) the αHL protein still only occupies a very small fraction of the bilayer area, Figure 34A. If the protein is introduced from the capillary side (or backside) of the GNM, the insertion will happen in such a way that the trans side of the pore faces out of the GNM, Figure 34B. The hypothesis at this stage of the development was that the protein pore should readily incorporate into the bilayer.
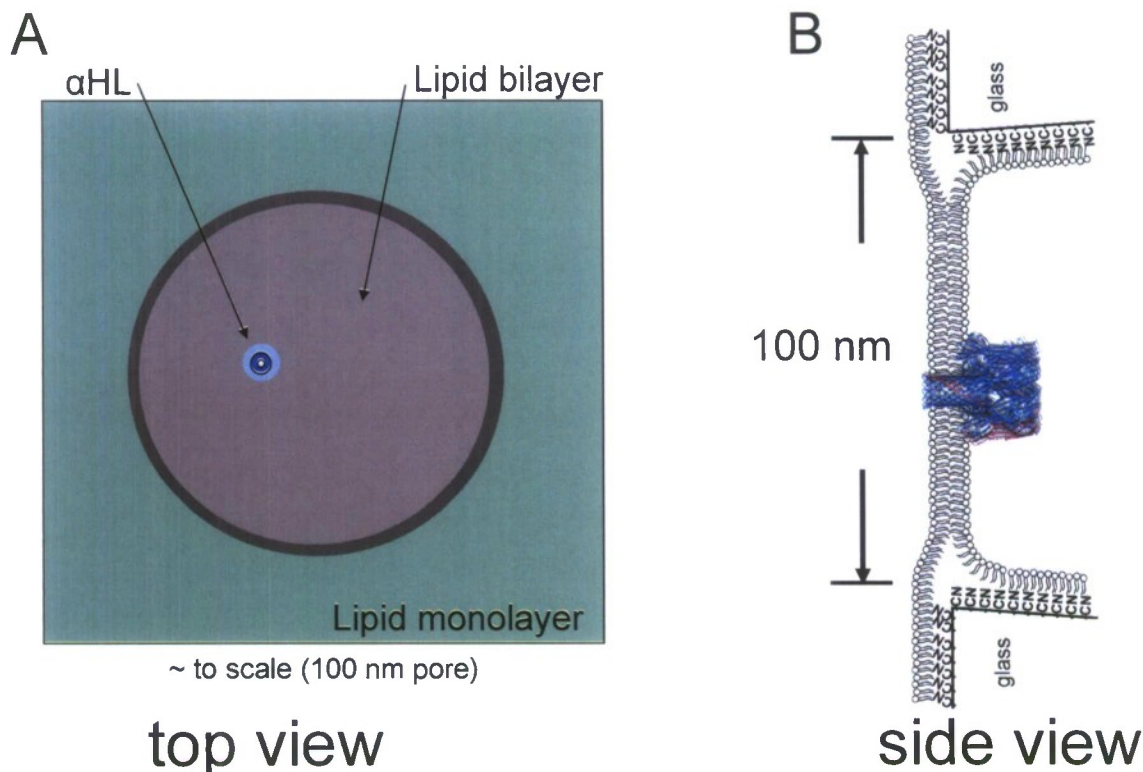
Figure 34. (A) Graphical top view of lipid bilayer, lipid monolayer and inserted αHL protein on a GNM face. (B) Side view of the suspended lipid bilayer across a nanopore with an αHL protein inserted from the backside of the GNM.

Preliminary measurements with the new suspended bilayer were inconsistent and the lifetime of the αHL in the bilayer was often very short. Some experiments with the newly modified GNMs showed signs of protein insertion into the bilayer, while others did not. Early on it was discovered that sealing the opposite end of the capillary significantly improved protein insertion. This then led to the use of backpressure to control the insertion and removal of αHL protein from the lipid bilayer.

A custom-built pressure rig (Figure 35A) was used to control and maintain a small positive transmembrane pressure, P_T, to quantitatively investigate the influence of P_T on αHL insertion rates. The experiment is performed by applying a positive or negative P_T (between -100 and 350 mmHg) inside the capillary relative to the external solution. Figure 35B shows a i-t plot of the pressure controlled insertion and removal of αHL. In this experiment, a DPhPC bilayer is painted across a 190 nm-radius GNM. The internal solution contained 3 μM αHL and a PBS buffer solution (pH 7.4), while the external solution contained only the PBS buffer (pH 7.4). To confirm protein insertion and removal, the ionic current was monitored while applying a constant voltage of -40 mV. In the initial stage of the experiment, and as long as $P_T = 0$, no channels insert in the bilayer. At t = 5 s, P_T is increased to ~100 mmHg, resulting in a single protein insertion at t = 7 s. A second channel inserts into the bilayer at t = 9 s. At t = 11 s, the pressure is reduced to -40 mmHg, resulting in the sudden removal of both channels. The suspended lipid bilayer membrane remains intact during the variations in P_T and the insertion/removal steps can be repeated indefinitely using the same bilayer. Figure 35B shows the insertion and removal of two additional channels in the time period between 15 and 25 s.
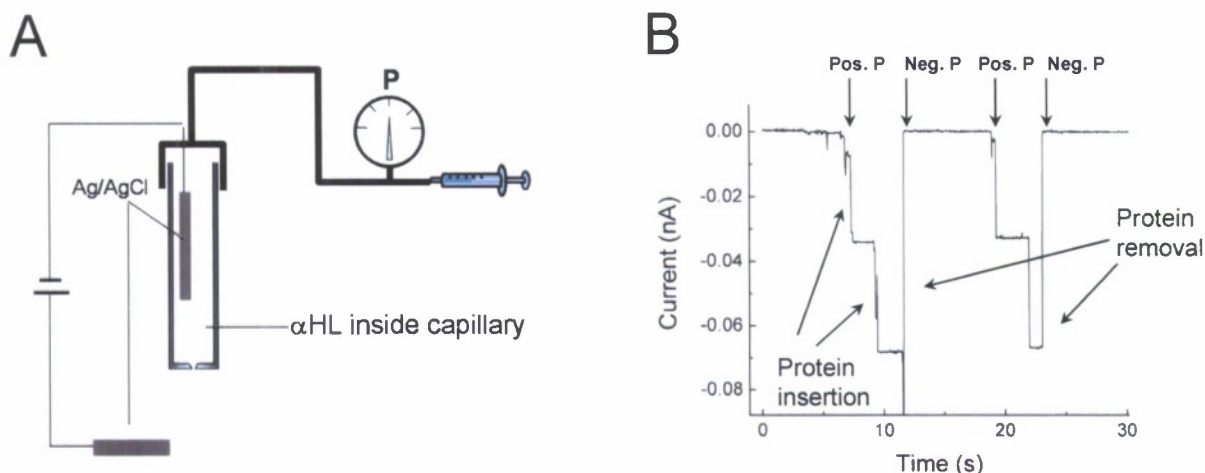
Figure 35. (A) Schematic of the pressure control apparatus used to control protein insertion into the lipid bilayer on a GNM. (B) An i-t trace showing the controlled insertion and removal of αHL channels as a function of the transmembrane pressure. In this example, a 100 mmHg transmembrane pressure is applied (inside capillary vs outside pressure) at t) 5 s, followed by spontaneous insertion of two αHL channels at ~7 and 9 s. The two channels are then removed by applying a -40 mmHg transmembrane pressure at ~11 s. A second controlled insertion and removal of two additional αHL channels is shown in the time period between 15 and 25 s.

Figure 36 shows a plot of the insertion rate of the first αHL channel into the DPhPC bilayers suspended across the orifices of three different GNMs with different radii (120, 190, and 250 nm). In these experiments, each GNM capillary was filled with a PBS buffer solution (pH 7.4) containing 1.5 μM αHL prior to formation of a DPhPC bilayer. After insertion of a single channel into the bilayer, a negative pressure was used to remove it, and the experiment was repeated. Inspection of Figure 36 demonstrates that the rate of insertion increases roughly linear with P_T. The slopes of the lines in Figure 36 also suggest that insertion rates scale roughly in proportional to the radius of the GNM orifice, or equivalently, the area of the lipid bilayer. In addition, the nonzero intercepts for all three lines clearly indicate that a threshold P_T of ~20 mmHg is required for insertion of a αHL channel into the GNM/bilayer structure. This latter finding is consistent with the observation discussed above that αHL channels do not insert into suspended bilayers on unsealed ($P_T = 0$) GNM.
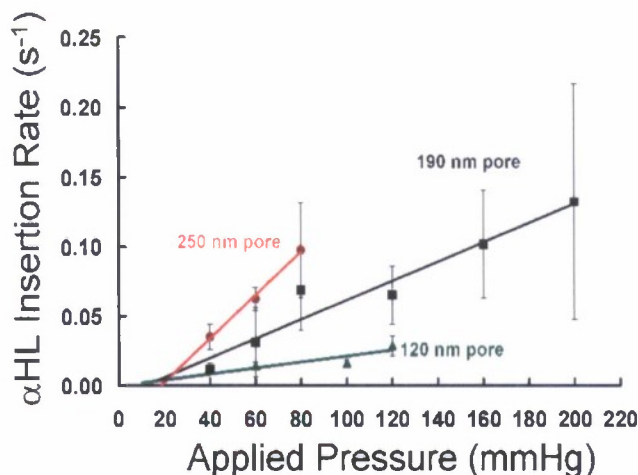
Figure 36. Plot of the rate of the first channel insertion as a function of transmembrane pressure for 250, 190, and 120 nm radius GNMs.

3.2.2.4.   Bilayer Robustness

Estimates of the stability of POPC and DPhPC bilayers suspended over GNMs were obtained by measuring the breakdown voltage, the susceptibility of failure from mechanical disruptions, and the lifetime of bilayers with and without αHL channels. As an initial qualitative measure of stability, we note that suspended bilayers on the GNM containing a functioning αHL channel can be manually transported between different solutions while maintaining electrical conductivity with a water droplet at the end of the glass capillary.

The electrical voltage stability of the suspended bilayer (without ion channel) was examined in PBS buffer solutions (pH 7.4). Bilayers were formed using the painting method [19] and then the potential was scanned at 50 mV/s while monitoring current. Using three GNMs (150, 150, and 100 nm-radius), an average breakdown voltage of 770 ± 150 mV was recorded, Figure 37. This voltage tolerance greatly exceeds the recently reported values of 325 mV [27] and 460 mV [28]. Along with improved voltage stability, bilayers suspended on the GNM are able to withstand rigorous stirring of solution without breakage.
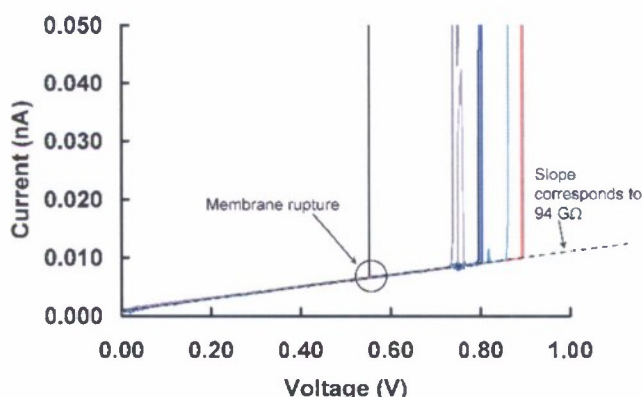
Figure 37. Electrical voltage stability of bilayers on GNMs. With a bilayer in place, the voltage is scanned at 50 mV/s. Failure of the bilayer is noted by a sudden increase in the measured current.

Bilayer lifetimes were measured in a sealed glass cell to avoid electrolyte evaporation. Bilayers were painted over several GNMs, and the seal resistance was monitored as a function of time.

Lifetimes of ~2 weeks were routinely achieved. Bilayers with αHL channels inserted from the inside of the capillary were also tested for lifetime stability with both continuous, Figure 38A, and periodic, Figure 38B, monitoring of the channel conductance. To date we have achieved a record for the continuous single ion channel recording (203 hours) of an ion channel in a lipid bilayer, as shown in Figure 38A. Blocking events are from sulfonated beta-cyclodextrin ($s_7\beta CD$). A single protein pore is maintained for ~3 days before additional insertions occur. On another system we achieved an approximately 400 hour lifetime with only periodic measurement of the ion channel current, Figure 38B. Each of these systems was operating in a laboratory with no special precautions for vibration isolation or environmental control. For comparison, a traditional, vibration isolated, laboratory setup for ion channel measurement will allow for continuous measurements of 10's of minutes to a few hours before the lipid bilayer fails.
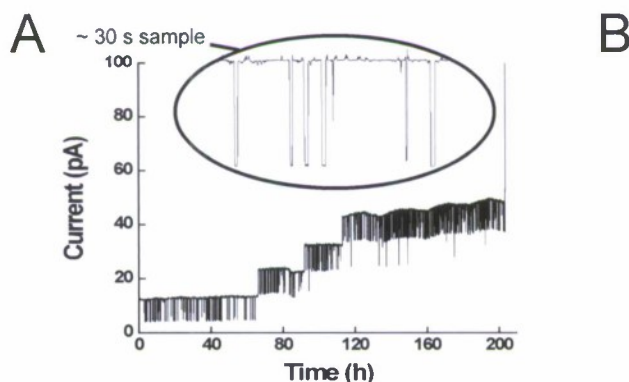
Figure 38. (A) Continuous 203 hour current measurement of ion channels in a suspended lipid bilayer, depicting beta cyclodextrin blocking events. A single channel (B) Current measurement through increasing numbers of ion channels for a lipid bilayer lasting ~400 hours.

3.2.2.5.   Development of a GNM Based Array

EBS has implemented a stochastic sensing array prototype based upon the GNM platform. Four glass nanopore membranes were set up in a custom built Telfon cell with the goal of demonstrating the feasibility of an array-based GNM system. A photograph of the EBS array-based demonstration system, including the Faraday cage, which contains 4 stopper boards (amplifiers), 4 GNMs and holders, and the single array-based Teflon cell is shown in Figure 39. For this system, lipid bilayers were simultaneously deposited onto each respective GNM, using the solution raise method (see Section 6.2.3). Initially, the electrolyte solution was below all of the GNMs. A small amount (< 1 μl) of 5 mg/ml DPhPC in decane was place on the surface of the electrolyte solution. The electrolyte solution surface was then raised up past each GNM, simultaneously depositing suspended lipid bilayers onto each GNM.

Figure 39. Top view of the EBS array demonstration system, which includes the Faraday cage, 4 stopper boards, 4 GNM and pressure control systems, and one array-based Teflon cell.

Once all four GNMs contained bilayers, αHL monomer (Sigma), was added to the Teflon cell to a final concentration of approximately 400 nM. Following the addition of αHL, the back pressure of each GNM was increased near its respective break pressure (determined prior to adding αHL), once αHL inserted, the back pressure of that GNM was decreased to near the pull out pressure. If the protein came out of the bilayer, the pressure was again raised to near its respective break pressure. This process was continued until all four GNMs contained one to a few αHL channels.

A close-up photograph, showing all 4 GNMs in the array, is shown in Figure 40. For this demonstration 1 M KCl, 10 mM PPB (pH 7.2) was used, and the analytes inside each GNM are as follows: GNM #1 (885 nm) contained 50 μM s$_7\beta$CD; GNM #2 (775 nm) contained 50 μM γCD (γ cyclodextrin); GNM #3 (315 nm) contained, 50 μM s$_7\beta$CD and 50 μM γCD; and GNM #4 (830 nm) contained no analyte molecule.
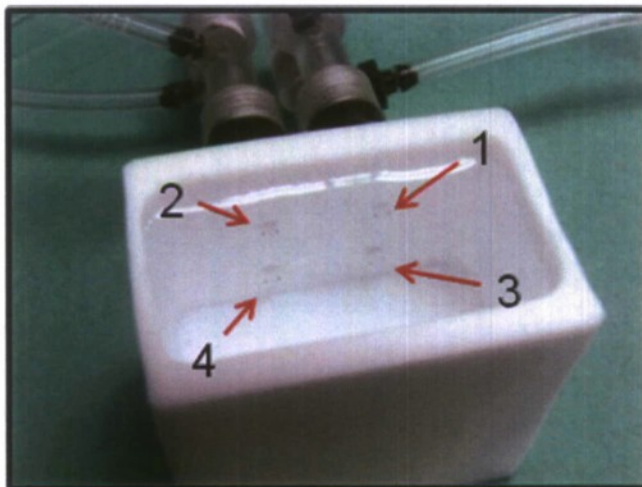
Figure 40. Photograph of the array-based Teflon cell, showing each GNM in the array.

A screen shot of the EBS LabVIEW array detection interface is shown in Figure 41. Here, the αHL channel in each respective GNM is detecting the internal analyte molecule, independently of one another. Channel four, is not detecting analyte, as there is no analyte within that GNM.
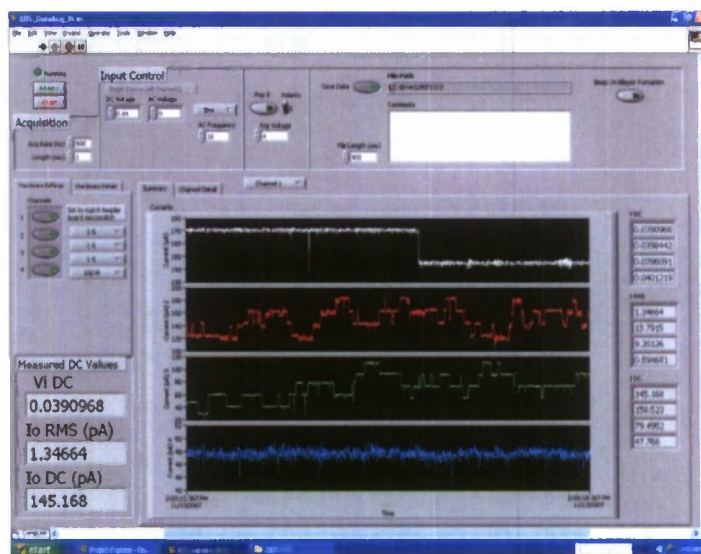
Figure 41   A screen shot of EBSs' array-based LabVIEW interface, depicting all four GNMs, containing αHL channels, and the associated analyte detection.

The results above, not only demonstrate the ability to transfer single GNMs into an array based system, but also demonstrate the ability to:

• simultaneously deposit bilayers onto an array, using the solution raise method.

• have independent ion channel control in an array, using pressure control.

• have a single cell, but separate electrical readout, in an array.

• have independent multi-analyte detection, using an array.

3.2.2.6.   Moving forward with the GNM platform

Following the initial evaluation of the GNM devices for use as a stochastic sensing platform, the GNM became the platform of choice for developing a prototype stochastic sensor. Although the bilayer lifetimes have not been shown to match those of the supported tBLM, the GNM platform has demonstrated the ability to make single channel measurements over extended periods of time. As will be shown later, the GNM platform has also proven to be readily incorporated into small test cells that employ semi-automated methods to form the suspended bilayer.

4. The Sensing Element - αHL

The central sensing element of the stochastic sensor is the αHL channel. The αHL channel is quite robust to modification of individual amino acids [29] while still maintaining the ability to produce channels through lipid bilayers. Over the course of the program, we have studied a variety of modifications to αHL to confer sensitivity to various types of chemical warfare agents. The modified sites are shown in Figure 42A. The modifications are made only to odd numbered residues as these are the residues that project into the interior of the β-barrel portion of the pore, Figure 42B.
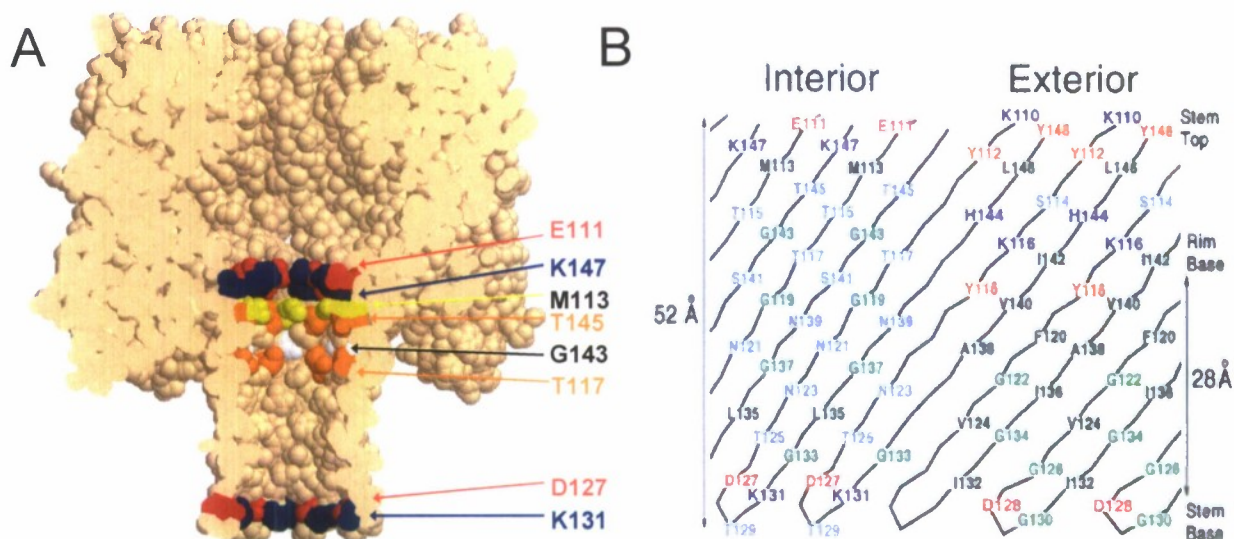
Figure 42. (A) Modification sites of the αHL protein pore. (B) Arrangement of amino acid residues in the interior and exterior of the β-barrel [30].

4.1. Detection of Mustard Agents

The University of Oxford group pursued the development of recombinant αHL proteins with the capability of detecting mustard agents. A number of separate strategies were developed whereby a reactive site was introduced into the lumen of the αHL pore [31]. An overview of the two primary strategies is shown in Figure 43 and a description of each is as follows

- Class I, reactions between mustards and single thiol groups inside the β-barrel of the αHL pore, provided by the side chains of cysteine residues
- Class II, reactions between mustards and multiple thiol groups inside the β-barrel of the αHL pore

All measurements were made with a traditional planar lipid bilayer setup as described by Braha et al [3].
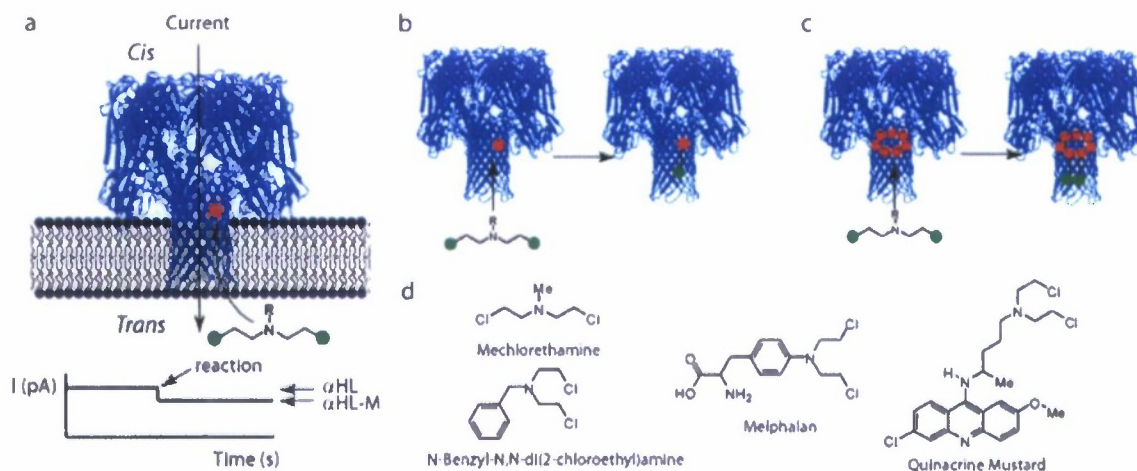
Figure 43. Primary strategies employed in the detection of mustard gas analogues with engineered αHL pores. Thiol groups are represented as red spots. Chemical structures in A-E are not to scale: (A) Illustration of the principle for the detection of mustards through covalent reaction with thiol groups within the lumen of αHL nanopores. After reaction, the mustard produces a reduction in current as illustrated (αHL-M). (B) Detection of mustards with an engineered αHL pore containing a single thiol group contributed by a cysteine residue (class I reaction). (C) Detection of mustards with an engineered αHL pore containing multiple thiol groups contributed by cysteine residues (class II reaction). (D) Chemical structures of mustard molecules used in the present study.

4.1.1. αHL Pore Containing a Single Thiol (Class I Reaction).

The chloroethyl group of mustards reacts with thiol groups under basic conditions at room temperature [32]. When a single pore, $(T117C)_1(WT)_6$, a cysteine residue at position 117 on one unit of the heptamer and wild type proteins for the other 6 units, was introduced into the lipid bilayer from the cis chamber, we measured an ionic current of 125 ± 10 pA (+100 mV, 20 mM CAPS, pH 10.5, 2 M NaCl; number of bilayers examined, n = 12). To observe a reaction with the pore, mustards in methanol solution were added into the trans chamber (final concentration, 50 μM) while the potential was held at +100 mV.

After a period ranging from 2 to 10 min, a current reduction was observed for all the four mustards tested (Figure 43F). In the case of the small molecule mechlorethamine, a current reduction of 3.0 ± 0.5 pA (n = 6) was observed at the reaction point and the current level became permanently locked into this lower conductance state (Figure 44A). No recovery of the current from the lower value to that of the unreacted pore was observed during a total recording period of 6 h (over six experiments).

Figure 44. Detection of mustards with an engineered αHL pore containing a single cysteine residue. (A) Single-channel current trace of $(T117C)_1(WT)_6$ with mechlorethamine (50 μM) in the trans chamber in 20 mM CAPS, pH 10.5, 2 M NaCl, at +100 mV. The reaction point is marked by an arrow and was at 3.0 min in this case. The mean time to reaction was 2.5 ± 0.5 min (n = 3). (B) Single-channel current trace of $(T117C-D8RL3)_1(WT)_6$ with N-benzyl-N,N-di(2-chloroethyl)amine (50 μM) in the trans chamber in 20 mM CAPS, pH 10.5, 2 M NaCl, at -100 mV. The reaction point is marked by an arrow and was at 10.0 min in this case. The mean time to reaction was 10 ± 3 min (n = 3). (C) Characteristic current trace at +100 mV of the $(T117C)_1(WT)_6$ pore after reaction with N-benzyl-N,N-di(2-chloroethyl)amine. (D) Characteristic current trace at -100 mV of the $(T117C)_1(WT)_6$ pore after reaction with N-benzyl-N,N-di(2-chloroethyl)amine.

In the case of the larger molecule melphalan, a larger current reduction (36 ± 4 pA, n = 3) was observed when the reaction occurred and the current again remained permanently at the reduced level. Interestingly, for N-benzyl-N,N-di(2-chloroethyl) amine and quinacrine mustard, after the reaction occurred, we observed characteristic substates at both positive and negative potentials (Figure 44B-D). These signals are presumably due to the movement of the mustards attached to the cysteine side chains inside the lumen of the αHL pore.

The disadvantage of the class I reaction is that there is only one reaction step and therefore detection might not be considered conclusive, especially if the reacted mustard does not provide a distinctive current signature.

4.1.2. αHL Pore Containing Multiple Thiols (Class II Reaction).

To observe multiple reactions of an analyte inside a single protein pore, and thereby ensure more secure detection, we made a homoheptameric αHL pore $(T117C)_7$ with cysteine residues at position 177 for all seven units of the heptameric protein pore. When a single $(T117C)_7$ pore was introduced into the lipid bilayer from the cis chamber, we measured an ionic current of 120 ± 8 pA (+100 mV, 20 mM CAPS, pH 10.5, 2M NaCl, n = 6). Mustards in methanol solution were added into the trans chamber (final concentration, 50 μM) and the potential was held at +100 mV. For N-benzyl-N,N-di(2-chloroethyl)amine, Figure 45A, the first reaction occurred within 10 min of the addition (8 ± 2 min, n = 3). A second reaction occurred 1.2 ± 0.3 min (n = 3) after the

first one, and 2.0 ± 0.5 min (n = 3) later a third reaction occurred. The recording was continued for another 30 min, and no more reaction steps were observed (n = 3). For mechlorethamine, the first reaction occurred 3.5 ± 1.0 min (n = 3) after addition. A second reaction occurred 1.5 ± 0.5 min (n = 3) later, and then at 1.9 ± 0.5 min a third reaction occurred. There was a relatively long time gap (15 ± 3 min, n = 3) before a fourth reaction was observed. After another long gap (18 ± 5 min, n = 3), a fifth reaction occurred (Figure 45B). The recordings were continued for another 35 min, and no further reactions were observed (n = 3).

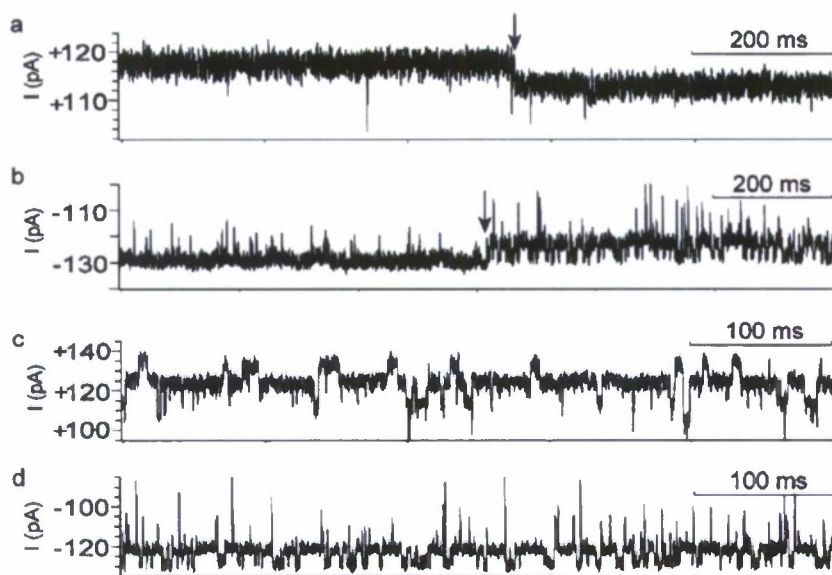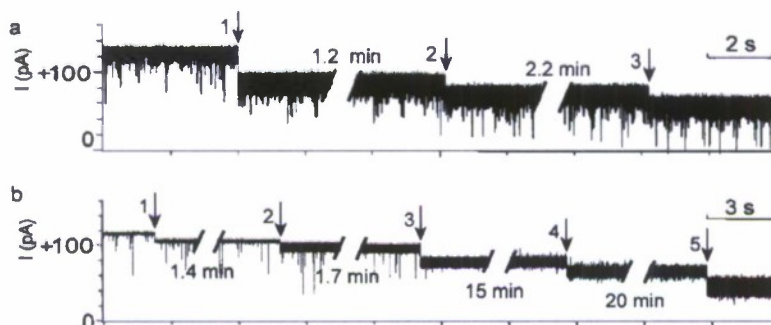Figure 45. Detection of mustards with an engineered αHL pore containing multiple cysteine residues. (A) Single-channel current trace of $(T117C)_7$ with N-benzyl-N,N-di(2-chloroethyl)amine (50 µM) in the trans chamber in 20 mM CAPS, pH 10.5, 2 M NaCl, at +100 mV. The reaction points are marked by arrows. (B) Single-channel current trace of $(T117C)_7$ with mechlorethamine (50 µM) in the trans chamber in 20 mM CAPS, pH 10.5, 2 M NaCl, at +100 mV. The reaction points are marked by arrows.

As with the Class I method, the binding of the mustard analog to the protein pore is not reversible. This limits the utility of the method as quantification of analyte will be difficult and there is not a characteristic signature to the binding events.

4.1.3. Discussion of Mustard Agent Detection Methods

In addition to the two methods described in detail above, two other methods were investigated for the detection of mustard agents [31]. Each of these methods suffered from the same drawbacks: relatively low sensitivity (i.e. detection of ~50 µM quantities in minutes, limited ability to quantify the concentration of analyte) and a poisoning of the sensor due to irreversible binding with the target analyte. The sensor did not recover functionality after exposure to mustard agents even after waiting periods in excess of 6 hours. The lack of sensor recovery is a serious limitation since it makes it difficult to distinguish between interaction with mustard agents and non-specific interaction of the cysteine residue with natural interferents. The goal of the program is to use the benefits of stochastic sensing where the blocking level and kinetics can be used to identify and quantify the target analytes. In light of these limitations, we made the decisions to move on to strategies where the analyte-pore binding is much more rapidly reversible.

4.2. Detection of Organophosphate Nerve Agents

The team at the University of Texas at Arlington (UTA) has focused on the detection of organophosphate based chemical warfare agents (nerve agents). Examples of the most common nerve agents are shown in Figure 46. The approach adopted by UTA was to introduce functional groups into the lumen of the αHL pore that would have preferential non-covalent bonding to small organophosphates. Due to the difficulty in obtaining nerve agents for testing,

the UTA group has restricted testing to various analogs including the hydrolysis products of the nerve agents.
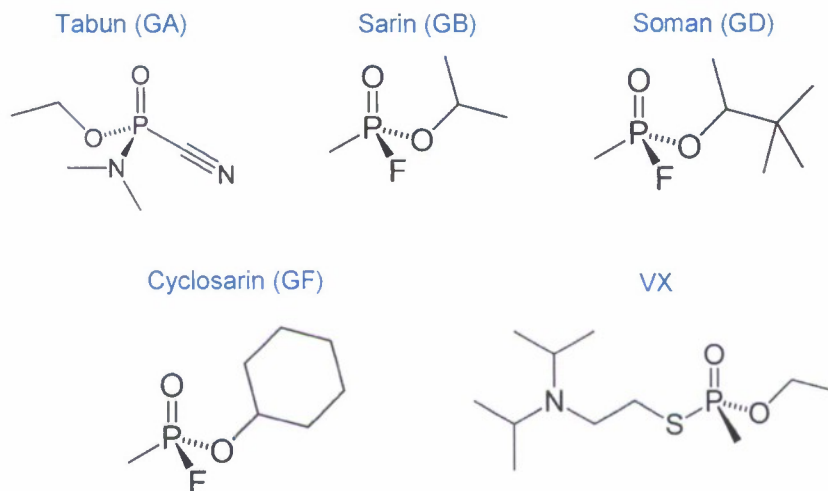
Figure 46. Common organophosphate chemical warfare agents and their associated structures.

4.2.1. UTA Test Apparatus

The apparatus consists of two fluid chambers (*cis* and *trans*) separated by a Teflon septum (25 μm thick; Goodfellow, Malvern, PA, USA).   An aperture (150 μm) in the septum is pretreated with 10% (v/v) hexadecane (Aldrich; Milwaukee, WI) in *n*-pentane (Burdick & Jackson; Muskegon, MI).   A bilayer of 10 mg/mL 1,2-diphytanoylphosphatidylcholine (Avanti Polar Lipids; Alabaster, AL, USA) in *n*-pentane is formed on the aperture.   The formation of the bilayer is achieved by using the Montal-Mueller (i.e., monolayer folding) method [18], and monitored by using a function generator (BK precision 4012A; Yorba Linda, CA, USA).   The experiments are performed under symmetrical buffer conditions with each compartment containing a 2.0 mL solution of 1 M NaCl and 10 mM Tris·HCl (pH 7.5) unless otherwise specified.   Unless otherwise noted, the αHL protein was added to the *cis* compartment, which was connected to "ground".   In such a way, after insertion of a single αHL channel, its mushroom cap is located in the *cis* compartment, while the β-barrel of the αHL is inserted into the lipid bilayer and connected with the *trans* chamber.   The final concentration of the αHL protein is typically 0.2–2.0 ng·mL^{-1}.   The transmembrane potential is applied with Ag/AgCl electrodes with 3% agarose bridges (Sigma) containing 3 M KCl (EMD Chemicals Inc; Darmstadt, Germany.   A negative potential indicates a lower potential in the *trans* chamber of the apparatus.   Currents are recorded with a patch clamp amplifier (Axopatch 200B, Molecular Devices; Sunnyvale, CA, USA), low-pass filtered with a built-in four-pole Bessel filter at 2 kHz and sampled at 10 kHz by a computer equipped with a Digidata 1440 A/D converter (Molecular Devices).   To shield against ambient electrical noise, a metal box is used to serve as a Faraday cage, inside which the bilayer recording amplifying headstage, stirring system, chamber, and chamber holder are enclosed.

4.2.2. Protein Expression

Mutant αHL genes were constructed by side-directed mutagenesis (Mutagenex, Piscataway, NJ) with a wild type (WT) αHL gene in a T7 vector (pT7–αHL) [33]. Briefly, mutant αHL monomers were first synthesized by coupled *in vitro* transcription and translation (IVTT) using

the *E. Coli* T7 S30 Extract System for Circular DNA from Promega (Madison, WI). Subsequently, they were assembled into homoheptamers by adding rabbit red cell membranes and incubating for 2 h. The heptamers were purified by SDS-polyacrylamide gel electrophoresis and stored in aliquots at -80 °C.

4.2.3. Detection of DTPMPA and TDP with M113K

The first nerve agents analog to be tested was Diethylenetriaminepentamethylenephosphonic acid heptasodium salt ($C_9H_{21}N_3O_{15}P_5Na_7$, DTPMPA). DTPMPA is a water soluble organophosphate with multiple phosphate groups. Thymidine 5"-diphosphate (TDP) was used as an interferent. Both compounds are shown in Figure 47.

DTMPA: Diethylene Triamine   TDP: Thymidine 5"-diphosphate
Penta (methylene phosphonic acid)
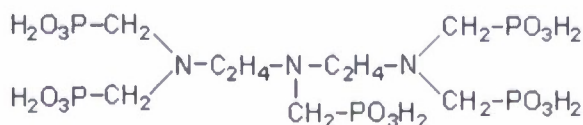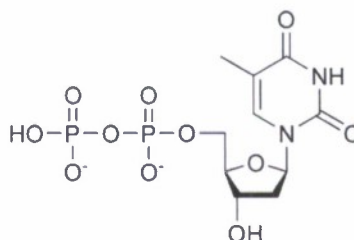
Figure 47. (Left) The DTPMPA molecule used as a nerve agent simulant. (Right) The TDP molecule used as a strong interferent to DTPMPA detection.

The UTA team tested a variety of αHL mutants for sensitivity to DTPMPA and TDP and found that the $(M113K)_7$ mutant (i.e. the methionine at residue 113 is replaced with lysine on each of the 7 units of the heptameric pore) was especially well suited to the task. When DTPMPA was added to *cis* chamber, clearly defined blocking events were observed, Figure 48A. As the concentration of the DTPMPA was increased the frequency of DTPMPA events increased proportionately as shown in Figure 48B. Very low concentration (~10 nM) of DTPMPA were readily detected. Although the αHL mutant $(M113R)_7$ was also shown to sense DTPMPA, the sensitivity was much lower than that of the $(M113K)_7$ pore. When $(M113R)_7$ was used, the event dwell time was about one-tenth of that observed when using $(M113K)_7$. In both cases, the relatively neutral methionine residue at the constriction of the pore was replaced by a positively charge residue, lysine (K) or Arginine (R), with an affinity for phosphate groups.
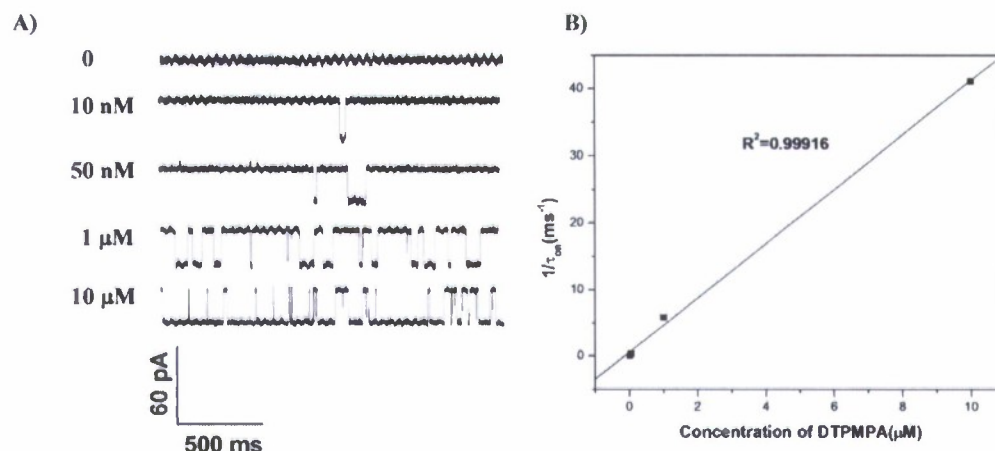
Figure 48. Stochastic detection of DTPMPA in the αHL mutant (M113K)$_7$ pore. A) Single-channel current recordings showing the interaction of a single (M113K)$_7$ pore with DTPMPA; B) Dose-response curve. The experiments were performed at +40 mV (*cis* at ground) in 1 M NaCl, 10mM Tris.HCl (pH 7.5). Both (M113K)$_7$ and DTPMPA were added in the *cis* side of the chamber.

As shown in Figure 49, detection of DTPMPA by (M113K)$_7$ is significantly affected by the relative orientation of the αHL pore. When adding DTPMPA to the *trans* side the events are very short and infrequent. By adding DTPMPA to the *cis* side, the blocking dwell time and frequency is dramatically increased. This asymmetry of the interaction demonstrates the complex nature of the interaction between the protein pore and the target analytes.
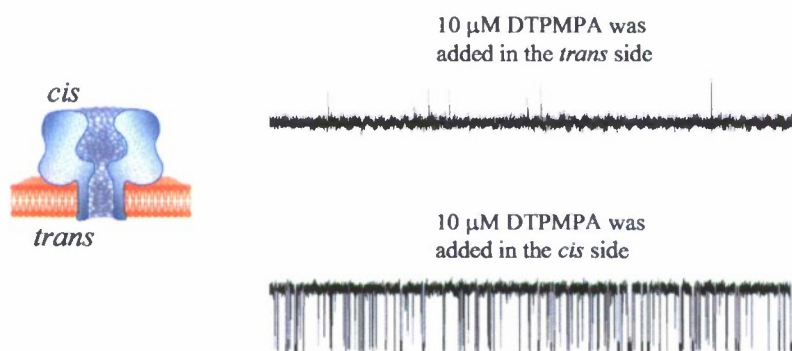
Figure 49. Adding DTPMPA to the *trans* side of (M113K)$_7$ (top) results in far lower sensitivity than adding DTPMPA to the *cis* side (bottom).

The UTA group characterized the effect of the bias potential on the dwell time and blocking amplitude of DTPMPA. A maximum in the blocking dwell time was observed at ~20 mV bias, Figure 50. The blocking amplitude increases approximately linearly with voltage and the fractional block ranges from ~70% to 90%. The longer dwell times near 20 mV have the potential to improve sensitivity, but this needs to be balanced against the increased event SNR provided at higher bias and the increase in event frequency at higher bias (not shown). The factors will be considered later when optimizing the detection sensitivity for the demonstration system.
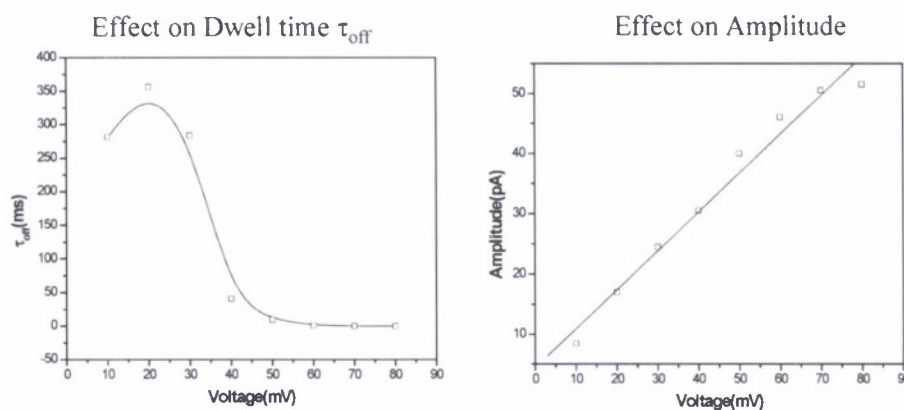
Figure 50. Voltage effect on DTPMPA detection. The experiments were performed at various applied voltages (*cis* at ground) in 1 M NaCl, 10mM Tris.HCl (pH 7.5). Both (M113K)$_7$ and 10 µM DTPMPA were added in the *cis* side of the chamber.

A series of tests were run to determine the ability to discriminate between DTPMPA and the interferent TDP. Both DTPMPA and TDP are organophosphates and expected to have an interaction with the (M113K)$_7$ channel. Single channel traces are shown in Figure 51. With 400 µM TDP and no DTPMPA, short and shallow blocking events are observed. Increasing the DTPMPA concentration results in a steady increase in the number of events per unit time attributable to DTPMPA blockades.
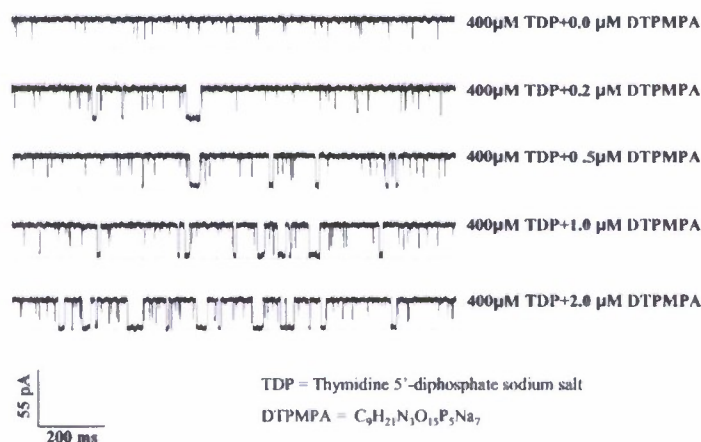
Figure 51. Single channel current recordings of mixtures of DTPMPA and TDP. The long deep blocks are directly attributable to DTPMPA.

Using methods described in Section 5, the University of Miami group (UMiami) performed an analysis of the stochastic sensing of DTPMPA in the presence of TDP. The resulting ROC curves are presented in Figure 52. The analysis assumes a detection time of 10 minutes and no other interferents than TDP. With a 400 µM concentration of TDP, the detection of 40 nM DTPMPA is effectively perfect. At 20 nM DTPMPA concentration the false alarm rate is less than 1 in 1 million at a 99.8% probability of detection.
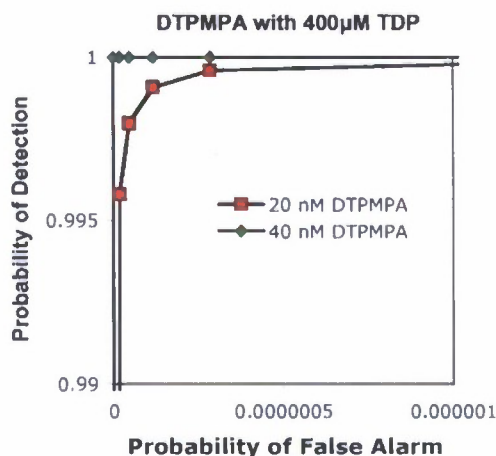
Figure 52. Receiver operating characteristic (ROC) curve for detection of DTPMPA in the presence of TDP. 20 nM DTPMPA (red) can be detected in the presence of 400 μM TDP (20,000: 1 ratio) 99.8% of the time with a false alarm rate less than 10^{-7}. 40 nM and higher DTPMPA (green) is indistinguishable from perfect detection at the level of computational accuracy available.

4.2.3.1.   Interferent Studies

The effect of three interferents on the detection of the organophosphate DTPMPA in the αHL pore (M113K)$_7$ was also investigated. In the first interferent test, Methyl Salicylate was added to the cis side of the apparatus at concentrations of 0, 1 μM, 10 μM and 100 μM. The single channel traces are shown in Figure 53A. Increasing the Methyl Salicylate concentration does not create any visible changes in the blocking events. A number of traces at each concentration were analyzed to determine mean time the channel is open (τ_{on}) and blocked (τ_{off}). The reciprocal of the open time ($1/\tau_{on}$) is proportional to the DTPMPA concentration and should also remain unaffected in order to properly quantify the DTPMPA concentration. The mean blocking time is used to discriminate between analytes and should not change in order to properly detect DTPMPA. As shown in Figure 53B and C neither $1/\tau_{on}$ or τ_{off} are affected by increasing the concentration of the tested interferent.
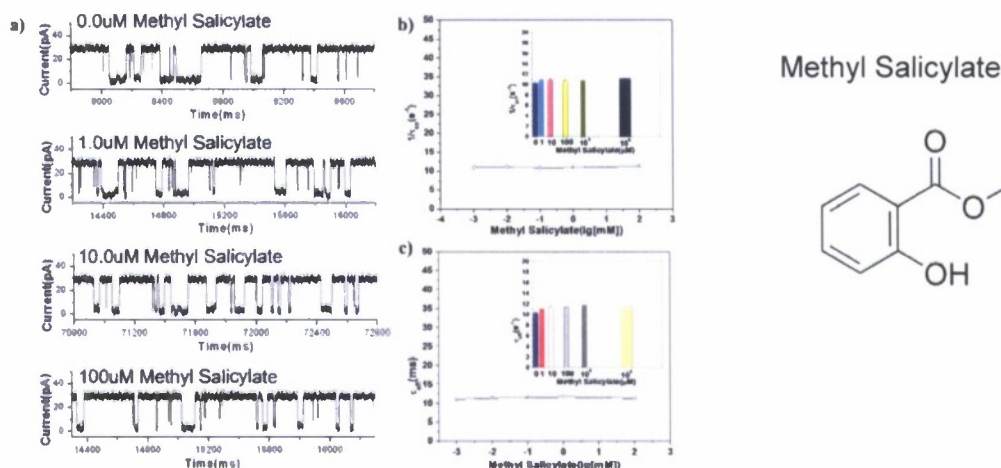
Figure 53. Effect of Methyl Salicylate on detection of 1 µM DTPMPA using the (M113K)$_7$ pore. (A) Single channel traces at increasing concentrations of Methyl Salicylate. (B) $1/\tau_{on}$ yields the frequency of DTPMPA events and is proportional to the DTPMPA concentration. (C) τ_{off} is the mean duration of DTPMPA blocks and is unaffected by the interferent.

Interferent tests were also run with Ethylene Glycol, a common component of radiator coolant. The effect of increasing Ethylene Glycol concentration (0, 1, 10, 100, 1000 µM) on the blocking of 1 µM DTPMPA is shown in Figure 54. As with Methyl Salicylate, Ethylene Glycol does not produce any noticeable interference with the detection and quantification of DTPMPA.
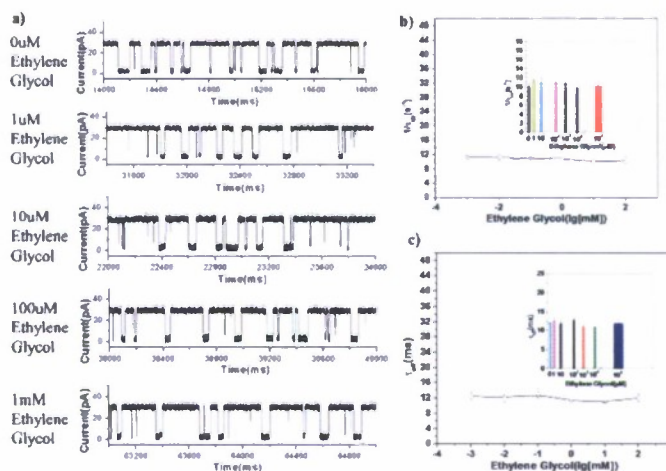
Figure 54. Effect of Ethylene Glycol on detection of 1 µM DTPMPA using the (M113K)$_7$ pore. (A) Single channel traces at increasing concentrations of Ethylene Glycol. (B) $1/\tau_{on}$ yields the frequency of DTPMPA events and is proportional to the DTPMPA concentration. (C) τ_{off} is the mean duration of DTPMPA blocks and is unaffected by the interferent.

Although the previous two tested interferents did not significantly affect the critical parameters of the DTPMPA signal, the introduction of Sodium Hypochlorite (NaClO) above ~100 ppm causes the DTPMPA events to be less frequent and farther apart in time. Increasing the NaClO

concentration above ~250 ppm stops all DTPMPA blocking activity. This leads to the possibility that it may be necessary to neutralize Cl_2 in heavily bleached water supplies.
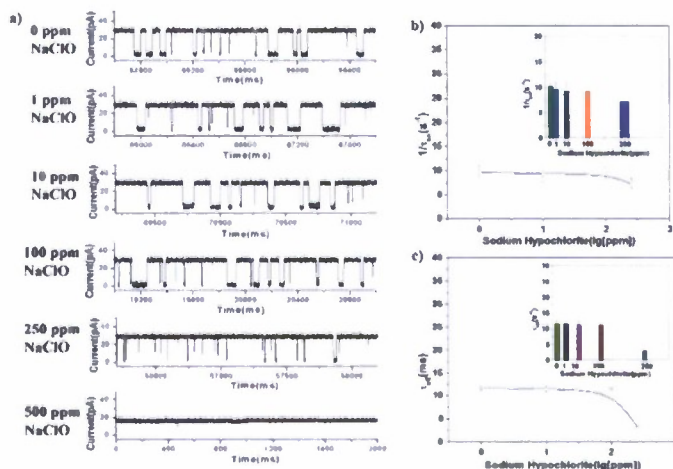
Figure 55. The presence of up to 100 ppm Sodium Hypochlorite (NaClO) containing 10-14% Cl_2 does not interfere with 1 μM DTPMPA detection. When the concentration of Sodium Hypochlorite exceeds 100 ppm, the frequency and duration of DTPMPA blocks decrease. Above 250 ppm, no activity is observed. a) Single-channel current traces; b) The event frequency ($1/\tau_{on}$); and c) dwell time (τ_{off}).

4.2.4. Detection of CWA Hydrolysis Products

Both DTPMPA and TDP share characteristics of organophosphate based chemical warfare agents, but neither is directly related to a specific CWA. Following the success with detection of DTPMPA and TDP at low concentrations, the MOLDICE team was directed to focus on developing the sensor element for the detection of live agents. Due to the difficulty in obtaining live agents for test and the poor solubility of live agents in aqueous solutions [32], we began to work with the readily obtained hydrolysis products of common CWA. Some examples of CWA hydrolysis products are shown in Figure 56.
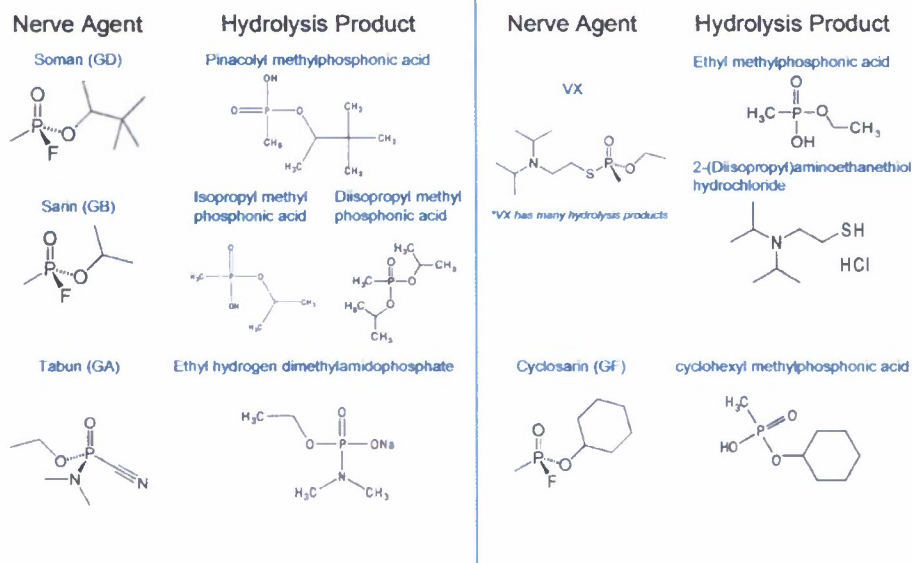
Figure 56. Common organophosphate nerve agents and their primary hydrolysis products.

4.2.4.1.   Nanopore sensing element for small organophosphates

At UTA, the engineered αHL (M113F/K147N)$_7$ pore, with βCD lodged in the lumen of the channel (as depicted in Figure 57A/B) as a molecular adapter, was employed as the stochastic sensing element for CWA hydrolysis products. Pinacolyl methyl phosphonic acid (PMPA) and cyclohexyl methyl phosphonic acid (CMPA), hydrolysis products of GD and GF [34], respectively, were employed as analytes. It is well established that βCD can be used as a host compound to capture and hence sense organic molecules [35]. When βCD is bound to the αHL pore, the channel is partially blocked and the open channel current drops. When a guest molecule is captured by βCD, and the resultant host-guest complex is bound to the pore, the channel is blocked to a larger extent with a further decrease in the observed current [5].
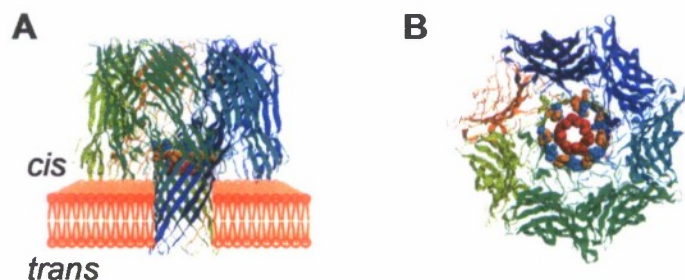
Figure 57. Molecular graphics representation of the staphylococcal αHL protein with βCD lodged in the lumen of the channel. (A) Side view of the (M113F/K147N)$_7$ pore; and (B) View into the (M113F/K147N)$_7$ pore from the *cis* side of the lipid bilayer, highlighting positions 113 (orange) and 147 (cyan), where the naturally occurring Met and Lys residues have been substituted with Phe and Asn, respectively, while the red color represents the βCD molecule.

Our experiments showed that in 1 M NaCl solution, βCD binds to the mutant (M113F/K147N)$_7$ protein very tightly, with a mean dwell time of 1.2 ± 0.1 s at an applied -80 mV potential. With βCD's binding to the pore, the channel current dropped from 58.8 ± 3.2 pA to 9.9 ± 1.2 pA (n = 10). If PMPA or CMPA was additionally added to the mutant (M113F/K147N)$_7$ αHL pore, the blocking event by the βCD·PMPA or βCD·CMPA complex further reduced the current to 0.08 ± 0.06 pA (n=5), or 0.31 ± 0.09 pA (n=5), respectively Figure 58. The association rate constants (k_{on}) of βCD·PMPA and βCD·CMPA were $6.5 \pm 0.7 \times 10^6$ $M^{-1}\cdot S^{-1}$ (n=3), and $2.5 \pm 0.3 \times 10^6$ $M^{-1}\cdot S^{-1}$ (n=3), respectively, while the dissociation rate constants (k_{off}) were $1.2 \pm 0.1 \times 10^3$ S^{-1} (n=3), and $1.6 \pm 0.2 \times 10^3$ S^{-1} (n=3), respectively. Thus, the overall reaction formation constants (K_f) at 23 $^{\circ}$C for βCD·PMPA and βCD·CMPA were $5.4 \pm 0.5 \times 10^3$ M^{-1} and $1.5 \pm 0.3 \times 10^3$ M^{-1} (n=3), respectively. This suggests that PMPA has a stronger binding affinity to βCD than does CMPA.
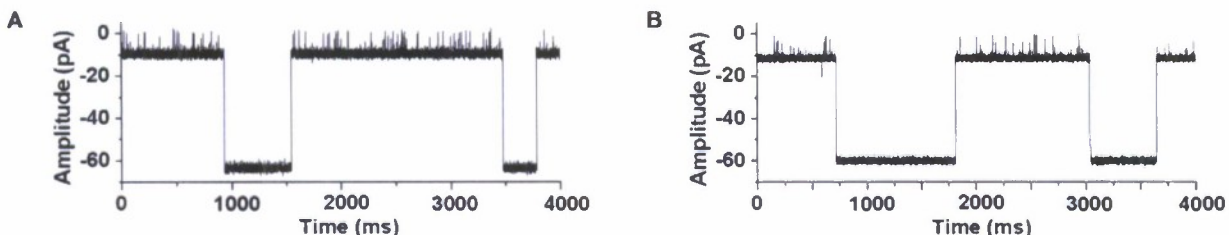
Figure 58.   Typical single channel current recording traces, showing the detection of PMPA and CMPA. (A) 2 µM PMPA; and (B) 2 µM CMPA.   The experiments were performed at -80 mV in 1 M NaCl and 10 mM Tris·HCl (pH 7.5), and in the presence of 40 µM βCD.

It should be noted that other engineered αHL pores, including (M113F/G145F/K147N)$_7$ and (M113F/T143F/G145F/K147N)$_7$ were also examined with βCD and PMPA/CMPA.   These two nerve agent hydrolytes produced similar current blockage events to those observed in the (M113F/K147N)$_7$ pore, although βCD showed much weaker bindings toward both the pores (data not shown).   The purpose of the pore mutation is to hold in the βCD host molecule as opposed to modify the host-guest interaction between the βCD and the target analyte.

4.2.4.2.   **Effect of voltage on sensor resolution**

PMPA events showed much shorter binding times (τ_{off}), indicating much weaker host-guest interactions occurred in the protein pore at positively applied potentials than at negatively applied voltages.   Hence, the voltage effect on the detection of 10 µM PMPA was investigated using the (M113F/K147N)$_7$ pore and in the presence of 40 µM βCD with an applied potential ranging from –40 mV to –120 mV.   With an increase in the applied voltage, both the dwell time and frequency of the host molecule βCD events decreased, while the amplitude of the analyte PMPA events increased.   As shown in Figure 59, with the increase of the applied voltage from -40 to -120 mV, the dwell time (τ_{off}) of the host molecule βCD decreased from 5.03 ± 0.13 s to 0.78 ± 0.24 s, the βCD event frequency ($1/\tau_{on}$) decreased from 4.38 ± 0.04 s^{-1} to 0.27 ± 0.05 s^{-1}, while the amplitude of PMPA events increased from 3.74 ± 0.30 pA to 16.01 ± 0.27 pA.   For the sensitive detection of PMPA, a large mean amplitude of PMPA events as well as large event dwell time and high frequency for the host molecule βCD were desired.   Based on these results a compromise bias of -80 mV was chosen.   At this bias the βCD last ~1s, occur frequently and the amplitude of the PMPA events is well above the noise floor of the measurement.
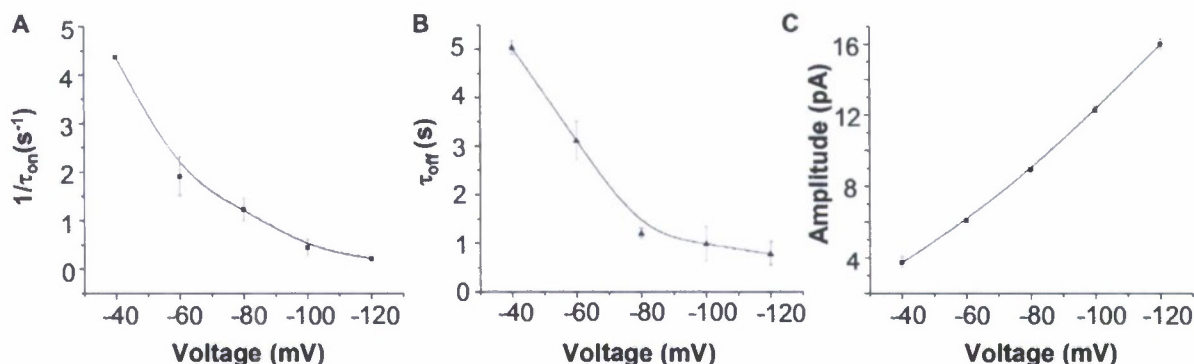
Figure 59. The effect of applied potential on (A) $1/\tau_{on}$ and (B) τ_{off} of the βCD events, and the (C) amplitude of PMPA events. The experiments were performed in1 M NaCl and 10 mM Tris·HCl (pH 7.5) and averaged over at least 3 trials. Both βCD and PMPA were added to the *trans*, while the mutant αHL protein (M113K/F147N)$_7$ was added to the *cis* compartment. The concentration of βCD was 40 µM, and that of PMPA was 10 µM.

4.2.4.3.   Characteristics of the nanopore stochastic sensor

The effect of the concentration of PMPA and CMPA on the event frequency ($1/\tau_{on}$), dwell time (τ_{off}), and amplitude was investigated. Our experiments (Figure 60A and B) showed that the event mean dwell time and amplitude were unvaried with the increase of the concentration of added PMPA (ranging from 500 nM to 10 µM) and CMPA (ranging from 500 nM to 8 µM). Therefore, amplitude and dwell time can be used as signatures for identifying different organophosphates, specifically, PMPA and CMPA. The experimental results also demonstrated that the event frequency ($1/\tau_{on}$) was linearly related to the concentration of PMPA and CMPA (Figure 60C), which provides a basis for quantifying these analytes. The sensitivities of the method for the detection of PMPA and CMPA were 4.47 µM·S^{-1} and 2.31 µM·S^{-1}, respectively. The detection limits for PMPA and CMPA were 53 nM (i.e., 0.01 mg/L) and 102 nM (i.e., 0.02 mg/L), respectively. The detection limit was defined as the concentration corresponding to three times the standard deviation of a blank signal. These values are significantly lower than the discharge limits required by US Army (0.1% in w/v, i.e., 1000 mg/L) [36]. It should be noted that, to obtain such detection limits, a 10 min recording time is required to collect 300 to 500 events depending on whether the analyte is PMPA or CMPA, from which low error mean values of the analyte signatures (e.g., τ_{off}, τ_{on}, and amplitude) can be obtained.
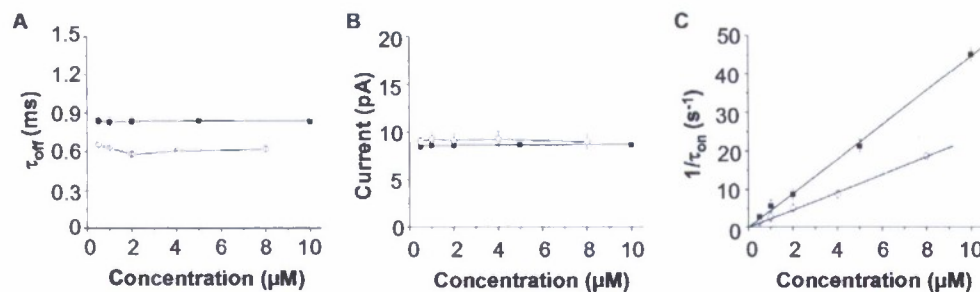
Figure 60. Effect of analyte concentration on current blocking events. (■) PMPA; and (○) CMPA. (A) Plot of τ_{off} as a function of PMPA/CMPA concentration, showing the mean dwell time of events was unchanged with the increasing concentration of added organophosphate, (B) Plot of amplitude as a function of PMPA/CMPA concentration, indicating the mean amplitude was unvaried with the changing concentration, where the amplitude was defined as the extent of current blockage, and (C) Plot of $1/\tau_{on}$ as a function of PMPA/CMPA concentration, demonstrating that the event frequency was linearly related to the concentration of added PMPA/CMPA. The experiments were performed at –80 mV in 1 M NaCl and 10 mM Tris·HCl (pH 7.5) and were averaged over at least 3 trials.

4.2.4.4.   Nanopore selectivity

Sarin hydrolysis products (i.e., isopropyl methylphosphonic acid, and diisopropyl methylphosphonic acid), VX hydrolysis products (i.e., 2-(diethylamino) ethanethiol, 2-(dimethylamino) ethanethiol, 2-(diisopropylamino)-ethanethiol, ethyl methylphosphonic acid, methyl phosphonic acid), tabun hydrolyte (i.e., ethyl hydrogen dimethylamidophosphate), and some common toxic organophosphates including diazinon, parathion, malathion and amifostine were also tested with the nanopore sensor. However, no current blockage events were observed when the concentrations of these analytes were lower than 500 µM, suggesting that the unmodified βCD approach is very selective toward PMPA and CMPA. It is likely that the interactions between these compounds and βCD are much weaker than those between βCD and PMPA/CMPA so that they could not be captured by βCD for sufficient time to produce observable events in our single-channel recording experiments (note that the instrument resolution is about 100 µs).

In general, βCD-based host-guest systems are not specific. A number of organic molecules with proper size will be captured by βCD and produce current blockage events, including, e.g., ibuprofen and thalidomide [37]. However, since different compounds produce different signatures (e.g., dwell time and/or amplitude) in the protein nanopore, PMPA and CMPA could be differentiated against common chemicals. For example, the dwell time of thalidomide was ~0.2 ms [37], while those of PMPA and CMPA were 0.83 ms, and 0.62 ms, respectively. Therefore, our method offers the potential for rapid screening of PMPA and CMPA. To further improve the selectivity and resolution of the nanopore sensor, development of other engineered αHL pores and utilization of more specific (non-βCD) approaches to the detection of nerve agent hydrolytes are now in progress.

4.3. Next Steps

Under the current program we have developed αHL sensing elements for mustard agents and organophosphate nerve agents. In each, nano to mico-molar sensitivity has been demonstrated for available simulant materials. With each of these systems, the next step is to demonstrate

high sensitivity detection of live agents. In addition, new sensing elements will be developed to improve the level of detection for CWA.

5. Signal Processing for Stochastic Sensing

As described in Section 2, stochastic sensing relies upon the reproducible blocking level of the analyte and the kinetics of the blocking to discriminate, identify, and quantify target analytes. The process breaks down to identifying binding events, analyzing the kinetics of the events, determining the optimal model to fit the kinetics, and reporting the sample composition and concentrations. The University of Miami team (UMiami) implemented an automated version of this analysis to detect and quantify the presence of target analytes in the stochastic sensing system.

5.1. Identifying Events

As shown in Section 2, the stochastic sensor detects the interaction of the target analyte with the pore based upon a discrete reduction in the measured current across the nanopore. For a given analyte, these events will have a characteristic blocking level(s). A variety of methods have been developed to automatically identify the presence of binding events including the half amplitude method [38] and the segmental k-means method [39]. The UMiami group has implemented a thresholding algorithm based upon an automated analysis of the single channel amplitudes histograms.

An example of the event detection results is shown in Figure 61. The measured current amplitudes of the single channel data (shown in green) are binned into a histogram (shown in blue to the right) that is used to determine the thresholding level. The threshold level is seen as a thin horizontal black line at ~60% of the maximum current level. The threshold is set based upon ½ the amplitude of the first peak in the edge of the peak in the distribution associated with the open channel (in this case the upper current limit). Based upon this amplitude, the algorithm determines the points in time when the amplitude drops below the threshold level. Values below the threshold level are clustered into contiguous blocked channel events. Values above the threshold are clustered into sections of open intervals. These events are represented by a thin black overlay of the current data. The main data window (contains 9 rows of ~66 ms single channel traces) contains approximately 600 ms of single channel data. The inset is a magnification of a selected region of data.
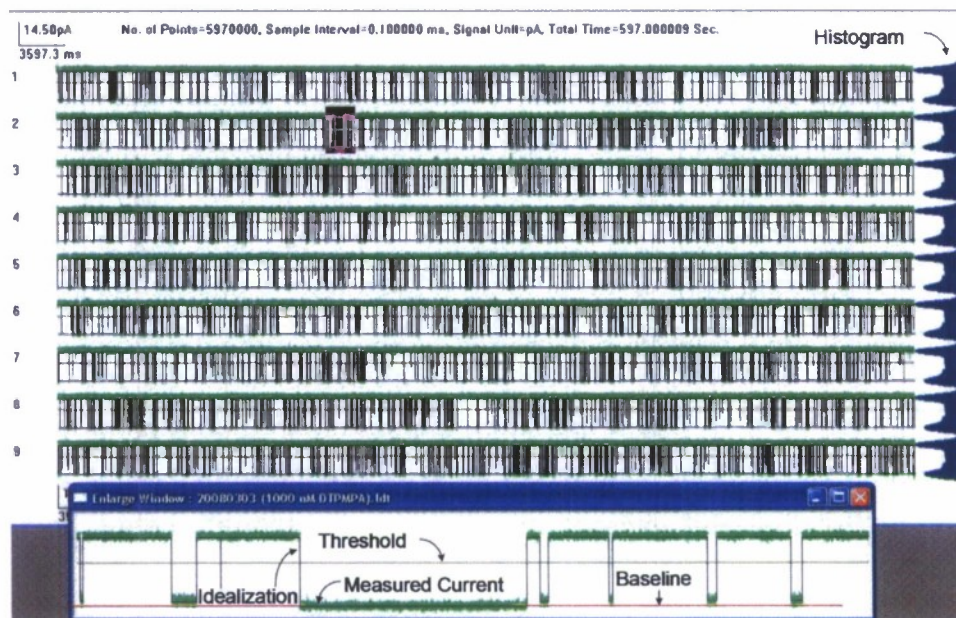
Figure 61. Example of event detection for 1 µM DTPMPA in 1M KCl. The main screen shows ~600 ms of data with the raw single channel current in green and the idealized data (detected events) overlayed in black. The histogram of all measured current values is shown in blue to the right. The inset shows an magnified view of data selected in the second trace.

UMiami also investigated the more advanced segmental k-means (SKM) algorithm for event identification [39], but no improvement in performance was noted for the high SNR data acquired during the program. The disadvantage of SKM is the ~10X increase in the computation time. For lower contrast blocking events, it may be necessary to adopt the SKM method, but under the current program this was not necessary.

5.2. Kinetics of Binding Events

With the events identified it is now possible to determine the kinetics of the binding events. The kinetics are particularly important in that the duration of the events identify the analyte and the frequency of the events determine the concentration of the analyte.

Event durations are binned according to the logarithms of their durations with

$$\text{bin} = 1 + \text{integer } (R \times \log_{10}(\text{duration of interval in sample periods}))$$

where R is the resolution factor which sets the number of bins per log unit [40]. Log binning allows events of any observed duration to be binned in a few hundred bins with negligible error if the resolution is 25 bins or greater per log unit. Even larger bins can be used without error if a correction for bin width is applied during the fitting. More details of binning and plotting of event duration histograms is provided by McManus et al [40].

Histograms of the events are then fitted with sums of exponential components using the method of maximum likelihood [41], as applied to binned and sampled data [40]. Each distribution was fitted with

$$f(t) = \sum_{j=1}^{k} a_j \tau_j^{-1} \exp\left(-t/\tau_j\right)$$

where $f(t)$ is the event duration histogram, k is the number of exponential components, and τ_j and a_j, are the time constant and area, respectively, of component j. The durations of all intervals greater than twice the dead time were fitted by maximizing the likelihood of the parameters (areas and time constants) describing the exponential components. Intervals less than two times the dead time were excluded to prevent detection of possible 'phantom' exponentials which can occur when data are filtered, and because durations of filtered intervals less than two dead times are underestimated with 50% detection [41] and correction of such durations is complicated by the noise in the experimental record [40].

Fits to each distribution of interval durations were made with increasing numbers of summed exponential components. The fits were then compared with the likelihood ratio test in order to determine the maximum number of significant exponential components in each distribution. Comparing fits with different numbers of exponential components corresponds to comparing nested models, allowing use of the likelihood ratio test [42]. Fits with different numbers of exponentials were compared by determining $\ln R_k$ from

$$\ln R_k = \ln L - \ln L_{k-1}$$

where $\ln R_k$ is the natural logarithm of the likelihood ratio for k versus k-1 exponential components, and L_k and L_{k-l} are the maximum likelihoods that the data were drawn from a distribution described by the sum of k and k-1 exponential components. Twice the value of $\ln R_k$ is distributed as χ^2, with the degrees of freedom equal to the difference in the number of free parameters when fitting with k and k -1 exponential components. An additional exponential component was judged significant (p < 0 05) when the value of $\ln R_k$ was ~2.96, one half the χ^2 value for two degrees of freedom at the 0 05 level. This provides an automated method to identify the number of components in the event duration distribution. An example of the results from the automated fit are shown in Figure 62.
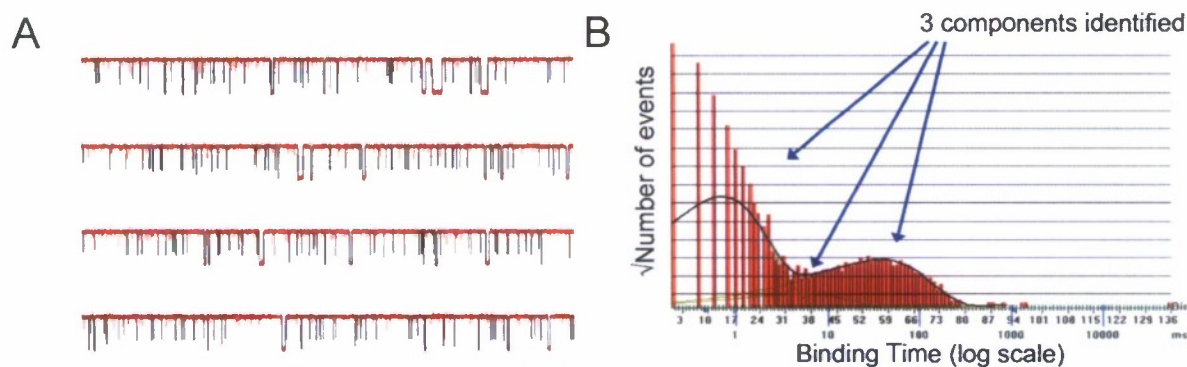
Figure 62. (A) Single channel current records of a DTPMPA and TDP mixture. (B) Event duration histogram derived from the single channel data.

5.3. Identification and Quantification

In order to determine the presence of an analyte it is necessary to know the expected binding time constant for that sample. With the known time constant, it is possible to determine how

well each fitted component matches to the target analyte. The normalized fitted distribution for $\tau_j^{-1}\exp\left(-t/\tau_j\right)$ for each component is compared to the expected distribution $\tau_m^{-1}\exp\left(-t/\tau_m\right)$ for each of the target analytes, m. If the correlation between the two distributions exceeds a set threshold, the jth component is identified as the mth analyte.

To determine the concentration of the analyte, it is necessary to know the event frequency as a function of the analyte concentration. Calibration curves such as those shown in Figure 63 are produced using known samples of the target analytes. With a known event frequency versus concentration it is then possible to convert the measured component areas a_j into analyte concentration.
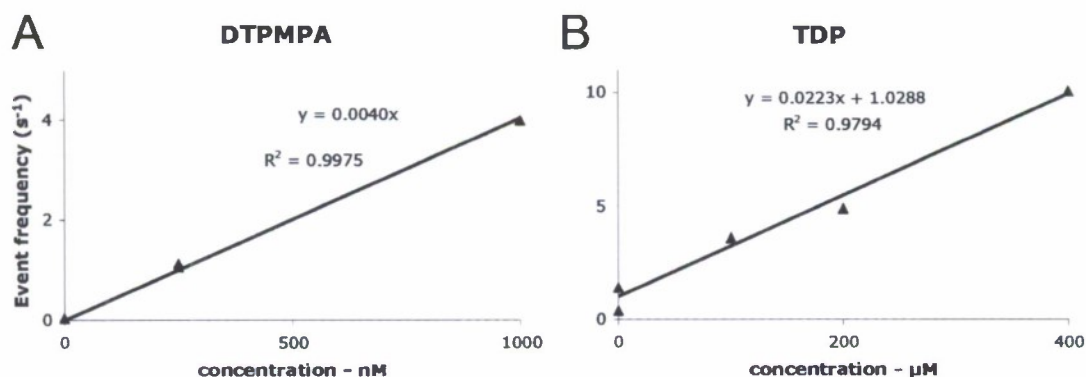
Figure 63. Event frequency for as a function of analyte concentrations for (A) DTPMPA and (B) TDP. The slope of the lines are used to calibrate the concentration output for the stochastic sensing automated analysis.

5.4. Integrated Analysis Package

UMiami integrated the previously described signal processing components to analyze stochastic sensor data into a single automated software application. The software application reads in the single channel data, performs an idealization to identify stochastic binding events, performs an analysis of the event duration statistics, estimates the presence and concentration of target analytes and displays a time history of the results. This application brings together the key signal processing developments developed under the current program.

The graphical user interface for the analysis package as configured for the system demonstration is shown at the top of Figure 64. The operation proceeds as follows. The user enters setup information via the setup function in the lower right corner. Details of the setup interface are shown at the bottom of Figure 64.

For each of the compounds to be detected, the user enters the compound name, the time constant of the blocking events(ms), the expected standard deviation of the binding time constant, the forward rate constant (Hz per µM) at a known concentration (nM), and the units to display. Examples are shown for DTPMPA and TDP. All of the parameters are determined from calibration experiments performed on known samples. The binding time constant is determined as shown in 5.2 based upon an exponential fitting to the binding time distribution. The forward rate constant is determined from the slope of the event frequency versus analyte concentration as shown in Figure 63. The user can enter any number of target analytes.

Figure 64. Automated analysis package for analysis of stochastic sensor data. (Top) Primary graphical interface and data display. (Bottom) Principal adjustable parameters accessed through the setup function.

In the setup window the user also enters information on how the data is to be displayed in the interface. The analysis will be performed on a predetermined number of samples (Categories) with a set number of repetitions per sample (Number of Runs) as defined by the user. Presently only the results from the first two compounds is displayed.

The left half of the interface displays results from the last sample analyzed. The top left "Raw Data" figure shows the raw current vs time traces with an overlay of the idealized events. Immediately to the right, the current amplitude distributions are displayed. The Blocking (or Binding) Time Distribution and the model fits are shown below. Adjacent to the standard binding time distribution is a plot of the joint probability distribution for event amplitude and duration. This distribution may later be used to provide a higher level of discrimination between analytes. Below this, a schematic of the optimal kinetic model is shown with forward and reverse rate constants. At the bottom left, the numerical results for each of the detected components in the current sample are shown. The area is proportional to the number of events per second and is converted into both the forward rate constant K based on the duration of the measurement (3 minutes in this case) and the concentration of the compound. Tau is the mean blocking time for the compound.

The right half of the interface displays summary results from the current and previous measurements. For each of the samples tested (in this case A, B, C and D) the detected concentration of DTPMPA and TDP is plotted. In this case, three trials are completed for each sample resulting in a total of 12 complete measurements.

The samples in analyzed in Figure 64 are as follows
Sample A: DTPMPA 500 nM, TDP 0 µM
Sample B: DTPMPA 0 nM, TDP 0 µM
Sample C: DTPMPA 100 nM, TDP 0 µM
Sample D: DTPMPA 100 nM, TDP 150 µM

6. Development of a Demonstration System

Entering into the second year of the program a significant effort was made to develop a prototype stochastic sensing system capable of off-site operation. The goal was to detect nM quantities of a CWA simulant in the presence of µM quantities of an interferent using a portable apparatus. To date all of the stochastic sensing measurements had been made in controlled laboratory conditions and with no such time pressure as might be imposed during a live system demonstration. In order to achieve the system demonstration goal a number of subsidiary goals were identified and presented at the February 2007 program review:

1. Reliable production of the GNM
2. Develop a compact and robust test cell for operation with the GNM
3. Automate the bilayer formation procedure
4. Successfully transition the mutant αHL protein from the UT Arlington apparatus to a fieldable version employing the GNM
5. Automate the signal processing
6. Demonstrate high reliability of successfully completing the demonstration

Achieving these goals proceeded in parallel with the other elements of the program described above with a successful demonstration of stochastic sensing at an offsite demo in Arlington, VA in May 2008.

6.1. GNM Production

In order to provide GNM devices to multiple groups for experiments and have sufficient GNMs to develop a demonstration system, EBS developed processes to produce large quantities of GNMs. Initially EBS was trained on the production process from the University of Utah. EBS then implemented that process along with multiple changes to increase production to about 10 GNMs per week. This number generates enough devices to allow for multiple experiments in a variety of pore sizes to test membrane stability, ion channel lifetime runs, and automated bilayer formation techniques. Additional changes are still continuing to automate more of the process, however, current procedures meet current GNM needs.

The GNMs are produced in a multiple stage process. First, a 0.75 mm ID glass capillary housing with a Tungsten wire epoxied to a 25 µm Pt wire are created. The Pt wire is then etched in a sodium cyanide solution to create the conical tip. That tip is then sealed in the glass capillary using a hydrogen flame. This device is then sanded on multiple grits of paper and felt with polishing compound to expose the Pt tip and obtain the necessary surface smoothness for bilayer formation. The desired size of the GNM pore region (usually 200-1000 nm) can be targeted using a circuit developed by EBS. The Pt tip is then etched out of the pore region

using a calcium chloride solution. The GNM pore size is then measured and recorded. The GNM then goes through a silane process and is then ready to use for experiments. Below a couple of the process improvements are discussed that have allowed increased production:

Circuit for Targeting Pore Size
Previously at EBS, the breakthrough circuit that measured when the Pt tip was exposed was set to trigger immediately after breakthrough when doing hand polishing. The increase in area of the Pt disk was then monitored using the Ruthenium redox measurement for total Pt area. The breakthrough circuit was modified to allow for computer monitoring of the breakthrough voltage during polishing on an automated polishing machine. Multiple GNMs were then felted using the circuit and their sizes recorded. The results are shown in Figure 3. This circuit now allows for a specific size to be targeted with a voltage setting, also eliminating the need for a Ruthenium measurement. Specific pore sizes are useful for different experiments performed and it may be determined that a certain size is better than another for bilayer stability. Thus, this modification will drastically increase production as well as allowing for additional control on desired size ranges.

The breakthrough circuit was tested initially with Pt disks of known area (as determined by the Ru redox measurement). These were equated to the measured voltage on the breakthrough circuit. A plot of the measured voltage vs the known Pt disk radius is shown below.

Figure 3 – Voltage of the breakthrough circuit versus pore size

Targeting Pore Breakthrough on 1200 Grit Paper
One of the most time consuming steps of the GNM production process was the felting of the GNM with polishing compound. Felt times over 2 hours were not uncommon To help improve this process, the electronic circuit developed by EBS is used to expose the Pt tip in the pore on 1200 grit paper and then have it proceed to a set felting time of 8 minutes. Eventually automated polishers will replace sanding by hand and will further decrease production time.

6.2. Development of the Apparatus

Following the decision to move toward a demonstration system, EBS immediately began to pursue the development of a system concept and specific apparatus for use in an offsite demonstration system. The system must allow for the reliable formation of the sensor elements (lipid bilayer with ion channel on a GNM) and a relatively automated testing of multiple samples

containing various combinations of target analytes. The details of the evolution and development of this device are provided below.

6.2.1. First version of the millifluidic test article (MTA)

Prior to the development of a special purpose test apparatus, the apparatus used to make stochastic sensing or single channel measurements with the GNM were not well suited to portability. An example is shown in Figure 65. The various components of the apparatus are held with test tube clamps and arranged in a copper screened box. The GNM is moved down into the PDMS test cell in order to produce a bilayer and proceed with the incorporation of the sensing protein. Devices constructed in this manner must operate on vibration isolation tables to avoid movement of the suspended wires and components. Setup of such devices is also complicated and there is not a reliable means of introducing new samples for test.
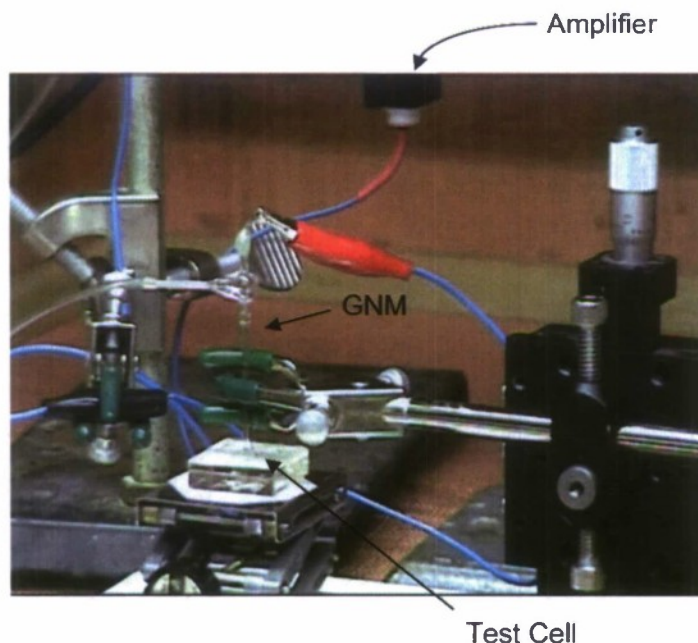
Figure 65. Early version of systems used for stochastic sensing measurements with GNMs. The copper screen from the enclosing faraday shield is visible in the background.

An initial design and build of the Millifluidic Test Article (MTA), which contains a 35 microlitre analyte chamber, electrode opening, inlet and outlet ports and a third port for possible alpha-hemolysin insertion was created in early 2007.

The MTA function is to automate the fluid delivery and extraction across the GNM within a small volume. The system includes a 10 cc syringe reservoir system that can handle different fluids (KCl, alpha-hemolysin, lipids, and analytes), a 6-way valve for switching between each fluid, the MTA, electrode holder with pressure gauge attached and a GNM, EBS receiver electronics to monitor events, and a peristaltic pump to control volume flow. The inlet tubing is 0.25 mm ID PEEK tubing and the outlet is 1 mm ID PEEK tubing that attaches to 0.51 mm peristaltic pump tubing. The overall layout of the planned system is shown below in Figure 66. The volume of the inlet line from the 6-way valve to the MTA is 10 µL and the line from the 6-way valve to the syringe is 250 µL (this is essentially part of the reservoir system).
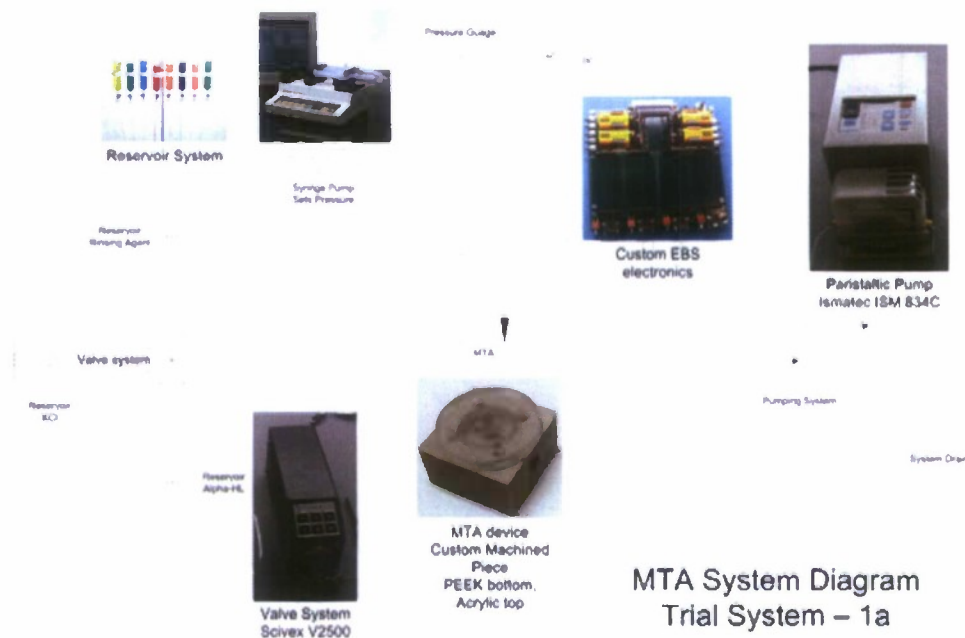
Figure 66. Preliminary layout for prototype stochastic sensing system.

The as built first system (Figure 67) was setup initially inside a faraday cage with all of the components except the syringe pump. The syringe pump was originally intended to inject the αHL solution into the test cell, but this approach was never implemented due to practical difficulties. As with the earlier system shown in Figure 65, much of the apparatus is held together with test tube clamps and the component integration is loose. This initial setup allowed for basic validation of the individual components including the peristaltic pump, the fluid switch and the concept of a flow through test cell.

Figure 67. Original setup of the MTA in a faraday cage.

Mechanical drawings of the first fluidic test cell for the MTA are shown in Figure 68. This design demonstrates a number of the features of later versions. The three threaded fluid ports in the body (Figure 68A) are compatible with standard hollow threaded screws used for fluid handling in liquid chromatography systems (see Upchurch Scientific). In the top right view, the top and bottom facing ports are the fluid inlet and outlet. The port to the left provides access for the reference electrode that is in contact with the electrolyte solution in the fluidic reservoir. With the cap in place (Figure 68B), the total fluid volume is ~35 µL. The GNM enters from the underside of the cell with the face of the GNM in the center of the fluid reservoir. The cap is put into place with the "vent" open and then a small screw is put in to seal the reservoir.
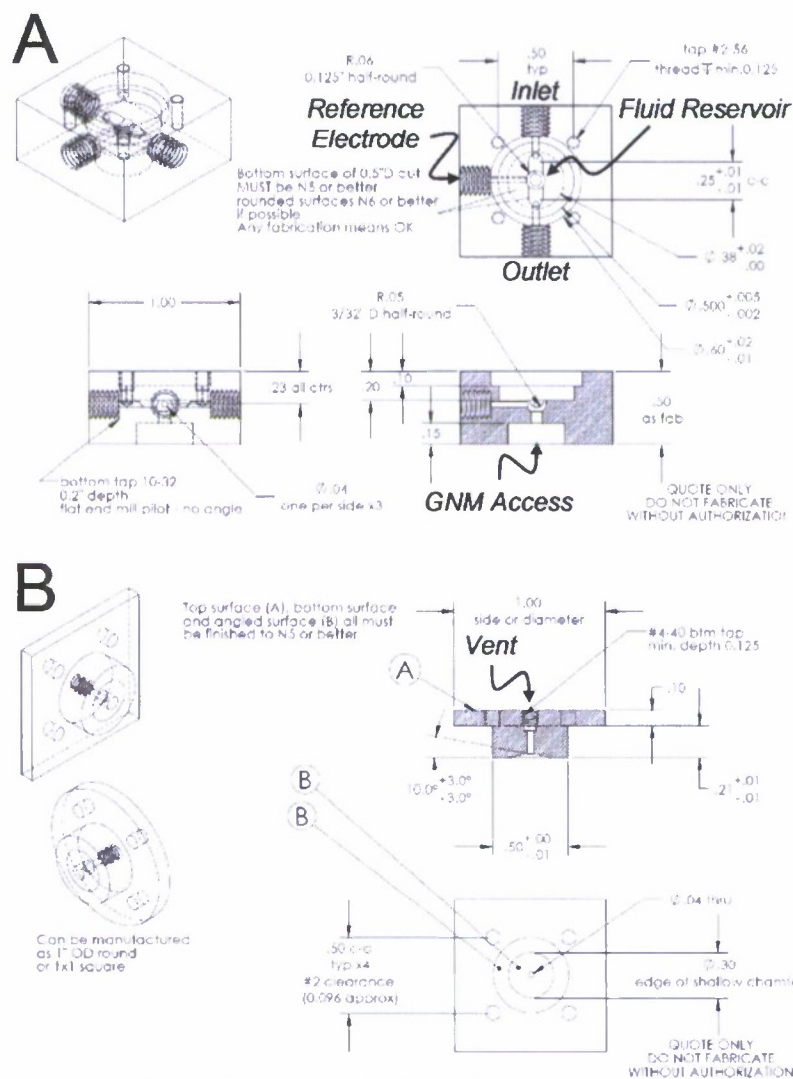
Figure 68. Details of the first fluidic cell for the millifluidic test article (MTA). (A) Body of the MTA fluidic cell. (B) Cover of the MTA fluidic cell.

Running the system consists of painting a bilayer across the GNM, seal the MTA with its cover, pumping an αHL containing electrolyte into the MTA, waiting for an αHL insertion, flushing with KCl (with the intention of limiting the number of insertions), then monitoring the blocking events. An example of the data viewed and recorded from the MTA operation with a GNM is shown in Figure 69. In this case the analyte beta-cyclodextrin is in the interior of the GNM and interacts with the trans side of the αHL.
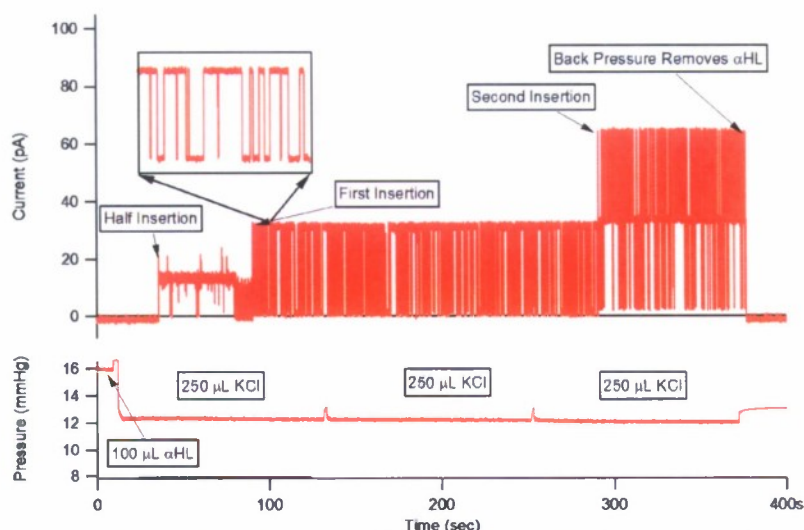
Figure 69. (Top) Measured current and (Bottom) pressure during operation of the MTA.

System control and data acquisition is handled by software written using the LabVIEW package. A example view is shown in Figure 70. The interface provides the user with full control over the applied voltage, data acquisition rate, filtering, and gain of the measurement. The software allows the user to automatically save data files in a binary format at a length determined by the user. Automated event detection provides the user with snapshots of rapidly occurring events. Additional information includes power spectral density plots and digital display of the applied DC voltage and measured DC current.
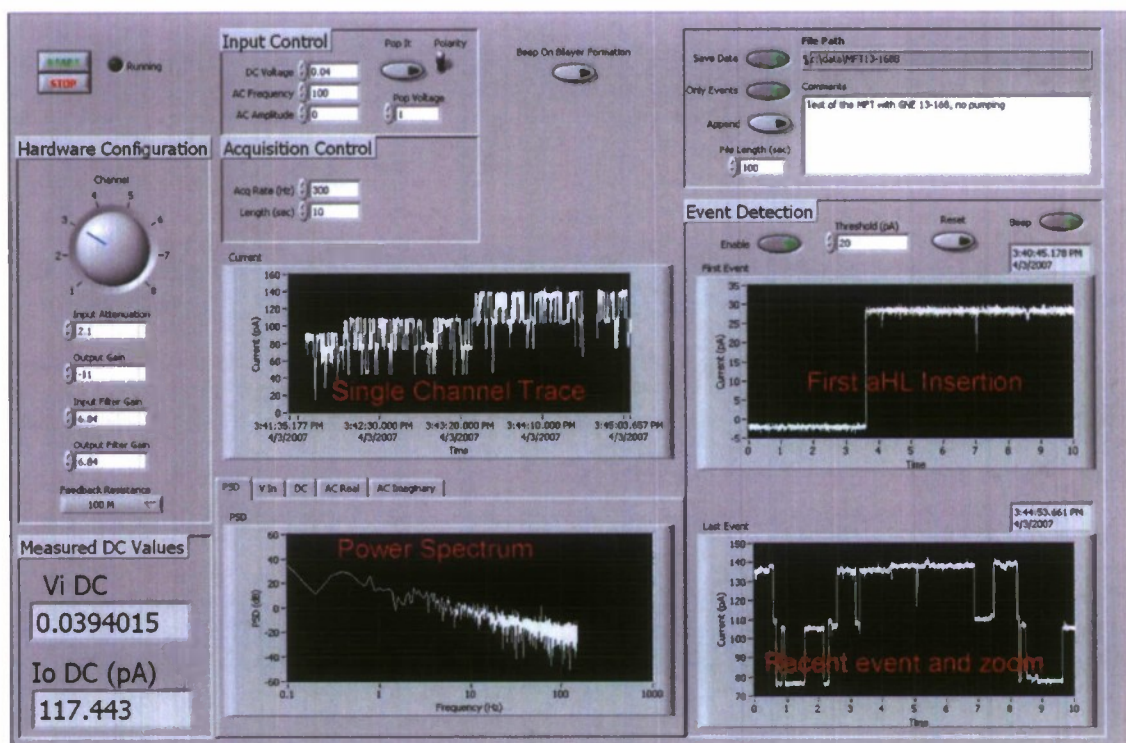
Figure 70. Current traces of αHL insertion and BCD switching events using the MTA and LabVIEW data acquisition program.

6.2.2. Improvements to the MTA - Version 2.0

In the next version of the system prototype a number of issues were addressed including:
- Placing the MTA chamber in a small shielded box to eliminate the large faraday cage
- The lid of the fluidic test cell was converted from a stopper to a slider configuration
- The design of the electrode inserted into the side of the MTA was improved to prevent breakage.

The primary components of the second generation MTA are shown in Figure 71. This version of the apparatus with some slight modifications over time was used extensively during early stochastic sensing work at EBS. Multiple units were constructed and utilized at both EBS and Utah.

The fluid cell and amplifier are securely mounted in an aluminum enclosure that serves as an electrical interference shield. Fluid lines have been reduced in length to limit dead volume and eliminate clutter.

In the original design, the top of the fluid cell was pressed into the test cell and sealed using a small set screw. The overpressure caused by inserting the top and set screw resulted in relatively frequent failure of the bilayer due to overpressure. In the new design, the top seals the fluid reservoir by sliding into place over an o-ring held in place by a recessed groove. The closed and open positions of the sliding top are shown in Figure 71B and C.
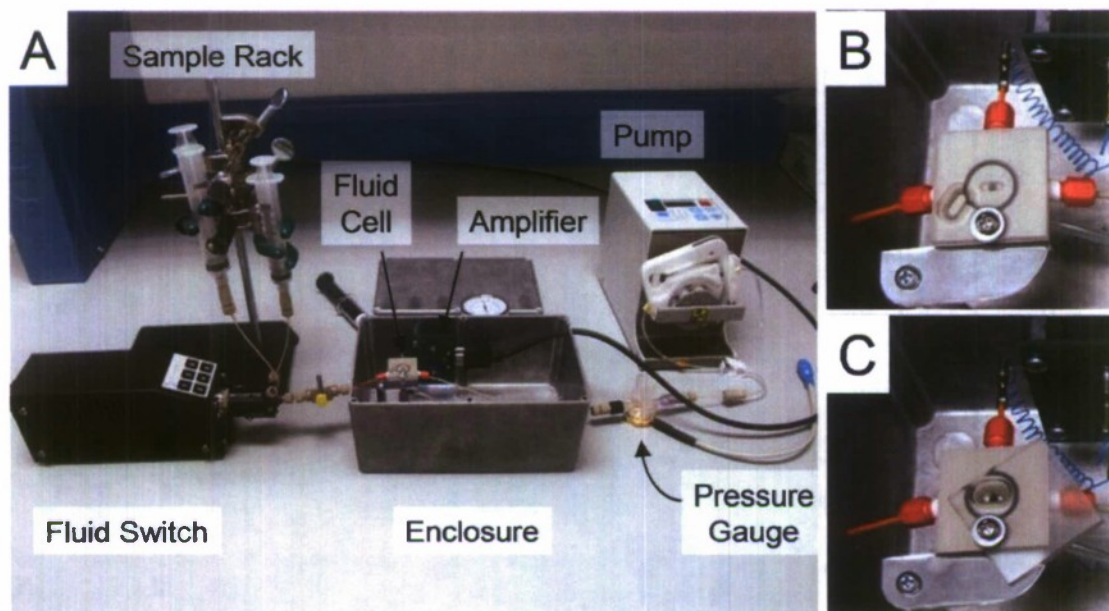
Figure 71. Version 2.0 of the MTA. (A) The overall system layout has been simplified and reduced in size. (B) and (C) The new fluidic test cell uses a sliding cover to prevent overpressure breakage of the lipid bilayer caused by insertion of the old style lid.

6.2.3. Automated Bilayer Formation

For the first two versions of the MTA, the bilayer has been formed using the painting method. The painting method involves the spreading of lipid/organic solvent across the surface of the GNM, using a pipette tip, in order to deposit a lipid bilayer across the nanopore aperture. The method requires a significant amount of training, since it is necessary for the operator to apply very precise pressure to the surface of the GNM and do so in a consistent manner. Such a method for bilayer formation has little hope of being automated

For the demonstration system, however, an automated (or capable of being automated) and reliable method is required to ensure the reliable operation. To this end, EBS investigated methods that would allow for rapid formation of the bilayer without the need for significant operator intervention and training. The result is the solution raise method for bilayer formation on a GNM surface. This method involves depositing a small amount of lipid/decane (10 mg/ml) on top of the buffer solution and raising the electrolyte solution height, up past the GNM surface. Although a fully automated version of the method has not been implemented, both the deposition of the lipid/solvent mixture and the raising of the fluid can be computer controlled.

The solution raise bilayer formation method begins by mounting a GNM, with its interior filled with an electrolyte solution, (horizontally or within 60 degrees of horizontal) into a test cell suitable for raising the height of an electrolyte solution containing a small amount of lipid, up past the surface of the GNM, in a systematic manner, in order to form a lipid bilayer across the GNM orifice. As shown in Figure 72, the GNM is initially mounted into the cell, which is then filled with an appropriate electrolyte solution, so that the height of the electrolyte solution is below the surface of the GNM. As with all of the single channel measurements described above, electrodes are located in the fluid reservoir and the interior of the GNM. Prior to the raising of the solution, the circuit between the two electrodes is effectively open and the resistance is too large to be measurable ($>> 1$ TΩ). A lipid/organic solvent mixture is then placed, drop-wise on the top of the electrolyte solution and is allowed to spread out over the surface of the electrolyte solution. The electrolyte solution is then raised up, past the surface of the GNM, resulting in the spontaneous formation of a lipid bilayer across the orifice of the GNM. With the bilayer in place the resistance between the two electrodes is on the order of $10 - 100$ GΩ. If a bilayer does not form, the solution in the GNM will be in contact with the solution in the test cell and the resistance between the electrodes will be $<< 1$ MΩ. By monitoring the resistance it is possible to manually or automatically determine the relative solution height and the presence or absence of a lipid bilayer across the aperture in the GNM. The solution height may be controlled manually using a syringe or automatically using an electronically controlled pump.

Lipid bilayers can be consistently reproduced by simply lowering the electrolyte solution height down past the surface of the GNM membrane and then re-raising it up. The pressure control system, Figure 72, allows the internal pressure of the GNM to be systematically controlled. As described in Section 3.2.2.3, a positive pressure is used to induce insertions of ion channels into the lipid bilayer suspended over the GNM orifice, while a negative back pressure is used to stop ion channel activity. The presence of a viable bilayer is verified by αHL insertion followed by detection of analyte or a calibration chemical.

1. Setup cell with GNM in holder (electrolyte solution height below GNM).
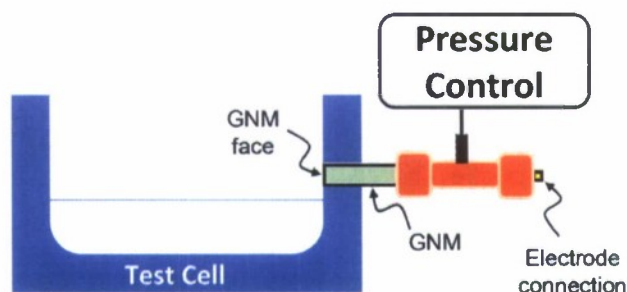
2. Apply small amount of lipid/decane to the electrolyte solution surface.
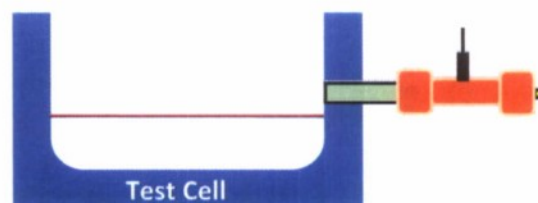
3. While holding back pressure (20-100 mm Hg) slowly raise solution height.
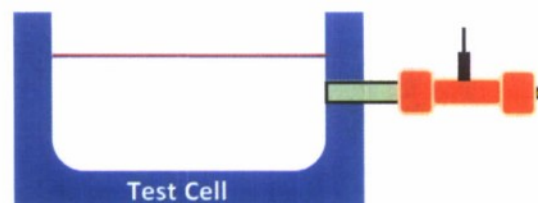
Figure 72. The solution raise method for automated bilayer formation using a GNM

Bilayer formation by the solution raise method is proposed to proceed as shown in Figure 73. The lipid/organic solvent mixture on the surface of the electrolyte solution slowly passes over the aperture of the GNM. As this happens, lipid and solvent are drawn into the GNM due to an attraction to the hydrophobic surface of the GNM. As the fluid level rises above the aperture, the lipid and solvent spontaneously assemble in a planar lipid bilayer, the lowest energy state for the small amount of lipid and solvent on the surface of the GNM.
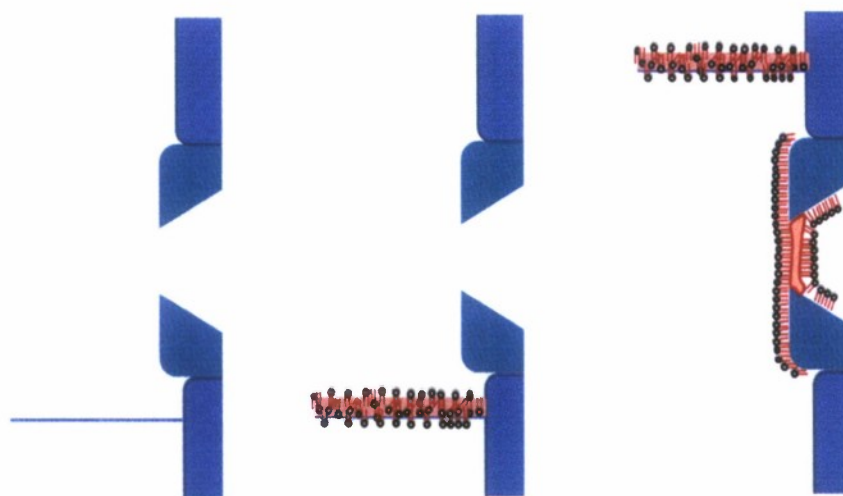
Figure 73. Schematic diagram depicting the formation of a solvent-containing lipid bilayer formed over the orifice of a GNM, using the single side automated bilayer formation technique.

The solution raise bilayer formation process has been adopted for use on all ion channel conductance measurement systems developed by EBS. Extensive testing has demonstrated that the bilayers produced by the solution raise method are as robust as those produced by the painting method and are far more reliable to form.

6.2.4. Incorporating automated bilayer formation into the MTA – Version 3.0

A new version of the fluidic cell was designed to incorporate the new solution raise method for bilayer formation. In the new design, Figure 74, the fluid inlet is placed below the level of the horizontal GNM in order to produce the raising and lowering of the fluid level to form bilayers. The fluid outlet is placed above the GNM. The system is sealed with a hinged lid that seals against an o-ring held in a recessed groove. In addition, a latching mechanism is used to securely hold down the lid of the device. The base of the fluidic cell is designed to fit into a secure platform housed within the metal enclosure of the MTA (see right side of Figure 74).
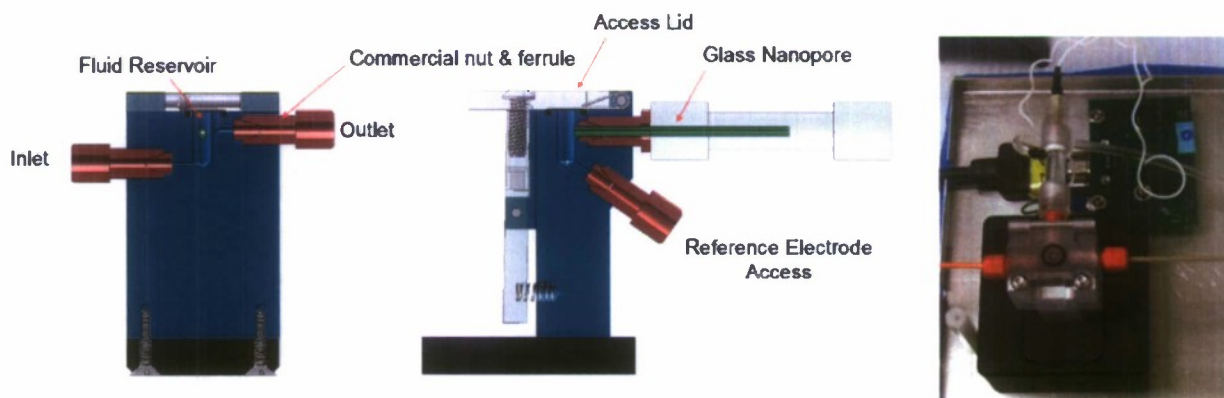
Figure 74. Solution raise fluidic cell for use in the MTA.

Mechanical drawings of the primary components of the solution raise fluidic raise test cell are provided in Figure 75.
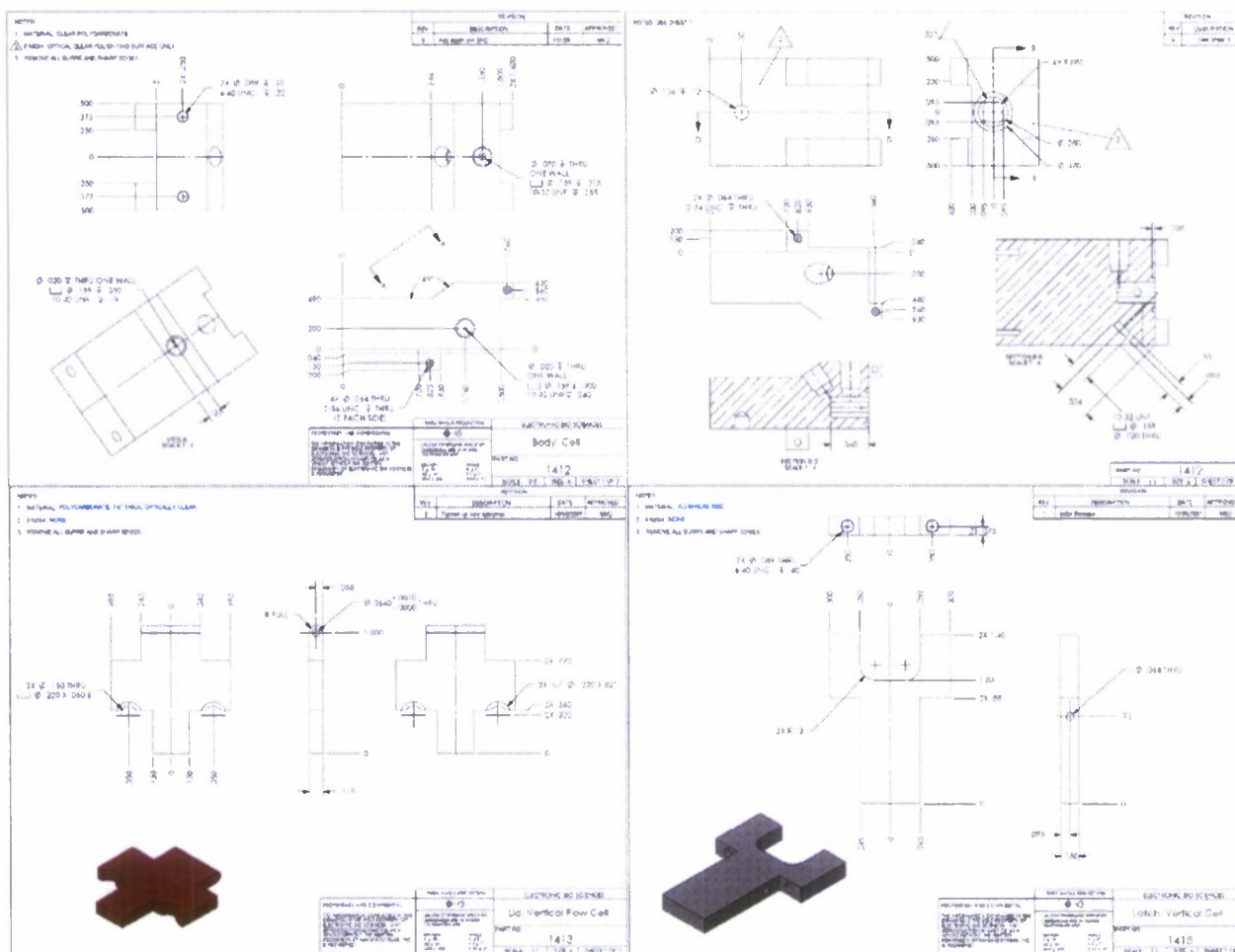
Figure 75. Mechanical drawings of the critical components of the solution raise fluidic test cell.

Rapid sample exchange using the solution raise fluidic test cell in the MTA was demonstrated with DTPMPA and TDP detection. A series of single channel current traces are shown in Figure 76 that demonstrate the performance. In the first panel a blank electrolyte solution produces no visible binding events. The test cell is then flushed for ~2 minutes at 150 µL/min to introduce the 500 nM DTPMPA sample. The next samples tested are blank, 100 nM DTPMPA, blank and 100 nM DTPMPA + 200 µM TDP. In each case, the measured signal accurately matches the composition of the sample. In future versions of the system we will reduce the volume of the test cell (~200 µL for the tested version of the system) to reduce the required flushing time and volume.
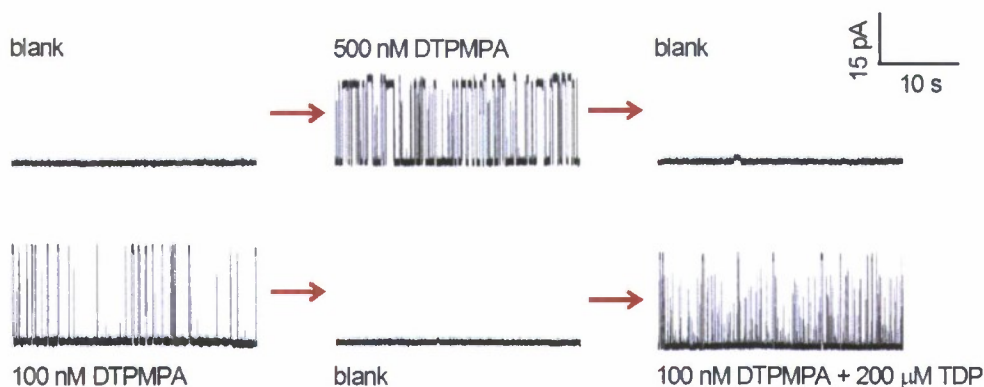
Figure 76. Demonstration of capability to flow in and flow out samples using the solution raise fluidic test cell. A 2minute flush time was used between detection of each sample. The flow rate was ~150 µL/min.

6.2.5. The Demonstration System

The final demonstration system was to be a relatively self contained and portable system for use outside of the laboratory. To this end, EBS integrated all of the elements of the MTA into a plastic carrying case. The complete prototype system is shown in Figure 77. The system allows for the injection of multiple samples selected by an automated fluid switch. The sample mixed with electrolyte flows through 500 µm diameter tubing to the test cell described in Figure 74. The end of a GNM device with a lipid bilayer and inserted αHL channel is exposed to the interior of the test cell. Sensitive receiver electronics coupled to electrodes in the GNM device and the test cell record the conductance through the channel. A computer (not shown) digitizes the conductance signal and performs an automated analysis of the single channel data. A single peristaltic pump drives the flow through the system and runs the excess electrolyte into a small waste receptacle. The test volume can be flushed with blank electrolyte to remove any traces from the analyte under test. The total volume of electrolyte used per measurement (including flushing of the test cell) is ~<1 ml. This system represents a *first* prototype for a portable ion channel based sensor system. As will be described later in the report, this system has been successfully tested at multiple offsite locations to demonstrate detection capabilities in a non-laboratory setting. In addition, dramatic size and complexity reductions are readily achievable.
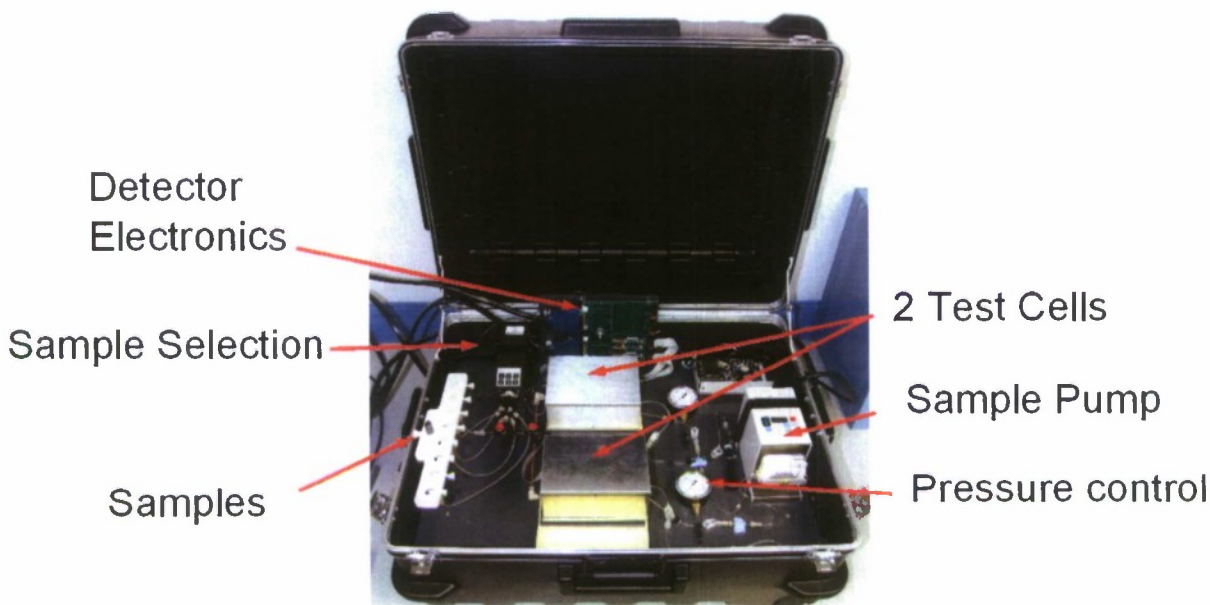
Figure 77. Prototype sensor system based on the GNM platform. Labeled modules are described in the main text.

An example of the single channel data resulting from the prototype ion channel sensor system is shown in Figure 78. With a blank sample (electrolyte only) no interaction with the ion channel is observed. The introduction of the chemical warfare agent simulant, DTPMPA, causes characteristic blocking (closure) of the ion channel. Increasing the concentration of DTPMPA produces a proportional increase in the number of events per unit time. The addition of a high concentration of the interferent TDP produces very rapid blocking events that are much shorter and less complete than the blocking events produced by DTPMPA. Successive samples can be run indefinitely. In the event of a bilayer failure, a new bilayer can be formed automatically and ion channels inserted.
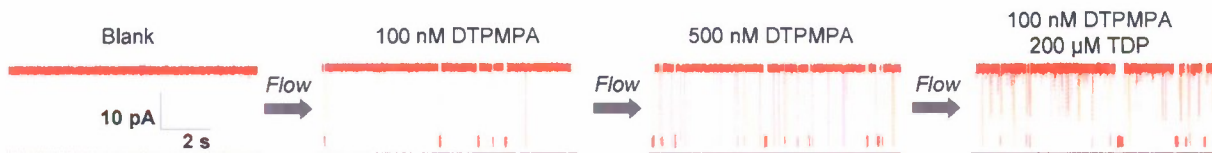
Figure 78. Sequential ion channel sensing of blank and organophosphate containing samples.

6.3. The Protein

6.3.1. Limited quantity from IVTT

UT Arlington demonstrated that nM quantities of CWA simulants can be detected in the presence of interferents using the $(M113K)_7$ protein. This work was done using a laboratory apparatus at UTA that is not suitable for incorporation into the prototype system. This being the case, it was necessary to transition the $(M113K)_7$ protein from the UTA apparatus to a GNM based platform.

Considerable work with the wild type αHL monomer and heptamer had been completed using the GNM platform prior to efforts to employ the modified $(M113K)_7$ protein. This being the case,

it was thought at the time that transitioning the $(M113K)_7$ protein to the GNM platform would be a relatively simple task. As was learned during this stage of the program, such a transition was actually not straightforward.

The standard method for using the αHL protein is to add a small amount of solution containing the protein to the reservoir of the test apparatus. In the UTA laboratory, the IVTT method is used to produce ~25 µL quantities of ~1 µg/ml protein. A small quantity (~0.5 µL) is added to the ~0.2 mL test cell. When using the ~200 µL fluidic cell with the MTA, EBS and collaborators traditionally add ~0.2 µL of a 1 mg/ml solution of the wild type αHL in the monomer form. The final concentration of protein in the UTA system is approximately one thousand times more dilute than that used with GNMs. The volumetric comparison is not ideal since the protein is always added near the lipid bilayer, but the UTA system does use a far smaller quantity of protein. The reason for the greater concentration requirement when using a GNM is likely due to the significantly smaller area of the nanopore in the GNM. Based on are arguments alone, one would expect that the concentration or protein used for the GNM should be > 20,000 X that needed for a 150 µm aperture in a Teflon film.

Understandably, initial attempts to use the UTA protein directly on a GNM did not meet with success. The UTA group worked to produce larger and more concentrated batches of the $(M113K)_7$ protein, but successful incorporation of protein was only reported on a few occasions after hundreds of trials and many variations on experimental conditions.

6.3.2. Producing M113K via Expression in E-Coli

The solution to the problem was to produce the protein by a method that will yield significantly larger quantities than the IVTT method used by UTA. To this end, EBS worked with a commercial protein synthesis laboratory (Paragon Bioservices) to produce large quantities of the M113K protein via expression in E-Coli. The procedure used is described below:

The DNA sequence for the M113K protein was incorporated into a cloning vector by DNA 2.0. The expression construct generated at DNA 2.0 was then used to transform E. coli BL21 to generate clones for expression screening. Induction experiments (1 mM IPTG, 3hrs) were performed on five colonies. SDS-PAGE or immunoblot was then run to compare the protein expression and the best expresser was chosen for production.

The best expressing clone was scaled 15 L fermentation. Cells were grown in LB medium and the culture was induced with 1 mM IPTG for expression. After three hours, the cell paste was harvested by centrifugation and stored at -20 °C until purification. SDS-PAGE was performed on an analytical sample to confirm the protein expression.

Recombinantly expressed protein was then purified following standard procedures [43]. Briefly, cell paste from the synthesis was lysed using a microfluidizer, and clarified by centrifugation. Clarified lysate was brought to 75% saturation with Ammonium Sulfate in order to precipitate the protein. After one hour at 4 °C, precipitated protein was collected by centrifugation and resuspended in a 10 mM Na-Acetate buffer (pH 5.0) with 20 mM NaCl. Solubilized material was then clarified by centrifugation and loaded onto a SP-Sepharose column. Bound protein was washed and then eluted using a linear NaCl gradient (0 - 500 mM). Pooled fractions containing the αHL protein were then concentrated and further purified using Size Exclusion chromatography.

The SDS-PAGE results for the purified fractions are shown in Figure 79. The molecular weight of the protein is ~35 kg/mol. The SDS-PAGE shows a strong band at ~38 kg/mol that is associated with the M113K protein.
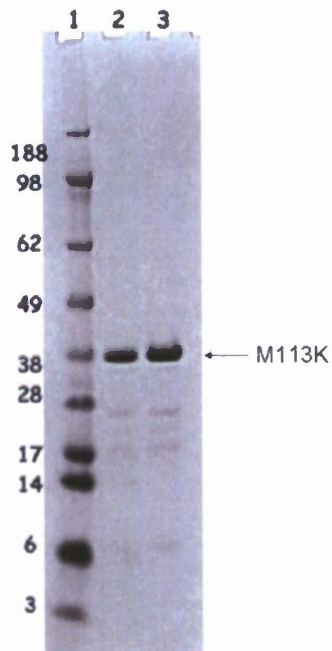
Figure 79.   SDS-PAGE results for the purification of M113K protein from Paragon Bioservices.   Molecular weight in kg/mol is indicated on the left.   Lane 1: Molecular weight marker. Lane 2: 1 µg. Lane 3: 2 µg.

Paragon Bioservices also produced the oligomerized form of the protein, $(M113K)_7$.   The method used by UTA to oligomerize the protein in the presence of rabbit blood cells was not pursued as this requires specific medical capabilities that were not available at Paragon. An alternative method was used based upon the work of Walker et al [43].

The final purified protein was oligomerized in the presence of 6.33 mM Na-deoxycholate at room temperature. Oligomerization was analyzed by SDS-PAGE and the results are shown in Figure 80.   The oligomer appears at ~150 kg/mol which is significantly smaller than the expected 230 kg/mol for (M113K)7. There is also a significant quantity of the monomer present near 35 kg/mol.   Based on these results, it was not clear whether the oligomerization was successful.
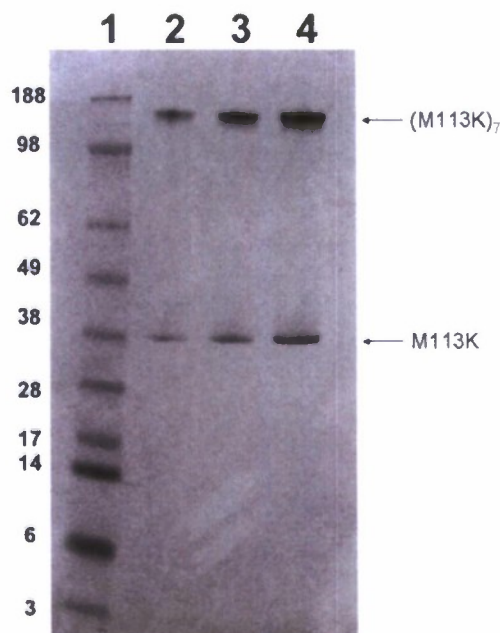
Figure 80. SDS-PAGE results for the purification of $(M113K)_7$ protein from Paragon Bioservices. Molecular weight in kg/mol is indicated on the left. Lane 1: Molecular weight marker. Lane 2: 1 µg. Lane 3: 2 µg. Lane 4: 5 µg.

Monomeric and oligomeric forms of the purified protein were concentrated to approximately 1 mg/ml, dialyzed into 10 mM Tris-C1, pH 8, and stored frozen at -80 °C. The final yield was ~ 90 mg of monomeric protein. 20 mg of the protein was retained as the monomer and the balance was used for oligomerization. The final yield for the oligomerization was ~7 mg of protein (~10% yield).

6.3.3. Initial Tests with M113K Expressed by E-Coli

EBS met with immediate success when using the Paragon M113K samples. An early example of the positive results is shown in Figure 76. The protein provided results very similar to those measured by the UTA group, Section 4.2.3, and incorporating the protein into the bilayer of the GNM was possible at concentrations comparable to those used for wild type αHL, 6.3.1.

EBS had to address a few minor difficulties with the M113K protein. For example, after a few seconds of acquiring data the conductance would drop to near zero and remain very low until the driving voltage is toggled to open the pore. Gating of the αHL protein was found to be dependent upon the presence of divalent metal cations such as calcium and magnesium. By adding a chelating agent such as EDTA at ~1 mM, the divalent cations were removed and gating of the pore became very infrequent.

The pre-formed oligomers from Paragon Bioservices, however, did not function properly. Many insertions with fractional conductance levels (i.e. the conductance is smaller than that measured for a properly functioning (M113K)7 protein) made it very difficult to take reliable measurements. Due to excellent performance of the monomeric M113K, attempts to use the Paragon (M113K)7 were not pursued further.

7. System Demonstration

7.1. Practice Demonstrations

To prepare for the demonstration and work out operational issues with the demonstration prototype, EBS performed multiple practice demonstrations using the demonstration system. Tests were performed at EBS, at EBS' sister company QUASAR and at a nearby hotel in San Diego. The final test at the hotel provided fine tuning of the procedures for system transport and setup outside of a laboratory environment.

Summary results from the San Diego practice demonstrations are shown in Figure 81. In each case the detection results for DTPMPA and TDP closely matched the actual concentrations of the test samples. All tests were run using the same calibration parameters as described in Section 5.4.
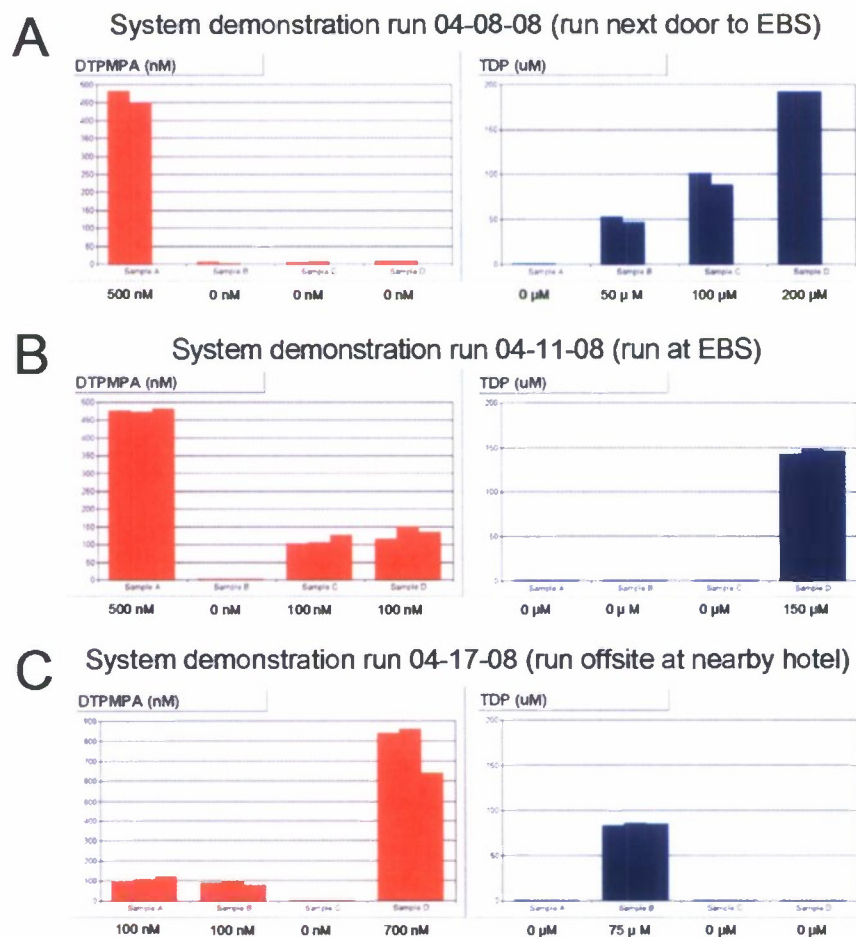
Figure 81. Summary results from practice demonstrations in San Diego. Ground truth concentrations are shown below each set of measurement results.

A practice demonstration was also performed in Arlington, Virginia prior to the final system demonstration.
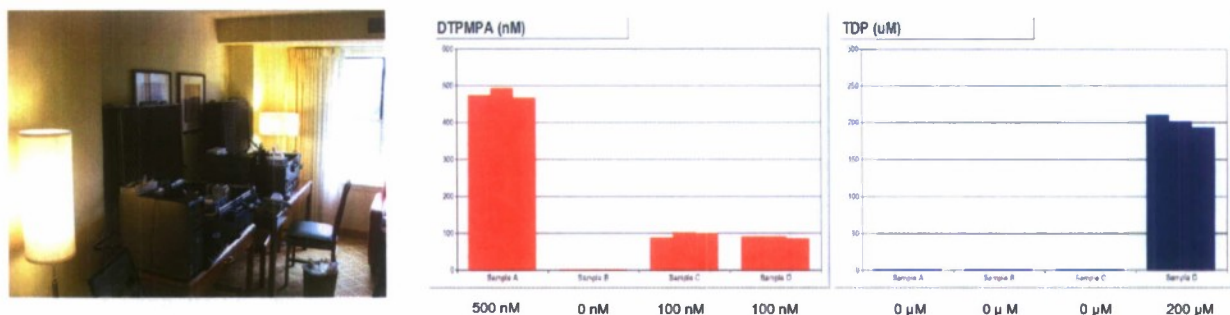
Figure 82. (Left) Site of the practice demonstration run in Arlington, VA on April 30, 2008. Two systems were set-up in parallel and the final demo was run on one system. (Right) Results from the April 30 practice demo

All of the practice demonstrations were run with the following solution conditions: 1.0 M NaCl, 10 mM Tris (pH 7.0), 2 mM EDTA. Measurement times were 3 minutes with a 2 minute flush cycle between measurements.

7.2. Official System Demonstration

Objective: In an off-site, non-laboratory environment, demonstrate the ability of an ion channel based stochastic sensor to detect ~2 ppb concentration chemical warfare agent simulant (DTPMPA) in the presence of a 4 ppm interferent (TDP).

Preparations: On the afternoon prior to the demo, the MOLDICE team set-up 2 stochastic sensing systems developed on the MOLDICE program. Basic operation of the systems was verified and the remaining preparations were left to the morning of the demo.

On the morning of the demo the MOLDICE team used semi-automated methods to complete the setup of the stochastic a sensor. Bilayers were formed on the glass nanopore supports and a single organophosphate sensitive ion channel (the $(M113K)_7$ mutant of the αHL protein) was inserted into the bilayer. Proper functioning of the ion channel was verified with test solutions of organophosphates.

Demonstration: The demo proper began at 1:30pm on 5/2/08 and continued until 3:30pm. Data was collected for ~3 minutes with each of the following aqueous solutions 500 nM DTPMPA, 100 nM DTPMPA, blank solution, and 100 nM DTPMPA in 200 µM TDP (Samples A, B, C, D). Between each solution the sample chamber was flushed for ~2 minutes. After each 3 minute run, the data was processed on a separate computer using an automated analysis program developed on MOLDICE. A screenshot of the analysis results at the end of the demo is shown in Figure 83. The top left panel shows the raw stochastic sensing data with DTPMPA and TDP molecules producing characteristic blocks of the current through the ion channel. The middle left panel shows the distribution of blocking times used to identify the components of the sample and determine the concentration of the target compounds. The bottom left panel shows the results for the last run analyzed (average blocking time and concentration of target compound). The bar charts to the right show the measured concentration of DTPMPA and TDP in Samples A, B, C and D for the 3 sets of runs completed during the demo. Sample A registers DTPMPA concentration from 480-600 nM. The blank, Sample B, shows a trace amount of DTPMPA (likely due to a small amount of contamination from Sample A). Sample C registers 90-120 nM DTPMPA. Sample D shows a mixture of DTPMPA (~100 nM) and TDP (estimated concentrations from 230-260 µM). All of the measurements are consistent with the composition of the samples with a relative concentration error of 10-20%.
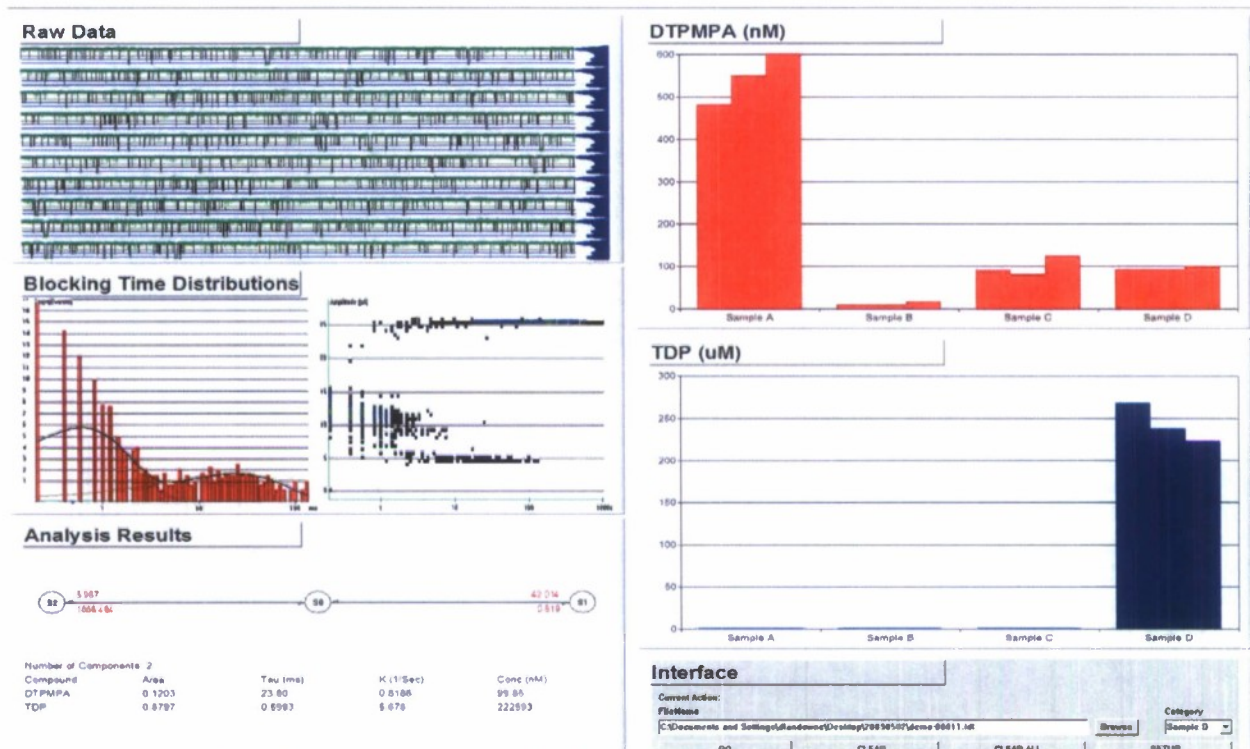
Figure 83.   Results from the MOLDICE demonstration on 5/2/2008.   Details are presented in the text.

With the successful offsite practice and final demonstrations, the MOLDICE team has successfully demonstrated the operation of an ion channel based stochastic sensing system outside the laboratory environment.

8. Nanopore Sequencing of DNA

8.1. Background and Motivation

The primary focus of the MOLDICE program has been to develop stochastic sensing for the detection of chemical warfare agents.   There is also considerable interest in the detection of biological warfare agents (BWA).   Detection of BWA is traditionally accomplished by either the detection of specific proteins or specific DNA sequences unique to the target agent (e.g. viruses or bacteria).   The most specific detection methods utilize DNA sequence detection to avoid high false alarm rates common for immunoassays designed to identify specific proteins.   The drawback with the DNA sequencing methods is the high cost of both the equipment and reagents necessary to accurately identify even short stretches of DNA.   Under the MOLDICE program we pursued an investigation of nanopore based DNA sequencing.

The idea of using the current blockade of a protein pore to sequence a single strand of DNA was first developed by NIST researcher John Kasianowicz in the mid 1990's.   The basic concept is to pass single stranded DNA (ssDNA) through a protein pore embedded in a planar lipid bilayer and observe the change in current as the ssDNA translocates through the pore [44]. See Figure 84.   Traditionally, the lipid bilayer is suspended across an ~100 μm in diameter orifice that separates two buffered electrolyte filled reservoirs.   Proteins such as the alpha toxin of staphylococcus aureus (αHL), spontaneously assemble into pores in such lipid bilayers. When a voltage is applied between the two reservoirs, current flows through the pore.   As

molecules pass through the pore, the peak current level is reduced by a characteristic amount depending upon the nature of the translocating molecule.
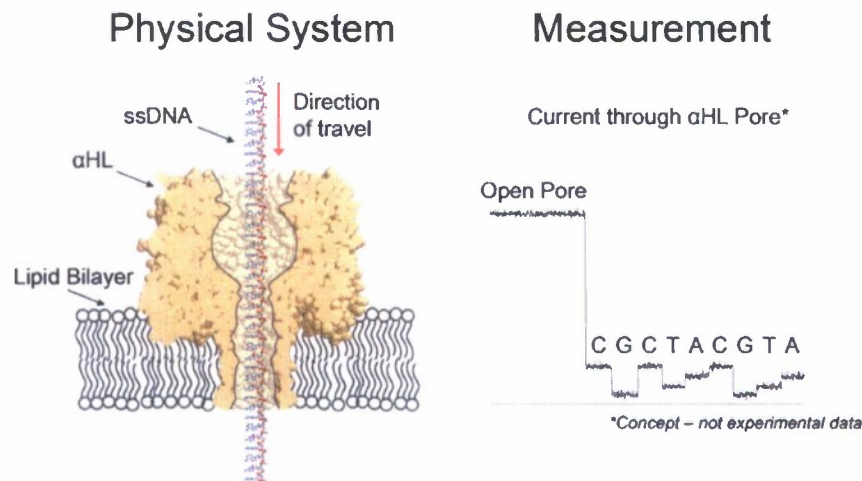
Figure 84. Nanopore sequencing of DNA based on the translocation of ssDNA through αHL. The data to the right is the ultimate goal of the method – direct readout of the DNA sequence.

Kasianowicz teamed with researchers at Harvard and UCSC to demonstrate the translocation of ssDNA through the protein pore αHL [44]. The initial results showed that the duration of the decrease in current is proportional to the ssDNA length and inversely proportional to the voltage driving the polynucleotide through the pore. This work led to numerous other groups applying both protein pores and artificial nanoscale pores in attempts to sequence DNA.

Astier et al., showed the detection of distinct, individual blocking signals for all four DNA bases, with signal differences of order ~1 pA to 4 pA (at 120 mV bias) as shown in Figure 85A [45]. Meller et al., reported similar differences in current level between poly(dA) and poly(dC) [46]. Using ssDNA with a terminal hairpin structure, Ashkenasy et al., showed detection of a single nucleotide change within a polynucleotide (Figure 85B) and measured a significantly larger difference between poly(dA) and poly(dC) [47].
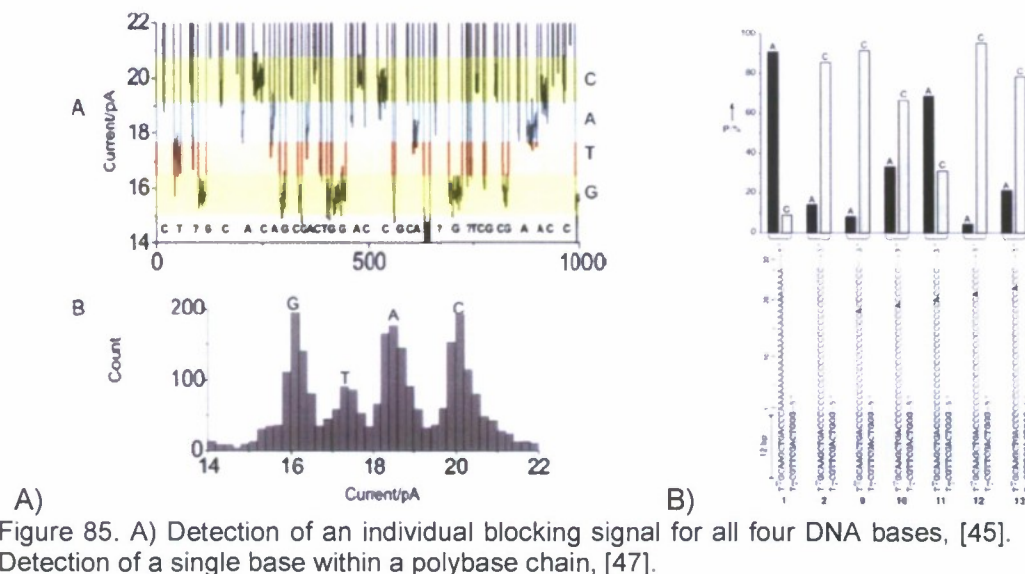
Figure 85. A) Detection of an individual blocking signal for all four DNA bases, [45]. B) Detection of a single base within a polybase chain, [47].

Presently, the principal limitation with using a protein pore for direct DNA sequencing is that the polymer translocates through the protein pore too quickly for the signals of individual nucleotides to be resolved using available single channel measurement systems. The basic protein pore conductance measurement requires the application of a DC potential in order to measure a DC current. The measured current is merely the voltage potential acting on the impedance of the pore and the bilayer. With a fixed noise level, the sensitivity or signal to noise ratio may be increased by increasing the DC potential. However, the polynucleotide is charged and will move through the protein pore faster as the potential is increased. At an applied potential of ~120 mV, the polynucleotide has a velocity of ~1 nt (nucleotide) per 1-2 µs [46]. To properly detect the passage of a single nucleotide it would require a detection bandwidth in excess of 1 MHz. Unfortunately, the current noise increases with the bandwidth of the measurement. At 1 MHz, the current noise will be in excess of 100 pArms as shown in Figure 86.
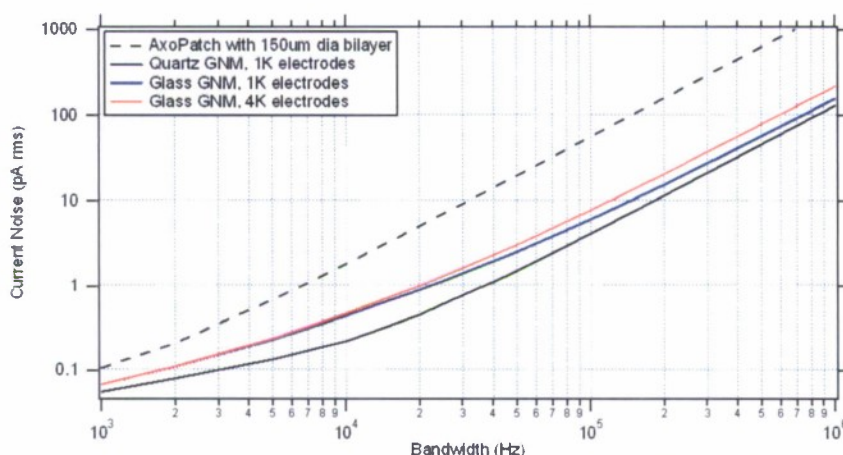
Figure 86. Current noise vs. detection bandwidth for conventional systems (AxoPatch with 150µm diameter bilayer) and low noise systems employing glass nanopore membranes (GNMs).

An associated limitation is the very rapid diffusion of the ssDNA in the pore. At 15 C, the diffusion rate of poly(A)$_{50}$ (a single strand of 50 adenosine units) ssDNA has been measured to be ~2.5×10^{-10} cm^2/s [13]. Assuming a spacing of 4 Å between bases [48-50], the DNA will have a characteristic diffusion length of ~1 base every 10 µs. Diffusion alone will blur the distinction between individual bases unless diffusion is reduced by ~2 orders of magnitude.

In order to measure changes between nucleotides in a single strand of ssDNA, it will be necessary to significantly slow the translocation and diffusion of ssDNA. To this end, EBS developed an AC based nanopore system to characterize the kinetics of ssDNA motion at low temperatures and evaluate the feasibility of using an AC bias to monitor the conductance of the protein pore during DNA translocation.

8.2. Introduction to the Experiment

Mathé et. al., recently devised an experiment to measure the voltage free diffusion of a DNA hairpin containing a polydeoxyadenosine (poly-A) tail as it escapes from an αHL pore [51]. In their experiment the DNA hairpin is initially driven into the αHL channel using a DC drive voltage (120 mV$_{dc}$). The ssDNA tail of the hairpin is driven through the nanopore until the larger hairpin prevents further motion. Once the ssDNA tail of the hairpin has been captured within the pore, it

is released by turning off the DC drive voltage. A short time later, between 100 and 10,000 μs, the DC bias is turned back on in order to probe the conductance of the pore and determine the probability of the ssDNA tail remaining within the constriction of the protein pore. Using the general formalism derived by Lubensky and Nelson[52], which describes the one-dimensional motion of a homopolymer translocating through a narrow pore with which it has a strong interaction, Mathé et al. were able to derive the bias free diffusion constant for DNA escaping out of an αHL pore. Motivated by the work of Mathé et al. and the theoretical analysis provided by Lubensky and Nelson, we examined the escape time of a similar DNA molecule out of an αHL pore using an AC probing signal.

The use of an AC measurement has significant potential advantages in comparison to the conventional DC measurement. Combining an AC probing signal with a DC drive voltage provides the capability to separate the electric field used to produce the probing current from the electric field used to drive the biomolecule into and through the nanopore.[48] This combination offers the potential benefit that a high amplitude AC signal (i.e., > 150 mV_{ac}) can be used to monitor the conductance of the pore, significantly increasing the signal-to-noise ratio (SNR) of the measurement over conventional DC measurements (120 mV_{dc}). In addition, an AC signal places a lower net driving force on a biomolecule in comparison to a DC signal. Indeed, because an AC electrical field with zero offset is alternately driving the biomolecule into and then out of the nanopore over a single cycle, the AC electric field effect on driven translocation is substantially decreased relative to a constant driving force produced by a DC electric field.
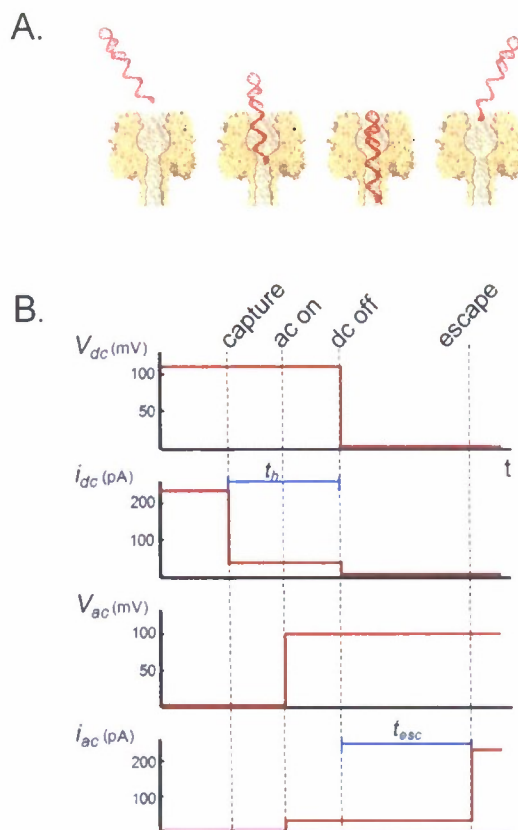
Figure 87. (a) An illustration of the capture and subsequent release of a DNA hairpin molecule, by an αHL pore. (B) Time line of the DC drive voltage (V_{dc}), AC probing signal (V_{ac}), along with their associated current responses (i_{dc} and i_{ac}, respectively) for the DNA capture and release measurement. Initially, only V_{dc} is on, which drives the DNA hairpin molecule into the αHL pore. Once the DNA hairpin is captured, V_{ac} is turned on and V_{dc} is turned off, allowing the DNA hairpin to escape from the αHL pore, as seen in i_{ac}.

The experimental procedure by which a DC drive voltage is used to capture a DNA molecule within a nanopore while an AC probing signal is used to monitor the conductance of the nanopore once the hairpin is released is depicted in Figure 87. Initially, the αHL pore is in an open (unblocked) state and the DC drive voltage (V_{dc}) is on (120 mV$_{dc}$), driving the DNA molecule into the αHL pore. Once the ssDNA tail has been driven into the pore, up to the hairpin, and is captured, as determined by a drop in DC current (i_{dc}), the AC probing voltage (V_{ac}) is turned on in order to monitor the conductance of the αHL pore. A short holding time later (t_h), V_{dc} is turned off and the DNA molecule is allowed to escape out of the pore. The escape time (t_{esc}), defined as the time it takes from when V_{dc} is turn off to the time when the DNA molecule leaves the pore, seen as an increase in the AC current (i_{ac}), is then measured. This technique allows the exact escape time of the DNA to be measured in the absence of a DC bias. Likewise, instead of setting V_{dc} to zero, V_{dc} can be set to a positive or negative value in order to determine the effect of a DC drive bias on the escape times of the DNA molecule.

The escape times of the DNA molecule have been measured as a function of AC probing signal amplitude, temperature, DC bias, and AC probing signal frequency. By determining the effect of these parameters, we have been able to obtain a clearer picture of the dynamic polymer/pore interaction. Following the theoretical analysis provided by Lubensky and Nelson [52], our results

are generally predicted by a one-dimensional asymmetric periodic potential model, across which the DNA molecule diffuses in order to escape the pore. In order to move into or out of the αHL pore, the HP-A$_{50}$ molecule must be thermally activated over the potential barrier presented by the asymmetric periodic potential. A DC bias added to the asymmetric periodic potential serves to tilt the periodic potential up (negative DC bias) or down (positive DC bias), driving the biomolecule into or out of the pore, respectively. By introducing the AC probing signal to the one-dimensional asymmetric periodic potential model, which oscillates the periodic potential between an up and down state, we have been able to determine the asymmetry factor (α) which describes the level of spatial asymmetry in the model.

8.3. Experimental Section

8.3.1. Chemicals and materials

NaCl (Alpha Aesar), Tris (Sigma), HCl (Alpha Aesar), and EDTA (Sigma) were used as received. Wild-type α-hemolysin (αHL) (lyophilized powder, monomer) (Sigma) was used as received. 1,2-diphytanoyl-*sn*-glycero-3-phosphocholine (DPhPC) (Avanti) was obtained in powdered form, and diluted to a concentration of 10 mg/ml in decane (Aldrich). All solutions were prepared using H$_2$O (18 MΩ•cm) from a Barnstead E-pure water purification system.

PAGE purified DNA (5'-GGGTCAGCTTGCTTTTGCAAGCTGACCC-A$_{50}$-3') (HP-A$_{50}$) (Sigma-Genosys), was obtained at 100 µM in 10 mM Tris (pH 8.5), 1 mM EDTA. Before each experiment, the HP-A$_{50}$ solution was heated to 95 °C in a water bath for 10 minutes, before cooling it to 8 °C for 20 minutes.

8.3.2. Glass Nanopore Membranes and Bilayer Formation

Glass nanopores were used as described in Section 3.2.2. Typical aperture sizes were 400 – 900 nm in radius. The GNM was filled with 3.0 M NaCl, 10 mM Tris-HCl (pH 7.2), 1.0 mM EDTA. A Ag/AgCl electrode, prepared by oxidizing a 0.25-mm diameter Ag wire in Bleach (Clorox) for ~30 min, was placed inside the glass capillary. The capillary was then inserted into a pipette holder (Dagan) that is connected to a 5 ml gas-tight syringe (Hamilton) and a pressure gauge (Fisher). The syringe and pressure gauge were used to control the pressure across the suspended bilayer during ion-channel recordings, as described in Section 3.2.2.3.

The glass capillary was horizontally mounted to the small polycarbonate cell small (~175 µl volume) described in Section 6.2.4, which contains a second Ag/AgCl electrode. The cell reservoir was filled with 3.0 M NaCl, 10 mM Tris-HCl (pH 7.2), 1.0 mM EDTA, so that the height of the electrolyte solution lies above the GNM surface. Bilayers were formed using the either the painting method [48, 53] or the solution raise method described in Section 6.2.3. Successful lipid bilayer formation was indicated by the formation of a 50-100 GΩ seal, measured between the two Ag/AgCl electrodes. After bilayer formation, αHL and the DNA hairpin were both added to the cell (outside of the GNM) to a final concentration of ~0.5 µM and ~1.0 µM, respectively.

8.3.3. Alternating Current Capture and Release Measurement

The custom instrumentation and apparatus used in the alternating current DNA hairpin capture and release measurement are depicted in Figure 88. A desktop computer (Dell) is used to control an AC source (National Instruments PCI-6289) producing a bias between a Ag/AgCl electrode outside the GNM and a second Ag/AgCl electrode, which is held at virtual ground, inside the GNM. Using custom electronics developed by EBS, the AC current across the bilayer

and protein pore, is summed with the inverted AC source before being amplified and measured. By summing the AC current signal with the amplitude and phase adjusted inverted AC drive voltage, the capacitive current associated with the shunt capacitance of the GNM and bilayer (~1.5 pF) can be reduced by over 80 dB or a factor of 10,000. The analog cancellation of the capacitive current reduces the dynamic range requirements of the data acquisition system sufficiently to allow for the use of off-the self data acquisition cards. This instrumentation configuration allows a high amplitude (up to 500 mV$_{ac}$) high frequency (up to 250 kHz) AC signal to be monitored. All data was collected at an AC source frequency of 100 kHz except where noted. After band pass filtering the amplifier output at the AC frequency with a bandwidth of 100 kHz, the signal is digitized (National Instruments PCI-6132) at 800 kHz, digitally demodulated with the simultaneously acquired source AC signal, phase adjusted to separate the real (resistive) and quadrature (capacitive) components, and finally sampled at the AC frequency. The resulting signal has an effective bandwidth of 50 kHz due to the quadrature detection method. The resistive component of the current is of primary interest as it measures the conductance of the αHL pore, so all analysis is performed on this component of the measured signal. For control purposes, the system also measures the DC current, albeit at a bandwidth under 100 Hz. Customized software in National Instruments' LabVIEW is employed for all system control, data acquisition and signal processing described above.
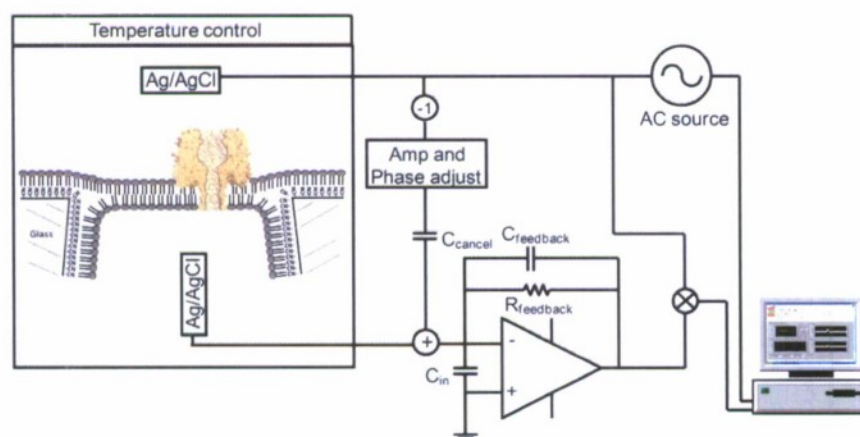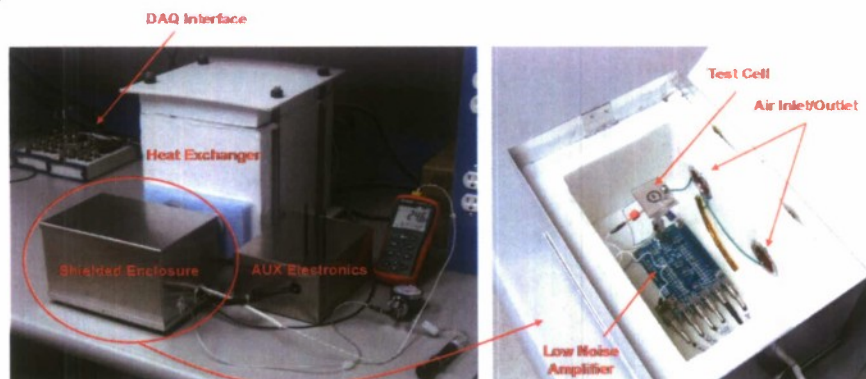
Figure 88. (A) Schematic diagram and (B) photograph of the instrumentation used in the AC+DC DNA hairpin capture and release experiment.

The αHL pore conductance is monitored as the 3' end of the HP-A$_{50}$ molecule is threaded into the αHL pore from the *cis* side. Initially, the AC voltage is turned off and a 120 mV DC bias is used to drive the DNA molecule into the αHL pore. The AC voltage is initially turned off so that it does not affect the capture of the DNA molecule. Once the DNA molecule has been captured as seen in the measured DC current (data not shown) the AC bias is turned on, as depicted in Figure 87. The AC voltage is turned on 100-250 ms after the DNA molecule has been captured. Following, an additional 100 ms the DC drive voltage is set to zero. The DNA molecule is allowed to escape out of the *cis* side of the pore, and the exact moment of escape is measured in the AC current signal as an abrupt increase in current, as seen in Figure 89. Approximately 2 seconds after the DNA molecule has escaped the AC voltage is turned off and the DC drive voltage is again turned on, in order to repeat the measurement cycle. This procedure is computer controlled, allowing thousands of capture and release measurements to be made. In some experiments, after capturing the DNA molecule and turning on the AC probing voltage, the DC drive voltage is set to a positive value in order to drive the DNA molecule out of the αHL pore at an increased rate. The temperature of the system is controlled down to -15 $^{\circ}$C using a Neslab RET 740 refrigerated bath (Thermo Scientific) and custom heat exchanger. Data analysis was performed using Igor Pro 6 (WaveMetrics).
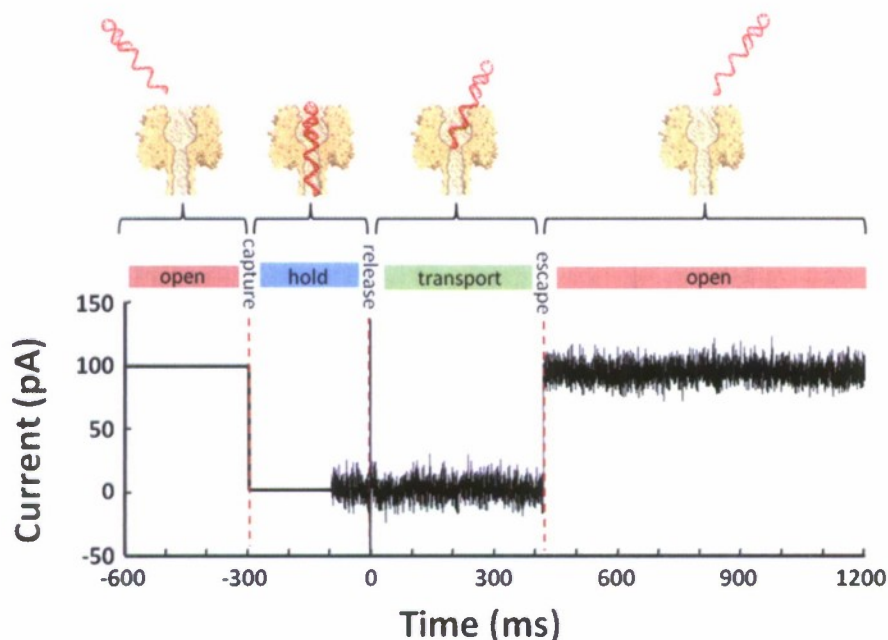
Figure 89. A representative AC current as a function of time plot, depicting the capture (illustrated data hand drawn) and subsequent release of the of the HP-A$_{50}$ molecule by an αHL pore. The HP-A$_{50}$ molecule is initially drawn into the αHL pore using a DC bias of -120 mV. Once the hairpin is captured, it is held within the αHL pore for ~300 ms before the AC signal (150 mV$_{ac}$ for this data) is turned on. Approximately 100 ms later, the DC bias is set to 0 V, allowing the DNA molecule to escape from the αHL pore. The sharp dual directional spike, seen at $t = 0$ ms, corresponds to the time at which the DC signal is turned off. This data was collected at 0 $^{\circ}$C.

8.4. Results and Discussion

Lubensky and Nelson have presented a theoretical look at the one dimensional motion of a biopolymer translocating through a biological pore, with which it has a strong interaction [52].

They theorized that as long as the motion of the polymer backbone was sufficiently slow relative to the other degrees of freedom, then motion in the x-coordinate (through the length of the αHL pore) was the only dynamic variable associated with DNA translocation. The remaining degrees of freedom could be described by the free energy of the biopolymer $\Phi(x)$, which includes the contributions associated with the electrostatic interactions between the biopolymer and the pore.

By simplifying the problem in such a manner, Lubensky and Nelson were able to describe the diffusion of the DNA molecule using the Smoluchowski equation. They went on to propose a sawtooth periodic potential model in which the minimum of the periodic potential had been shifted by the asymmetry factor, α. This asymmetry parameter has a large effect on polymer translocation time because the time required to move over the energy barrier, either into or out of the pore, depends exponentially on the energy barrier height. If the asymmetric potential is tilted up or down, as in the presence of a driving force, the potential energy barrier in the forward and reverse direction can be significantly different, resulting in different mean drift speeds for the polymer in the forward and reverse direction.

In presenting our results let us first describe the motion of DNA as it escapes from the αHL pore. Initially, the single stranded tail of the HP-A_{50} molecule is driven into the αHL pore, up to the hairpin, and is captured. The DNA molecule, modeled as a single particle that must be thermally activated to step over a potential energy barrier in order to take a single step out of or into the pore, must take 50 (the number of nucleotides in the tail) more steps out of the pore than it takes into the pore, in order to escape. Each one of these steps will be over an energy barrier from one minimum of the asymmetric periodic potential to the neighboring minimum, where the periodicity of the asymmetric periodic potential, defined as the distance between the two minimas, is equal to the base-to-base spacing of the ssDNA tail.
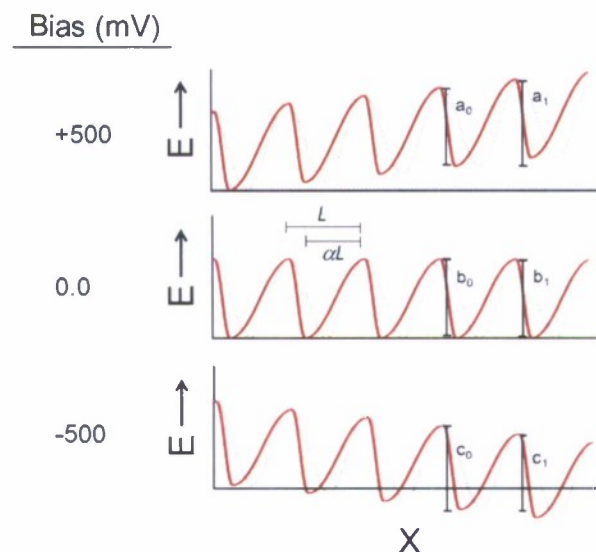
Figure 90. A schematic representation of the one-dimensional asymmetric periodic potential model in the presence of a +500 mVdc, 0.0 mV and -500 mVdc bias, as labeled. The asymmetric periodic potential is shown by the solid line while a symmetric periodic potential is shown by the gray dashed line.

A visual schematic of the actual asymmetric periodic potential that the HP-A_{50} molecule must overcome in order to move into or out of the αHL pore is presented in Figure 90. This schematic

shows the case of an asymmetric periodic potential, α = 0.7 (solid line) compared to a symmetric potential, α = 0.5 (dotted line) in the presence of varying bias levels, 500 mV_{dc}, zero, and -500 mV_{dc}. An asymmetry parameter of 1 would push the minima in the 0 bias potential left to the point where the minima and maxima occur at the same location. The intermediate asymmetry parameter of 0.7 pushes the minima left ~40% of the distance to the maxima. As depicted, the DC bias serves to tilt the asymmetric periodic potential either up or down. A result of the asymmetry is that as the asymmetric periodic potential is tilted up and down, the energy barrier into or out of the pore is different. Indeed, in cases were α > 0.5 the energy barrier to escape out of the pore while the asymmetric periodic potential is tilted down (c_1) is less than the energy barrier to insert into the pore when the potential is tilted up (a_0). Likewise, if α < 0.5 the energy barrier to escape out of the pore, while the asymmetric periodic potential is tilted down would be greater than the energy barrier to insert into the pore when the potential is tilted up. By using an AC probing signal which serves to repeatedly tilt the asymmetric periodic potential between the up and down states, we have not only been able to probe the effect of an AC signal but we have also begun to map out the exact structure of the asymmetric periodic potential by determining the height of the activation energy barrier and the asymmetry parameter associated with a polydeoxyadenosine escaping out of the *cis* side of an αHL pore. We will first introduce our experimental results before outlining the theory of combining an asymmetric periodic potential model with an AC probing signal, in order to theoretically model the mean escape time of the HP-A50 molecule out of the αHL pore as a function of AC amplitude, DC amplitude, and temperature.

8.4.1. AC Effect

Increasing the AC monitoring signal amplitude significantly affects the escape times of the HP-A_{50} molecule. Continually capturing and releasing HP-A_{50} molecules, a few hundred times, allows a histogram of the escape times to be constructed. Figure 91 shows three representative escape time histograms, plotted on a semi-logarithmic axis, depicting the escape times of the HP-A_{50} molecule. The escape times were monitored using a 100 kHz AC probing signal with peak amplitudes of 50 mV_{ac}, 100 mV_{ac}, and 150 mV_{ac}, as labeled. This data was collected at 20 °C.
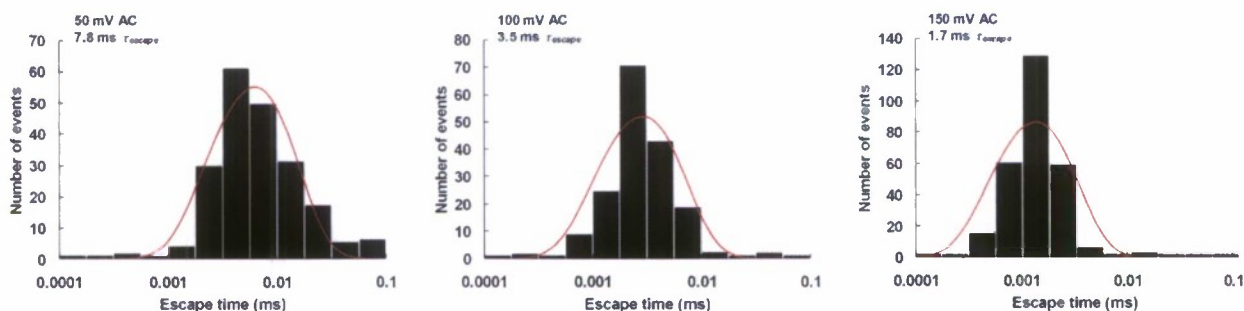
Figure 91. Time distributions of the HP-A50 molecule escaping from an αHL pore using a 50 mV, 100 mV, and 150 mV AC signal, as labeled. Each histogram was constructed from a few hundred events. Each distribution was fit to a one-dimensional asymmetric periodic potential model described by Equation 1. These data were recorded at a temperature of 20 °C.

The mean escape time for each data set was determined by fitting the histograms to the one dimensional diffusion model developed by Lubensky and Nelson:

$$\Psi(t) = \frac{1}{2v}\sqrt{\frac{D}{\pi t^3}}\left(1 - e^{-\frac{vL}{D}}\right)\sum_{k=0}^{\infty}\left(\frac{(2k+1)^2 L^2}{Dt} - 2\right)e^{-\frac{kvL}{D}}e^{-\frac{(vt-(2k+1)L)^2}{4Dt}}$$ Eq. 1

where v is the drift velocity of the polymer, D is the diffusion coefficient, t is time, and L is the length of the polymer. With v and D determined by the best fit to the histograms, the mean escape time of the HP-A$_{50}$ molecule is given by:

$$t_{mean} = \frac{L}{v}\left(\frac{2}{1-e^{-\frac{vL}{D}}} - \frac{2D}{vL} - 1\right)$$ Eq. 2

As depicted in Figure 91, an increase in the applied AC probing signal amplitude results in shortened mean escape times for the HP-A$_{50}$ molecule. At 50 mV$_{ac}$ the mean escape time for the HP-A$_{50}$ molecule is 7.8 ms, at 100 mV$_{ac}$ the escape time is 3.5 ms, and at 150 mV$_{ac}$ the escape time is 1.7 ms.

In addition to AC amplitude, the mean escape time of the HP-A50 molecule is also a function of temperature. The mean escape time of the HP-A$_{50}$ molecule, as a function of applied AC bias (peak) at 20 °C, 10 °C, 0 °C, and -10 °C, is depicted in Figure 92. Each data point along with its respective standard deviation was determined by collecting several hundred escape events using a minimum of three different αHL pores and reformed bilayers. The solid line associated with each data set, corresponds to the best fit, using the one-dimensional asymmetric periodic potential model described below.

Figure 92. The mean time required for HP-A$_{50}$ to escape from the αHL pore, as a function of applied AC amplitude (peak height) at four different temperatures (-10 °C, 0 °C, 10 °C, and 20 °C). The solid lines correspond to best fits, using the one-dimensional asymmetric periodic potential model described by Equation 5.

As depicted in Figure 92, an increase in AC amplitude results in shorter escape times. Although, the AC signal, which is centered at zero, is positive over half of each cycle and negative over

the other half of each cycle, the net driving effect does not appear to average to zero. At low AC amplitudes (< 30 mV_{ac}) the influence of the AC electric field appears to be very weak, while larger applied AC levels produce a marked reduction in the escape time. Escape times can be increased by decreasing the temperature of the system. A 10 degree decrease in temperature results in almost an order-of-magnitude increase in mean escape time.

While Figure 92 presents the escape times of $HP\text{-}A_{50}$ in the presence of an AC electric field, the extrapolated escape time at zero AC can be used to determine the diffusion coefficient of HP-A_{50} within the pore. The diffusion coefficient was determined from a model based extrapolation to zero V_{ac}, depicted in Figure 92. The details of the model are presented below. Diffusion coefficients were calculated from the one-dimensional diffusion equation, $L^2 = 2Dt_{esc}$, where L, the length of HP-A_{50} tail, is equal to 20 nm, assuming the length of a single nucleotide is 0.4 nm [48-50]. Figure 93 depicts the natural log of the HP-A_{50} diffusion coefficient, as it escapes out of the *cis* side of the αHL channel, as a function of inverse temperature. The Arrhenius plot, closely follows a straight line with a slope equal to $-E_a/R$, (Ea is the activation energy barrier for thermally activated diffusion, and R is the molar gas constant), and an intercept equal to the natural log of the pre-exponential factor (the diffusion coefficient at infinite temperature). Based on a linear best fit in Figure 7, an energy barrier of 1.8×10^{-19} J must be overcome in order for the HP-A_{50} molecule to either move one step out of or one step into the αHL pore, in the absence of an applied bias.
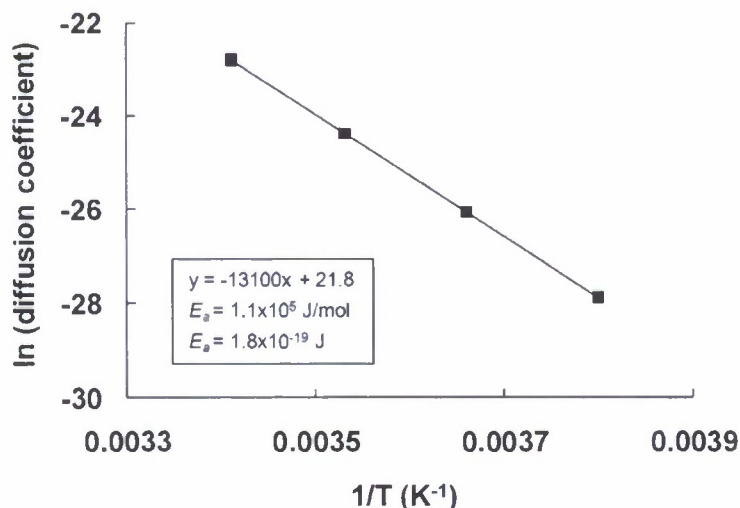
Figure 93. The natural log of the diffusion coefficient for HP-A_{50} within the αHL pore, as a function of inverse temperature. Diffusion coefficients were determined from the extrapolated bias free escape times, determined from the data shown in Figure 92.

Overall, a reduction in temperature from 20 °C to -10 °C had resulted in a reduction in the diffusion coefficient of ~200X. This significantly changes the characteristic diffusion length. Instead of diffusing ~1 base every 10 µs, the ssDNA will now diffuse ~1 base every 1.5 ms.

8.4.2. DC Effect

The applied DC drive voltage has a large effect on the escape time of the negatively charged HP-A_{50} molecule. For example, by applying a negative DC drive voltage, the HP-A_{50} molecule can be driven into and held within the αHL pore. Conversely, a positive DC voltage can be used to drive the HP-A_{50} molecule out of the pore, after it has been captured. The escape times of the

HP-A_{50} molecule as a function of DC bias and at a fixed temperature of 0 °C are presented in Figure 94. These escape times are monitored using a 100 kHz AC probing signal with a peak height of 50 mV_{ac}, 150 mV_{ac}, and 250 mV_{ac}, as labeled. The solid lines associated with each data set corresponding to the best fits using the one-dimensional asymmetric periodic potential model described below.
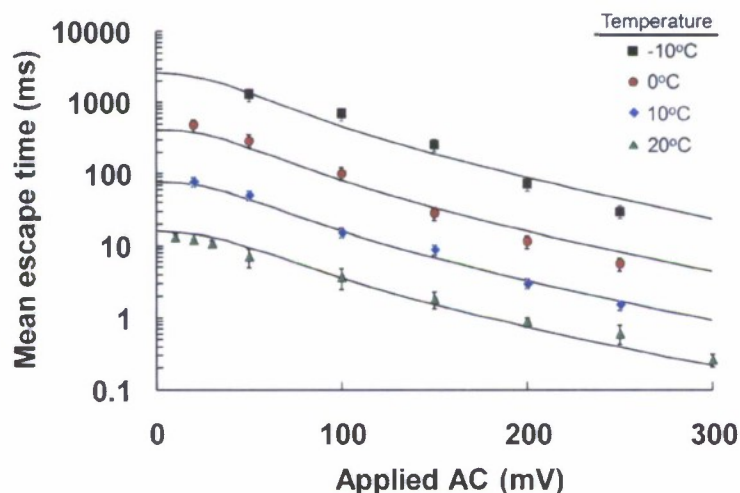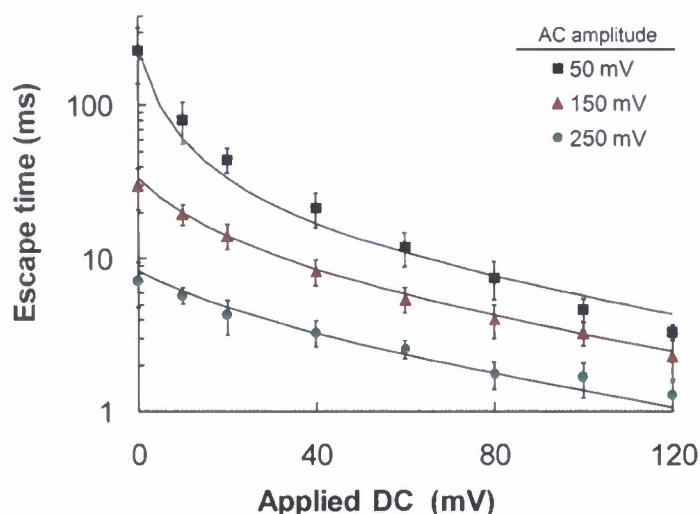

Figure 94. The mean time required for HP-A_{50} to escape from the αHL pore, once it has been captured, as a function of applied DC bias at three different AC amplitudes (50 mV, 150 mV, 250 mV) and at a temperature of 0 °C. The solid lines correspond to best fits, using the one-dimensional asymmetric periodic potential model described by Equation 5.

The escape times become shorter as the DC drive voltage, used to drive the HP-A50 molecule out of the pore once captured, becomes larger. The escape times, monitored using a 50 mV AC signal, decrease by well over an order of magnitude as the DC drive voltage is increased from 0.0 to 100 mV_{dc}. This result is in good agreement with the work by Wanunu et. al. who demonstrated that a change in DC drive voltage, from 0 to 80 mV_{dc} (15 °C), resulted in an approximately 2 orders of magnitude decrease in escape times for a similar hairpin containing a poly-A tail [54].

8.4.3. Frequency Dependence

As depicted in Figure 95, the frequency of the AC probing signal has little effect on the escape times of the HP-A_{50} molecule. There is no statistically significant difference in escape times between 60 and 200 kHz. This means that the response time of the HP-A_{50} molecule is fast (<< 5 μs) relative to the time variation of the electric field used to probe its motion. Within the frequency regime used here, HP-A_{50} has adequate time to react and migrate under the influence of the applied electric field. We anticipate that there is a frequency regime (> 200 kHz) where the AC field variation is faster than response time of HP-A_{50}, and the overall effect of the AC field may be reduced. In this theoretical case a large signal (i.e., > 1.0 V) could be used to monitor the conductance of the αHL pore, without placing a driving force on the DNA molecule.
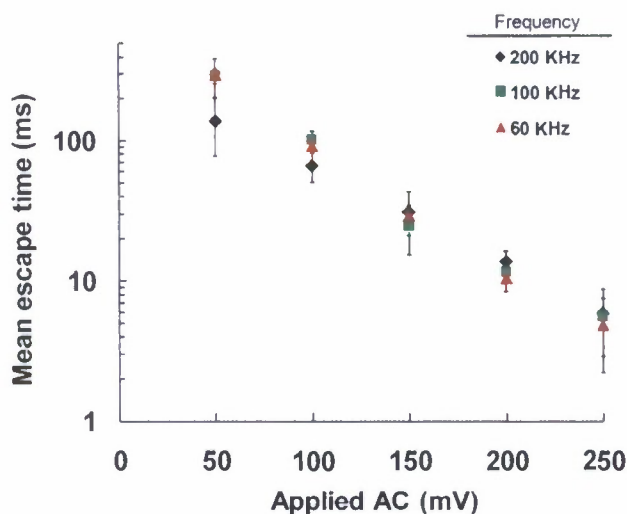
Figure 95. The mean time required for HP-A$_{50}$ to escape from the αHL pore, as a function of applied AC amplitude at three different frequencies (60 kHz, 100 kHz, and 200 kHz). This data was collected at 0 $^{\circ}$C.

8.4.4. AC Influence on the One-Dimensional Asymmetric Periodic Potential

We assume the DNA molecule can be modeled as a single particle that must be thermally activated to jump over the potential energy barrier from one minimum of the asymmetric periodic potential to the neighboring minimum. The rates at which the molecule takes one step out of the pore or one step into the pore are κ_{out} and κ_{in}, respectively. In order for the HP-A$_{50}$ molecule to escape, it must step out of the pore N times more than it steps into the pore, where N is the number of nucleotides in the HP-A$_{50}$ tail. When the two escape rates are equal (in the absence of an applied electrical field), the mean number of steps to escape is equal to N^2. When the escape rates are unequal, there is a bias towards moving in the direction of the higher rate, and the mean number of jumps to escape changes accordingly.

In order to calculate the mean number of jumps to escape, let us label the initial position of the DNA by x, and define $\bar{n}_x\,(N,\,p_{out})$ as the mean number of steps to escape. The probability that the DNA steps out of the pore (p_{out}) is given by:

$$p_{out} = \frac{\kappa_{out}}{\kappa_{out} + \kappa_{in}} \qquad\qquad\qquad\qquad \text{Eq. 3}$$

We can now define a recursion relation for $\bar{n}_x$:

$$\bar{n}_x = 1 + p_{out}\,\bar{n}_{x+1} + (1 - p_{out})\bar{n}_{x-1} \qquad\qquad\qquad \text{Eq. 4}$$

For the two endpoints we have: $\bar{n}_{N-1} = 1 + (1 - p_{out})\bar{n}_{N-2}$ (because $\bar{n}_N$ is zero by definition) and $\bar{n}_0 = 1 + \bar{n}_1$ (because the presence of the hairpin prevents a jump to x = -1). Equation 4 can be readily solved by starting at the end (with $\bar{n}_{N-1}$) and working back to $\bar{n}_0$. Setting N = 50 we find that for p_{out} = 1, $\bar{n}_0$ = 50; for p_{out} = 0.5, $\bar{n}_0$ = 2500; and as p_{out} goes below 0.5, $\bar{n}_0$ rapidly increases.

If the mean number of steps for escape is known, the mean time to escape can be computed, given that the mean time for a single step is the reciprocal of the sum of the rates. Thus, the mean escape time is:

$$\bar{\tau} = \frac{\bar{n}_0(N, p_{out})}{\kappa_{out} + \kappa_{in}}$$

<div align="right">Eq. 5</div>

where $\bar{n}_0(N, p_{out})$ is the mean number of hops needed to escape, once the HP-A$_{50}$ molecule has been fully captured ($x = 0$). Determining the mean escape time has now been reduced to calculating the escape rates κ_{out} and κ_{in} as a function of the applied DC and AC voltages.

In order to move into or out of the αHL pore, the HP-A$_{50}$ molecule must be thermally activated over the potential barrier presented by the periodic potential $\Phi(x, t)$. For barrier heights that are large compared to kT, the escape rate over this potential can be calculated using Kramers' escape rate [55, 56]:

$$\kappa = \frac{1}{2\pi} \frac{\sqrt{\Phi''(x_{min}) | \Phi''(x_{max})|}}{m\gamma} e^{-\frac{\Phi(x_{max}) - \Phi(x_{min})}{kT}}$$

<div align="right">Eq. 6</div>

where m is the effective mass of the DNA molecule, γ is a parameter describing friction between the DNA and its environment, $\Phi(x_{max})$ is the maximum value of the periodic potential, $\Phi(x_{min})$ is the minimum value of the periodic potential, k is Boltzmann's constant, and T is temperature. If we use as an example the case of an asymmetric cosine potential, that has been stretched on one side of the minimum and compressed on the other side of the minimum by the asymmetry parameter α ($\alpha = 0.5$ describes a symmetric periodic potential), and place it in the presence of a DC field which adds a linear potential term to the asymmetric cosine potential, we get

$$\Phi(x) = \begin{cases} -\frac{E_0}{2}\cos\frac{\pi x}{\alpha L} - \frac{n_b q V_{dc}}{L}x & 0 < x < \alpha L \\[3mm] -\frac{E_0}{2}\cos\frac{\pi(L-x)}{(1-\alpha)L} - \frac{n_b q V_{dc}}{L}x & \alpha L < x < L \end{cases}$$

<div align="right">Eq. 7</div>

where E_0 is the energy of activation in the absence of an applied force, L is the periodicity of the potential (assumed to be the base to base length for the case of DNA), n_b is the fractional charge of a single nucleotide, q is the electron charge (1.6×10^{-19} coulombs), and V_{dc} is the applied DC drive voltage. Kramers' escape rate for a step out of and into the pore can now be shown to be:

$$\kappa_{out} = \frac{1}{\tau_0}\sqrt{1 - \left(\frac{2\alpha n_b q V_{dc}}{\pi E_0}\right)^2}\, e^{-\frac{E_0}{kT}\left(\sqrt{1 - \left(\frac{2\alpha n_b q V_{dc}}{\pi E_0}\right)^2} + \frac{2\alpha n_b q V_{dc}}{\pi E_0}\sin^{-1}\frac{2\alpha n_b q V_{dc}}{\pi E_0} - \frac{\alpha n_b q V_{dc}}{\pi E_0}\right)}$$

<div align="right">Eq. 8</div>

$$\kappa_{in} = \frac{1}{\tau_0}\sqrt{1 - \left(\frac{2\alpha n_b q V_{dc}}{\pi E_0}\right)^2}\, e^{-\frac{E_0}{kT}\left(\sqrt{1 - \left(\frac{2\alpha n_b q V_{dc}}{\pi E_0}\right)^2} + \frac{2\alpha n_b q V_{dc}}{\pi E_0}\sin^{-1}\frac{2\alpha n_b q V_{dc}}{\pi E_0} - \frac{(1-\alpha)n_b q V_{dc}}{\pi E_0}\right)}$$

<div align="right">Eq. 9</div>

where the prefactor:

$$\frac{1}{\tau_0} = \frac{\pi E_0}{m\gamma L^2}$$

<div align="right">Eq. 10</div>

can be thought of as the attempt rate for escape over the barrier.

In order to calculate the dependence of the escape rates on the AC probing signal, it must be assumed that the system is in the adiabatic limit. This means that the frequency of the AC monitoring signal is sufficiently low enough that the system stays in thermal equilibrium. In this case, the escape rate can be described as time dependent and the escape rate can be averaged over one period in order to determine the mean escape rate. However, before this is done the above expressions (Equations 8 and 9) for the DC dependent escape rates will be slightly simplified. If the energy due to the applied voltage is small compared to the potential energy barrier (<< 2.5 V based on the value of Ea, 1.8×10^{-19} $Joules$, and the expected charge of a single nucleotide, $\sim 0.7 \times 10^{-19}$ $Coulombs$) [48-50], then only the terms in both the prefactor and the exponential that are linear in the voltage need to be kept:

$$\kappa_{out} = \frac{1}{\tau_0} e^{-\frac{E_0}{kT}} e^{\frac{\alpha n_b q V_{dc}}{kT}}$$

Eq. 11

Now to calculate the escape rates dependence on the AC probing signal, V_{dc} will be replaced with $V_{dc} + V_{ac}\cos\omega t$:

$$\kappa_{out}(t) = \frac{1}{\tau_0} e^{-\frac{E_0}{kT}} e^{\frac{\alpha n_b q V_{dc}}{kT}} e^{\frac{\alpha n_b q V_{ac}}{kT}\cos\omega t}$$

Eq. 12

The mean escape rate for a step out of the pore is then obtained by averaging Equation 12 over one period:

$$\kappa_{out} = \frac{1}{\tau_0} e^{-\frac{E_0}{kT}} e^{\frac{\alpha n_b q V_{dc}}{kT}} \frac{\omega}{2\pi} \int_{-\pi/\omega}^{\pi/\omega} e^{\frac{\alpha n_b q V_{ac}}{kT}\cos\omega t}\, dt$$

Eq. 13

Similarly, the mean escape rate for a step into the αHL pore is:

$$\kappa_{in} = \frac{1}{\tau_0} e^{-\frac{E_0}{kT}} e^{-\frac{(1-\alpha) n_b q V_{dc}}{kT}} \frac{\omega}{2\pi} \int_{-\pi/\omega}^{\pi/\omega} e^{-\frac{(1-\alpha) n_b q V_{ac}}{kT}\cos\omega t}\, dt$$

Eq.14

In the general case we can evaluate these integrands numerically, but to examine the behavior for large V_{ac}, it is instructive to evaluate it when $\alpha n_b q V_{ac} \gg kT$. In that case, the integral is dominated by the region near the maximum of the integrand at $t = 0$; so we replace $\cos\omega t$ by its expansion to order $(\omega t)^2$ and extend the integration limits to $\pm\infty$:

$$\kappa_{out} = \frac{1}{\tau_0} e^{-\frac{E_0}{kT}} e^{\frac{\alpha n_b q V_{dc}}{kT}} e^{\frac{\alpha n_b q V_{ac}}{kT}} \frac{\omega}{2\pi} \int_{-\infty}^{\infty} e^{-\frac{\alpha n_b q V_{ac}}{2kT}(\omega t)^2}\, dt$$

Eq. 15

$$\kappa_{out} \cong \frac{1}{\tau_0} e^{-\frac{E_0}{kT}} e^{\frac{\alpha n_b q V_{dc}}{kT}} e^{\frac{\alpha n_b q V_{ac}}{kT}} \sqrt{\frac{kT}{2\pi \alpha n_b q V_{ac}}}$$

Eq. 16

Similarly, for the in rate:

$$\kappa_{in} = \frac{1}{\tau_0} e^{-\frac{E_0}{kT}} e^{-\frac{(1-\alpha) n_b q V_{dc}}{kT}} e^{-\frac{(1-\alpha) n_b q V_{ac}}{kT}} \frac{\omega}{2\pi} \int_{-\infty}^{\infty} e^{-\frac{(1-\alpha) n_b q V_{ac}}{kT}(\omega t - \pi)^2}\, dt$$

Eq. 17

$$\kappa_{in} = \frac{1}{\tau_0} e^{-\frac{E_0}{kT}} e^{-\frac{(1-\alpha)n_b q V_{dc}}{kT}} e^{\frac{(1-\alpha)n_b q V_{ac}}{kT}} \sqrt{\frac{kT}{2\pi(1-\alpha)n_b q V_{ac}}}$$ Eq.18

In both cases, the exponential is linear in the applied AC voltage.

Consider the ramifications of the simplified expressions in Equations 16 and 18. In the case of a symmetric potential (α = 0.5), κ_{out} and κ_{in} have the same dependency on V_{ac}, so p_{out} is a constant with respect to changes in Vac. At a fixed DC voltage, the mean escape time will then be exponentially dependent on $-V_{ac}$ for $V_{ac} > kT/nq \approx$ 30mV (assuming a fractional charge (n) of 0.4) [48-50]. This result is consistent with the near linear dependence of the log of the mean escape time on V_{ac} at voltages above 30 mV_{ac}, as shown in Figure 92. Alternatively, for large DC voltages and small AC voltages, $\kappa_{out} >> \kappa_{in}$, so $p_{out} \approx$ 1, and the mean escape time is exponentially dependent upon V_{dc} for $V_{dc} > 2kT/nq \approx$ 60mV. As shown in Figure 92, the escape time at 50 mV AC approaches an exponential dependence above $V_{dc} \approx$ 50 mV. These qualitative predictions provided by simplifications of the model are a strong indication that the overall model provides a good description of the physical processes being measured.

Equation 5, 16, and 18 in combination with the results from solving Equation 4 can be used to model the mean escape time of the HP-A$_{50}$ molecule. Using a least squares regression analysis, the experimental data presented in Figure 92 and Figure 94 were fit in order to determine the most likely values for the four adjustable parameters: τ_0, the overall scaling of all the results (this value is the inverse of the "attempt rate" for the thermally activated escape over the barrier); E_0, the height of the activation energy barrier presented by the periodic potential: n_b, the effective number of charges per nucleotide, and α, the asymmetry parameter of the periodic potential. Based on the best fits of the experimentally obtained data, presented in Figure 92 and Figure 94, τ_0 = 7.37x10^{-22} sec; E_0 = 1.8x10^{-19} Joules; n_b = 0.463 charges/base, in good agreement with the reported literature value of 0.4 [48-50] and α = 0.581. This measurement represents the first such measurement in which α is directly measured. And while α = 0.581 represents only a small level of asymmetry (0.5 = symmetric), this asymmetry can have a large effect on κ_{out} and κ_{in}, as depicted in , and is the reason why an AC signal has such a large effect on the escape rate of the HP-A$_{50}$ molecule.

8.4.5. Conclusions

EBS has developed a new AC methodology for monitoring the conductance of an αHL pore as a DNA molecule containing a polydeoxyadenosine tail is driven into and released from the pore. Using this method we have obtained accurate measures of the diffusion of ssDNA in the αHL nanopore from 20 °C to -10 °C. By reducing the temperature we have succeeded in reducing the diffusion coefficient by a factor of 200. The reduced diffusion coefficient leads to a characteristic diffusion length of less than 1 base per millisecond, and will enable the use of detection bandwidths as low as 10 kHz to ultimately perform nanopore based DNA sequencing.

Additionally we have demonstrated that the potential energy surface of ssDNA traversing the αHL nanopore is well described by a one-dimensional asymmetric periodic potential model. By combining the AC signal which serves to oscillate the asymmetric periodic potential model both up and down, we have been able to unambiguously determine the activation energy and asymmetry factor associated with HP-A$_{50}$ escaping out of the cis side of the αHL pore. This methodology should allow us to map out structure associated with the periodic potential model for adenines, cytosines, thymines, and guanines exiting both the cis and trans sides of the αHL pore. A better understanding of the biopolymer pore interaction will enable us to better predict

the conditions that will allow for controlled DNA translocation and the development of nanopore DNA sequencing.

9. References

[1]   B. Sakmann and E. Neher, *Single-channel recording*, 2nd ed. New York: Plenum Press, 1995.

[2]   O. Braha, L.-Q. Gu, L. Zhou, X. Lu, S. Cheley, and H. Bayley, "Simultaneous stochastic sensing of divalent metal ions," *Nat Biotech*, vol. 18, pp. 1005-1007, 2000.

[3]   O. Braha, B. Walker, S. Cheley, J. J. Kasianowicz, L. Song, J. E. Gouaux, and H. Bayley, "Designed protein pores as components for biosensors," *Chemistry and Biology*, vol. 4, pp. 497-505, 1997.

[4]   S. Cheley, L.-Q. Gu, and H. Bayley, "Stochastic Sensing of Nanomolar Inositol 1,4,5-Trisphosphate with an Engineered Pore," *Chemistry & Biology*, vol. 9, pp. 829-838, 2002.

[5]   L.-Q. Gu, O. Braha, S. Conlan, S. Cheley, and H. Bayley, "Stochastic sensing of organic analytes by a pore-forming protein containing a molecular adapter," *Nature*, vol. 398, pp. 686-690, 1999.

[6]   X. Guan, L.-Q. Gu, S. Cheley, O. Braha, and H. Bayley, "Stochastic Sensing of TNT with a Genetically Engineered Pore," *ChemBioChem*, vol. 6, pp. 1875-1881, 2005.

[7]   J. W. F. Robertson, C. G. Rodrigues, V. M. Stanford, K. A. Rubinson, O. V. Krasilnikov, and J. J. Kasianowicz, "Single-molecule mass spectrometry in solution using a solitary nanopore," *PNAS*, vol. 104, pp. 8207-8211, 2007.

[8]   L. Movileanu and H. Bayley, "Partitioning of a polymer into a nanoscopic protein pore obeys a simple scaling law," *PNAS*, vol. 98, pp. 10137-10141, 2001.

[9]   L. Movileanu, S. Howorka, O. Braha, and H. Bayley, "Detecting protein analytes that modulate transmembrane movement of a polymer chain within a single protein pore," *Nat Biotech*, vol. 18, pp. 1091-1095, 2000.

[10]   M. Akeson, D. Branton, J. J. Kasianowicz, E. Brandin, and D. W. Deamer, "Microsecond Time-Scale Discrimination Among Polycytidylic Acid, Polyadenylic Acid, and Polyuridylic Acid as Homopolymers or as Segments Within Single RNA Molecules," *Biophys. J.*, vol. 77, pp. 3227-3233, 1999.

[11]   W. Vercoutere, S. Winters-Hilt, H. Olsen, D. Deamer, D. Haussler, and M. Akeson, "Rapid discrimination among individual DNA hairpin molecules at single-nucleotide resolution using an ion channel," *Nature Biotechnology*, vol. 19, pp. 248-252, 2001.

[12]   J. J. Nakane, M. Akeson, and A. Marziali, "Nanopore sensors for nucleic acid analysis," *Journal of Physics: Condensed Matter*, vol. 15, pp. R1365-93, 2003.

[13]   J. Mathe, A. Aksimentiev, D. R. Nelson, K. Schulten, and A. Meller, "Orientation discrimination of single-stranded DNA inside the {alpha}-hemolysin membrane channel," *PNAS*, vol. 102, pp. 12377-12382, 2005.

[14]   S. Terrettaz, W.-P. Ulrich, R. Guerrini, A. Verdini, and H. Vogel, "Immunosensing by a Synthetic Ligand-Gated Ion Channel," *Angewandte Chemie International Edition*, vol. 40, pp. 1740-1743, 2001.

[15]   R. Naumann, S. M. Schiller, F. Giess, B. Grohe, K. B. Hartman, I. Karcher, I. Koper, J. Lubben, K. Vasilev, and W. Knoll, "Tethered Lipid Bilayers on Ultraflat Gold Surfaces," *Langmuir*, vol. 19, pp. 5435-5443, 2003.

[16]   V. Atanasov, P. P. Atanasova, I. K. Vockenroth, N. Knorr, and I. Koper, "A Molecular Toolkit for Highly Insulating Tethered Bilayer Lipid Membranes on Various Substrates," *Bioconjugate Chem.*, vol. 17, pp. 631-637, 2006.

[17]   G. Bainbridge, I. Gokce, and J. H. Lakey, "Voltage gating is a fundamental feature of porin and toxin [beta]-barrel membrane channels," *FEBS Letters,* vol. 431, pp. 305-308, 1998.

[18]   M. Montal and P. Mueller, "Formation of Bimolecular Membranes from Lipid Monolayers and a Study of their Electrical Properties," *PNAS,* vol. 69, pp. 3561-3566, 1972.

[19]   P. Mueller, D. O. Rudin, H. T. Tien, and W. C. Wescott, "Methods for the Formation of Single Bimolecular Lipid Membranes in Aqueous solution," *J. Phys. Chem.,* vol. 67, pp. 534-535, 1963.

[20]   L. Petrossian, S. J. Wilk, P. Joshi, S. Hihath, J. D. Posner, S. M. Goodnick, and T. J. Thornton, "High aspect ratio cylindrical nanopores in silicon-on-insulator substrates," *Solid-State Electronics,* vol. 51, pp. 1391-1397, 2007.

[21]   L. Petrossian, S. J. Wilk, P. Joshi, S. Hihath, S. M. Goodnick, and T. J. Thornton, "Fabrication of Cylindrical Nanopores and Nanopore Arrays in Silicon-On-Insulator Substrates," *Journal of Microelectromechanical Systems,* vol. 16, pp. 1419-1428, 2007.

[22]   B. Zhang, Y. Zhang, and H. S. White, "The Nanopore Electrode," *Anal. Chem.,* vol. 76, pp. 6229-6238, 2004.

[23]   B. Zhang, J. Galusha, P. G. Shiozawa, G. Wang, A. J. Bergren, R. M. Jones, R. J. White, E. N. Ervin, C. C. Cauley, and H. S. White, "Bench-Top Method for Fabricating Glass-Sealed Nanodisk Electrodes, Glass Nanopore Electrodes, and Glass Nanopore Membranes of Controlled Size," *Anal. Chem.,* vol. 79, pp. 4778-4787, 2007.

[24]   A. J. Melmed and J. J. Carroll, "An approach to realism in field ion microscopy via zone electropolishing," *Journal of Vacuum Science & Technology A: Vacuum, Surfaces, and Films,* vol. 2, pp. 1388-1389, 1984.

[25]   A. J. Melmed, "The art and science and other aspects of making sharp tips," in *Fifth International Conference on Scanning Tunneling Microscopy/Spectroscopy and First International Conference on Nanometer Scale Science and Technology. Maltimore, MD,* 1991.

[26]   R. J. White, B. Zhang, S. Daniel, J. M. Tang, E. N. Ervin, P. S. Cremer, and H. S. White, "Ionic Conductivity of the Aqueous Layer Separating a Lipid Bilayer Membrane and a Glass Support," *Langmuir,* vol. 22, pp. 10777-10783, 2006.

[27]   J. W. Shim and L. Q. Gu, "Stochastic Sensing on a Modular Chip Containing a Single-Ion Channel," *Anal. Chem.,* vol. 79, pp. 2207-2213, 2007.

[28]   M. Mayer, J. K. Kriebel, M. T. Tosteson, and G. M. Whitesides, "Microfabricated Teflon Membranes for Low-Noise Recordings of Ion Channels in Planar Lipid Bilayers," *Biophys. J.,* vol. 85, pp. 2684-2695, 2003.

[29]   B. Walker and H. Bayley, "Key Residues for Membrane Binding, Oligomerization, and Pore Forming Activity of Staphylococcal alpha-Hemolysin Identified by Cysteine Scanning Mutagenesis and Targeted Chemical Modification," *J. Biol. Chem.,* vol. 270, pp. 23065-23071, 1995.

[30]   L. Song, M. R. Hobaugh, C. Shustak, S. Cheley, H. Bayley, and J. E. Gouaux, "Structure of Staphylococcal alpha -Hemolysin, a Heptameric Transmembrane Pore," *Science,* vol. 274, pp. 1859-1865, 1996.

[31]   H.-C. Wu and H. Bayley, "Single-Molecule Detection of Nitrogen Mustards by Covalent Reaction within a Protein Nanopore," *Journal of the American Chemical Society,* vol. 130, pp. 6813-6819, 2008.

[32]   N. B. Munro, S. S. Talmage, G. D. Griffin, L. C. Waters, A. P. Watson, J. F. King, and V. Hauschild, "The sources, fate, and toxicity of chemical warfare agent degradation products," *Environ Health Perspect,* vol. 107, pp. 933-74, 1999.

[33]   Q. Zhao, D. A. Jayawardhana, and X. Guan, "Stochastic Study of the Effect of Ionic Strength on Noncovalent Interactions in Protein Pores," *Biophys. J.,* vol. 94, pp. 1267-1275, 2008.

[34]   W. E. Steiner, C. S. Harden, F. Hong, S. J. Klopsch, H. H. Hill, and V. M. McHugh, "Detection of Aqueous Phase Chemical Warfare Agent Degradation Products by Negative Mode Ion Mobility Time-of-Flight Mass Spectrometry [IM(tof)MS]," *Journal of the American Society for Mass Spectrometry,* vol. 17, pp. 241-245, 2006.

[35]   M. V. Rekharsky and Y. Inoue, "Complexation Thermodynamics of Cyclodextrins," *Chemical Reviews,* vol. 98, pp. 1875-1918, 1998.

[36]   H. Piao, R. B. Marx, S. Schneider, D. A. Irvine, and J. Staton, "Analysis of VX nerve agent hydrolysis products in wastewater effluents by ion chromatography with amperometric and conductivity detection," *Journal of Chromatography A,* vol. 1089, pp. 65-71, 2005.

[37]   X. F. Kang, S. Cheley, X. Guan, and H. Bayley, "Stochastic detection of enantiomers," *J. Am. Chem. Soc,* vol. 128, pp. 10684-10685, 2006.

[38]   F. Sachs, J. Neil, and N. Barkakati, "The Automated-Analysis of Data from Single Ionic Channels," *Pflugers Archiv-European Journal of Physiology,* vol. 395, pp. 331-340, 1982.

[39]   F. Qin, "Restoration of Single-Channel Currents Using the Segmental k-Means Method Based on Hidden Markov Modeling," *Biophysical Journal,* vol. 86, pp. 1488-1501, 2004.

[40]   O. B. McManus, A. L. Blatz, and K. L. Magleby, "Sampling, log binning, fitting, and plotting durations of open and shut intervals from single channels and the effects of noise," *Pflügers Archiv European Journal of Physiology,* vol. 410, pp. 530-553, 1987.

[41]   D. Colquhoun and F. J. Sigworth, "Fitting and statistical analysis of single-channel records In Sakmann, B. and Neher, E," Single Channel Recording, NY and London Plenum Press, 1983.

[42]   C. R. Rao, *Linear Statistical Inference and Its Applications.* New York: Wiley, 1973.

[43]   B. Walker, M. Krishnasastry, L. Zorn, J. Kasianowicz, and H. Bayley, "Functional expression of the alpha-hemolysin of Staphylococcus aureus in intact Escherichia coli and in cell lysates. Deletion of five C- terminal amino acids selectively impairs hemolytic activity," *J. Biol. Chem.,* vol. 267, pp. 10902-10909, 1992.

[44]   John J. Kasianowicz, E. Brandin, D. Branton, and David W. Deamer, "Characterization of individual polynucleotide molecules using a membrane channel," *Proceedings of the National Academy of Sciences,* vol. 93, pp. 13770-13773, 1996.

[45]   Y. Astier, O. Braha, and H. Bayley, "Toward Single Molecule DNA Sequencing: Direct Identification of Ribonucleoside and Deoxyribonucleoside 5'-Monophosphates by Using an Engineered Protein Nanopore Equipped with a Molecular Adapter," *J. Am. Chem. Soc.,* vol. 128, pp. 1705-1710, 2006.

[46]   A. Meller, L. Nivon, E. Brandin, J. Golovchenko, and D. Branton, "Rapid nanopore discrimination between single polynucleotide molecules," *PNAS,* vol. 97, pp. 1079-1084, 2000.

[47]   N. Ashkenasy, J. Sánchez-Quesada, H. Bayley, and M. R. Ghadiri, "Recognizing a Single Base in an Individual DNA Strand: A Step Toward DNA Sequencing in Nanopores," *Angewandte Chemie International Edition,* vol. 44, pp. 1401-1404, 2005.

[48]   E. N. Ervin, R. Kawano, R. J. White, and H. S. White, "Simultaneous Alternating and Direct Current Readout of Protein Ion Channel Blocking Events Using Glass Nanopore Membranes," *Anal. Chem.,* vol. 80, pp. 2069-2076, 2008.

[49]   J. Nakane, M. Wiggin, and A. Marziali, "A Nanosensor for Transmembrane Capture and Identification of Single Nucleic Acid Molecules," *Biophys. J.,* vol. 87, pp. 615-621, 2004.

[50]   V. S. DeGuzman, C. C. Lee, D. W. Deamer, and W. A. Vercoutere, "Sequence-dependent gating of an ion channel by DNA hairpin molecules," *Nucl. Acids Res.,* vol. 34, pp. 6425-6437, 2006.

[51]   J. Mathe, A. Aksimentiev, D. R. Nelson, K. Schulten, and A. Meller, "Orientation discrimination of single-stranded DNA inside the α-hemolysin membrane channel,"

Proceedings of the National Academy of Sciences of the United States of America, vol. 102, pp. 12377-12382, 2005.

[52]   D. K. Lubensky and D. R. Nelson, "Driven Polymer Translocation Through a Narrow Pore," Biophys. J., vol. 77, pp. 1824-1838, 1999.

[53]   R. J. White, E. N. Ervin, T. Yang, X. Chen, S. Daniel, P. S. Cremer, and H. S. White, "Single Ion-Channel Recordings Using Glass Nanopore Membranes," J. Am. Chem. Soc., vol. 129, pp. 11766-11775, 2007.

[54]   W. Meni, C. Buddhapriya, M. Jerome, R. N. David, and M. Amit, "Orientation-dependent interactions of DNA with an alpha-hemolysin channel," Physical Review E (Statistical, Nonlinear, and Soft Matter Physics), vol. 77, p. 031904, 2008.

[55]   H. A. Kramers, "Brownian motion in a field of force and the diffusion model of chemical reactions," Physica, 7, 1940.

[56]   C. W. Gardiner, Handbook of stochastic methods: Springer.

10. Key Personnel on the MOLDICE Program

Electronic Bio Sciences, LLC
5754 Pacific Center Blvd. Suite 204
San Diego, CA 92121
Dr. Andrew D. Hibbs
Dr. Geoffrey A. Barrall

Arizona State University
College of Engineering and Applied Sciences
Arizona State University, Tempe, AZ 85287-5706
Professor Stephen Goodnick
Professor Trevor Thornton

Max Planck University
Max Planck Institute for Polymer Research
Ackermannweg 10
55128 Mainz, Germany
Dr. Ingo Koper
Dr. Wolfgang Knoll

Oxford University
Chemical Biology Sub-Department
University of Oxford
Chemistry Research Laboratory
12 Mansfield Road
Oxford OX1 3TA
United Kingdom
Professor Hagan Bayley

Rush University
Rush University Medical Center
1750 W. Harrison St.
Chicago, IL 60612
Dr. Robert Eisenberg
Dr. John Tang

Texas A&M University
Department of Chemistry
P. O. Box 30012
College Station, TX 77842-3012
Professor Paul Cremer

University of California, Los Angeles
420 Westwood Plaza, Room 5121 ENGINEERING V
PO Box 951600
Los Angeles, CA 90095-1600
Professor Jacob Schmidt

University of Massachusetts
Department of Polymer Science and Engineering
Room A212, Conte Research Center
120 Governors Drive
Amherst, MA 01003
Professor Murugappan Muthukumar

University of Miami
Department of Physiology and Biophysics
Leonard M. Miller School of Medicine
P.O. Box 016430
Miami, FL 33101
Professor Karl Magleby

University of Texas, Arlington
Department of Chemistry and Biochemistry
Arlington, Texas 76019-0065, USA
Professor Richard (Xiyun) Guan

University of Texas, Austin
UT-PRC
10100 Burnet Road, Bldg 160
Mail Code R9900
Austin, TX 78758
Dr. Ananth Dodabalapur

University of Utah
315 So. 1400 E. Rm. 2020
Salt Lake City, Utah 84112-0850
Professor Henry White

11. Journal Articles Resulting from the MOLDICE Program

[1]   V. Atanasov, N. Knorr, R. S. Duran, S. Ingebrandt, A. Offenhausser, W. Knoll, and I. Koper, "Membrane on a Chip: A Functional Tethered Lipid Bilayer Membrane on Silicon Oxide Surfaces," *Biophys. J.,* vol. 89, pp. 1780-1788, 2005.

[2]   J. Schmidt, "Stochastic sensors," *Journal of Materials Chemistry,* vol. 15, pp. 831-840, 2005.

[3]   I. K. Vockenroth, P. P. Atanasova, W. Knoll, I. Koper, A. Toby, and A. Jenkins, "Functional tethered bilayer membranes as a biosensor platform," IEEE Sensors 2005 - The 4-th IEEE Conference on Sensors . Irvine, CA: IEEE Sensors, pp. 608-610, 2005.

[4]   F. Albertorio, S. Daniel, and P.S. Cremer, "Supported Lipopolymer Membranes as Nanoscale Filters: Simultaneous Protein Recognition and Size Selection Assays," *J. Am. Chem. Soc.,* vol. 128, pp. 7168-7169, 2006.

[5]   V. Atanasov, P. P. Atanasova, I. K. Vockenroth, N. Knorr, and I. Koper, "A Molecular Toolkit for Highly Insulating Tethered Bilayer Lipid Membranes on Various Substrates," *Bioconjugate Chem.,* vol. 17, pp. 631-637, 2006.

[6]   S. Daniel, F. Albertorio, and P.S. Cremer, "Making Lipid Membranes Rough, Tough, and Ready to Hit the Road," *MRS Bulletin,* vol. 31, pp. 536-540, 2006.

[7]   E.N. Ervin, H.S. White, L.A. Baker, and C.R. Martin, "Alternating Current Impedance Imaging of High-Resistance Membrane Pores using a Scanning Electrochemical Microscope. Application of Membrane Electrical Shunts to Increase Measurement Sensitivity and Image Contrast," *Analytical Chemistry,* vol. 78, pp. 6535-6541, 2006.

[8]   I. Koper, S. M. Schiller, F. Giess, R. Naumann, W. Knoll, "Functional tethered bimolecular lipid membranes (tBLMs)," *Advances in Planar Lipid Bilayers,* vol. 3, pp. 37-53, 2006.

[9]   R. J. White, B. Zhang, S. Daniel, J. M. Tang, E. N. Ervin, P. S. Cremer, and H. S. White, "Ionic Conductivity of the Aqueous Layer Separating a Lipid Bilayer Membrane and a Glass Support," *Langmuir,* vol. 22, pp. 10777-10783, 2006.

[10]   B. Zhang, Y. Zhang, and H.S. White, "Steady-State Voltammetric Response of the Nanopore Electrode", *Anal. Chem.,* vol. 78, pp. 477-483, 2006.

[11]   F. Albertorio, V.A. Chapa, X. Chen, A.J. Diaz, and P.S. Cremer, "The α,α-(1→1) Linkage of Trehalose is Key to Anhydrobiotic Preservation," *J. Am. Chem. Soc.,* vol. 129, pp. 10567-10574, 2007.

[12]   S. Daniel, A.J. Diaz, K.M. Martinez, B.J. Bench, F. Albertorio, and P.S. Cremer, "Separation of Membrane-Bound Compounds by Solid-Supported Bilayer Electrophoresis," *J. Am. Chem. Soc.,* vol. 129, pp. 8072-8073, 2007.

[13]   E. N. Ervin, R. J. White, T. G. Owens, J. M. Tang, and H. S. White, "AC Conductance of Transmembrane Protein Channels. The Number of Ionized Residue Mobile Counterions at Infinite Dilution," *J. Phys. Chem. B,* vol. 111, pp. 9165-9171, 2007.

[14]   H.M. Keizer, B.R. Drovel, M. Andersson, D. Fine, R.B. Price, J.R. Long, A. Dodabalapur, I. Koper, W. Knoll, P.A.V. Anderson, and R.S. Duran, "Functional Ion Channels in Tethered Bilayer Membranes – Implications for Biosensors," *ChemBioChem,* vol. 8, pp. 1246-1250, 2007.

[15]　I. Koper, "Insulating tethered bilayer lipid membranes to study membrane proteins," *Mol. Biosyst.*, vol. 10, pp. 651-657, 2007.

[16]　L. Petrossian, S. J. Wilk, P. Joshi, S. Hihath, J. D. Posner, S. M. Goodnick, and T. J. Thornton, "High aspect ratio cylindrical nanopores in silicon-on-insulator substrates," *Solid-State Electronics,* vol. 51, pp. 1391-1397, 2007.

[17]　L. Petrossian, S. J. Wilk, P. Joshi, S. Hihath, S. M. Goodnick, and T. J. Thornton, "Fabrication of Cylindrical Nanopores and Nanopore Arrays in Silicon-On-Insulator Substrates," *Journal of Microelectromechanical Systems,* vol. 16, pp. 1419-1428, 2007.

[18]　J.H. Shim, J. Kim, G.S. Cha, H. Nam, R.J. White, H.S. White, and R.B. Brown, "Glass Nanopore-Based Ion-Selective Electrodes," *Anal. Chem.*, vol. 79, pp. 3568-3574, 2007.

[19]　I.K. Vockenroth, P.P. Atanasova, J.R. Long, A.T.A. Jenkins, W. Knoll, I. Koper, "Functional incorporation of the pore forming segment of AChR M2 into tethered bilayer lipid membranes" *Biochim Biophys Acta.*, vol. 1768, pp. 1114-1120, 2007.

[20]　R. J. White, E. N. Ervin, T. Yang, X. Chen, S. Daniel, P. S. Cremer, and H. S. White, "Single Ion-Channel Recordings Using Glass Nanopore Membranes," *J. Am. Chem. Soc.,* vol. 129, pp. 11766-11775, 2007.

[21]　R.J. White, and H.S. White, "Influence of Electrophoresis Waveforms in Determining Stochastic Nanoparticle Capture Rates and Detection Sensitivity" *Analytical Chemistry*, vol. 79, pp. 6334-6340, 2007.

[22]　B. Zhang, J. Galusha, P. G. Shiozawa, G. Wang, A. J. Bergren, R. M. Jones, R. J. White, E. N. Ervin, C. C. Cauley, and H. S. White, "Bench-Top Method for Fabricating Glass-Sealed Nanodisk Electrodes, Glass Nanopore Electrodes, and Glass Nanopore Membranes of Controlled Size," *Anal. Chem.,* vol. 79, pp. 4778-4787, 2007.

[23]　Q. Zhao, D.A. Jayawardhana, and X. Guan, "Stochastic Study of the Effect of Ionic Strength on Non-Covalent Interactions in Protein Pores," *Biophys J.*, vol. 94, pp. 1267-1275, 2007.

[24]　E. N. Ervin, R. Kawano, R. J. White, and H. S. White, "Simultaneous Alternating and Direct Current Readout of Protein Ion Channel Blocking Events Using Glass Nanopore Membranes," *Anal. Chem.,* vol. 80, pp. 2069-2076, 2008.

[25]　K. V. Inga, O. Christian, W. F. R. Joseph, J. M. Duncan, L. Mathias, and K. Ingo, "Stable insulating tethered bilayer lipid membranes," *Biointerphases,* vol. 3, pp. FA68-FA73, 2008.

[26]　W. Knoll, I. Koper, R. Naumann, and E.-K. Sinner, "Tethered bimolecular lipid membranes--A novel model membrane platform," *Electrochimica Acta,* vol. 53, pp. 6680-6689, 2008.

[27]　I.K. Vockenroth, P. Atanasova, A. Jenkins, I. Koper, "Incorporation of alpha-Hemolysin in Different Tethered Bilayer Lipid Membrane Architectures." *Langmuir,* vol. 24, pp. 2954–2954, 2008.

[28]　I. K. Vockenroth, D. Fine, A. Dodobalapur, A. T. A. Jenkins, and I. Koper, "Tethered bilayer lipid membranes with giga-ohm resistances," *Electrochemistry Communications,* vol. 10, pp. 323-328, 2008.

[29]   H.-C. Wu and H. Bayley, "Single-Molecule Detection of Nitrogen Mustards by Covalent Reaction within a Protein Nanopore," *Journal of the American Chemical Society,* vol. 130, pp. 6813-6819, 2008.

[30]   H.S. White and A. Bund, "Ion current rectification at nanopores in glass membranes," *Langmuir,* vol. 24, pp. 2212-2218, 2008.

[31]   Q. Zhao, D. A. Jayawardhana, and X. Guan, "Stochastic Study of the Effect of Ionic Strength on Noncovalent Interactions in Protein Pores," *Biophys. J.,* vol. 94, pp. 1267-1275, 2008.

[32]   D.K. Lathrop, E.N. Ervin, G.A. Barrall, M.G. Keehan, R. Kawano, M.A. Krupka, H.S. White, and A.D. Hibbs, "Monitoring the Escape of DNA from a Nanopore Using an Alternating Current Signal," To be submitted, 2009.